# MEASUREMENT OF $^{34}$Ar($\alpha$,p)$^{37}$K USING THE JENSA GAS JET TARGET

By

Justin Edward Browne

A DISSERTATION

Submitted to
Michigan State University
in partial fulfillment of the requirements
for the degree of

Physics — Doctor of Philosophy

2020

## ABSTRACT

MEASUREMENT OF $^{34}$Ar($\alpha$,p)$^{37}$K USING THE JENSA GAS JET TARGET

By

Justin Edward Browne

X-ray bursts are very luminous thermonuclear explosions that occur in binary star systems. In these systems, a neutron star accreting matter from a companion star undergoes a runaway thermonuclear explosion, caused by a breakout from the CNO-cycle into the $\alpha$p-process. The $\alpha$p-process consists of a series of ($\alpha$,p) and (p,$\gamma$) reactions. In this process, there are "waiting point" nuclei at which the nuclear burning pauses until the stellar conditions change so that the ($\alpha$,p) reaction rate increases and burning continues. $^{34}$Ar is one of these waiting point nuclei, and sensitivity studies have found that varying the $^{34}$Ar($\alpha$,p)$^{37}$K reaction rate significantly impacts the light curve of x-ray bursts.

Because the $^{34}$Ar($\alpha$,p)$^{37}$K cross section had never been directly measured before, the reaction rates used in simulations are based on Hauser-Feshbach predictions. These predictions are hypothesized to be inaccurate because the Hauser-Feshbach statistical model requires a high level density in the compound nucleus and assumes there are no dominant resonances.

This thesis describes an experiment at the National Superconducting Cyclotron Laboratory (NSCL) designed to test Hauser-Feshbach predictions by directly measuring the $^{34}$Ar($\alpha$,p)$^{37}$K cross section. A radioactive ion beam of $^{34}$Ar$^{15+}$ with energies of 57.04 MeV and 54.19 MeV was delivered to a (5–8) $\times$ $10^{18}$ atoms/cm$^2$ thick He target, created by the Jet Experiments in Nuclear Structure and Astrophysics (JENSA) gas jet target. The recoils and beam were detected by the ANASEN position-sensitive ionization chamber, and the ejectiles were detected by an array of silicon detectors combining SuperORRUBA and SIDAR. The

beam included contamination from the decay products of $^{34}$Ar, namely $^{34}$Cl and $^{34}$S. While the contribution from $^{34}$S($\alpha$,p)$^{37}$Cl could be subtracted because the cross section had be previously measured, the contributions from $^{34}$Cl($\alpha$,p)$^{37}$Ar and $^{34}$Ar($\alpha$,p)$^{37}$K could not be separated, so a combined cross section for the two was derived from the data.

The the combined $^{34}$Cl($\alpha$,p)$^{37}$Ar and $^{34}$Ar($\alpha$,p)$^{37}$K cross sections were determined to be $(70 \pm 21)$ mb at $(5.91 \pm 0.08)$ MeV and $(52 \pm 13)$ mb at $(5.51 \pm 0.08)$ MeV in the center of mass frame. Comparison with Hauser-Feshbach theory indicates that the experimental cross sections are lower by 37 % and 20 %, for the two energies, respectively. This suggests that the hypothesis that the Hauser-Feshbach model overestimates the $^{34}$Ar($\alpha$,p)$^{37}$K cross section by 2 orders of magnitude is unlikely to be true at these energies.

# TABLE OF CONTENTS

# LIST OF TABLES

# LIST OF FIGURES

# Chapter 1

# Introduction

## 1.1 X-Ray Bursts

X-ray binaries are a type of binary stellar system in which a neutron star or black hole accretes matter from a companion star. The energy released by the change in gravitational energy of the accreted matter makes the system very luminous in x-rays. A subset of these x-ray binaries exhibit bursts in which the luminosity increases by about an order of magnitude, releasing about $10^{40}$ erg. These bursts typically last 10 s to 100 s and occur with recurrence times of hours to days [1, 2].

As the accreted matter accumulates on the surface of the neutron star, it is compressed and heated to $(10^6$–$10^7)$ K, which is hot enough for thermonuclear reactions to occur. For thin shells of gas, such as the accreted layer on the surface of the neutron star, the heat produced from the nuclear burning is not compensated by the cooling through expansion, leading to a thermal instability [3]. The partial degeneracy of the electron gas at typical densities of $(10^5$–$10^6)$ g/cm$^3$ also limits the ability of the layer to expand with rising temperature. Since the nuclear reactions are very sensitive to the temperature, the increase in the temperature from these nuclear reactions increases the rate at which the reactions occur. This leads to a thermonuclear runaway.

The details of the burst depend heavily on the parameters of the system, such as the

accretion rate, the composition of the accreted material (especially the amount of hydrogen, helium, and CNO elements), rotation speed, and heating from deeper parts of the neutron star. A typical burst scenario involves hydrogen burning via the CNO cycle, helium burning via the triple-α reaction, breakout of the CNO cycle, helium burning via the αp-process, then hydrogen burning via the rp-process.

The αp-process is composed of mainly (α,p) and (p,γ) reactions. Although (p,γ) reactions tend to be much faster than their competing (α,p) reactions, an equilibrium with the inverse (γ,p) reaction is established, so that overall the (α,p) reaction is more dominant. This synthesizes nuclei up to around Sc ($Z = 21$) [2]. Equation (1.1) shows a typical reaction path for the αp-process. From here, the (p,γ) start to dominate, and the rp-process starts, which is composed of (p,γ) and $\beta^+$ reactions. This continues until the hydrogen is exhausted, and is limited by the SnSbTe cycle, the endpoint of the rp-process [4].

$$\begin{aligned} &{}^{14}\mathrm{O}(\alpha,\mathrm{p})^{17}\mathrm{F}(\mathrm{p},\gamma)^{18}\mathrm{Ne}(\alpha,\mathrm{p})^{21}\mathrm{Na}(\mathrm{p},\gamma)^{22}\mathrm{Mg}(\alpha,\mathrm{p})^{25}\mathrm{Al}(\mathrm{p},\gamma)^{26}\mathrm{Si}(\alpha,\mathrm{p}) \\ &{}^{29}\mathrm{P}(\mathrm{p},\gamma)^{30}\mathrm{S}(\alpha,\mathrm{p})^{33}\mathrm{Cl}(\mathrm{p},\gamma)^{34}\mathrm{Ar}(\alpha,\mathrm{p})^{37}\mathrm{K}(\mathrm{p},\gamma)^{38}\mathrm{Ca}(\alpha,\mathrm{p})^{41}\mathrm{Sc} \end{aligned} \tag{1.1}$$

The exact reaction path depends heavily on the temperature and density. Different competing reactions dominate at different temperatures. For example, some β-decay rates for nuclei with short half-lives are comparable to the competing (α,p) or (p,γ) rates, leading to alternative or parallel reaction paths [2].

The shape of the light curve—how the intensity of light output varies over time—is one of the main observables used to compare calculations with actual bursts. Some x-ray bursts exhibit multi-peak structures in the light curve. This was explained as being caused by the luminosity exceeding the Eddington limit, resulting in the expansion of the neutron

star's radius. The star then cools, and the frequency of the radiation is pushed outside of the detection range of the detector [5]. However, in some rare cases, the *bolometric* luminosity—the total energy output in all energy ranges—also exhibits double-peaked [6–8] or even triple-peaked [9, 10] structures. One explanation of this is that there are "waiting points" where (p,$\gamma$)-($\gamma$,p) equlilibrium causes the reaction flow to stall until the temperature increases enough for the ($\alpha$,p) reaction rate to allow for the reaction flow to continue. $^{30}$S and $^{34}$Ar were found to be waiting points important for potentially creating a double-peak structure [11]. Therefore, the rates of ($\alpha$,p) reactions on these isotopes are of particular interest.

Sensitivity studies are studies in which many reaction rates are varied to see the effect it has on burst calculations. Varying the $^{34}$Ar($\alpha$,p)$^{37}$K reaction rate has been found to have a significant impact on the light curve of x-ray bursts [12].

Finally, different conditions, such as temperature, accretion rate, the metallicity of accreted matter, etc. allow for either bursts or stable burning [13, 14]. In steady-state burning, ($\alpha$,p) reactions also play an important role in determining the fuel-to-seed ratio for the rp-process [14].

These considerations motivated the experimental study of the $^{34}$Ar($\alpha$,p)$^{37}$K reaction in this thesis.

## 1.2 Cross Section and Reaction Rate

Consider a scenario in which particles with velocity $v$ are traveling through a volume $V$ occupied by another group of particles. The moving group is called the beam and the stationary group is called the target. The number of beam and target particles are $N_b$ and

$N_t$, respectively, their number densities are $n_b$ and $n_t$, and the current density of the beam is $j_b = n_b v$.

The reaction rate per target nucleus is

$$\lambda = \sigma j_b. \tag{1.2}$$

$\sigma$ is the reaction cross section, a property of the reaction describing the probability of it occurring, given in units of area. The number of reactions for a period of time, $R$, can be expressed as

$$R = \lambda N_t = \sigma n_b v n_t V. \tag{1.3}$$

The reaction rate per volume is then given by

$$r = n_b n_t \sigma v. \tag{1.4}$$

In a stellar environment, the reactants are not monoenergetic. To account for this, the reaction rate must be averaged over the energies of the particles:

$$\langle \sigma v \rangle = \int \sigma(E) v(E) P(E) \, \mathrm{d}E \,, \tag{1.5}$$

where $P(E)\,\mathrm{d}E$ is the probability of a particle having an energy between $E$ and $E + \mathrm{d}E$. In a star, the energies are distributed according to the Maxwell-Boltzmann distribution, which is given by

$$P(E)\,\mathrm{d}E = \frac{2}{\sqrt{\pi}} \frac{1}{(k_\mathrm{B}T)^{3/2}} \sqrt{E} \exp(-E/k_\mathrm{B}T)\,\mathrm{d}E \,. \tag{1.6}$$

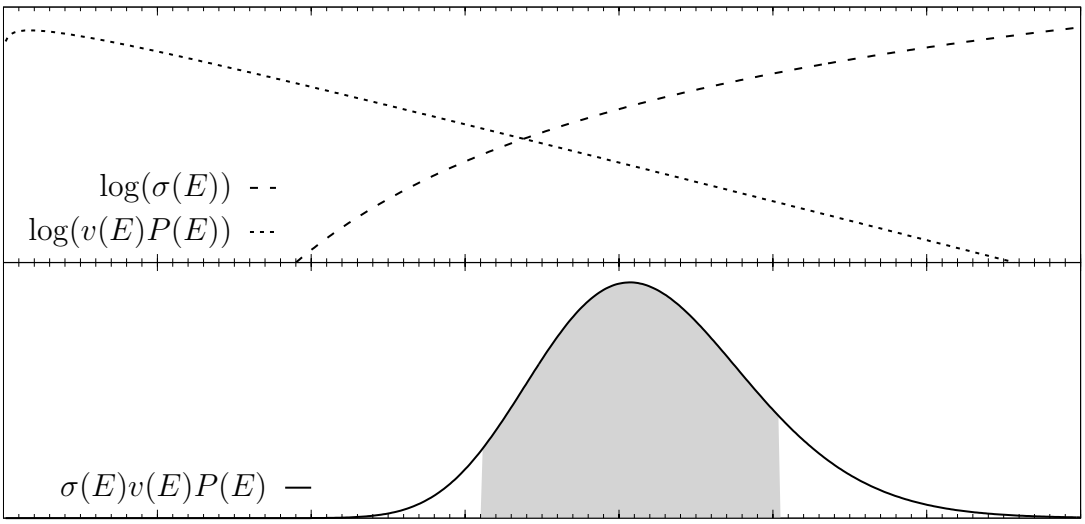


Figure 1.1: An example of how the cross section ($\sigma(E)$) and Maxwell-Boltzmann distribution ($P(E)$) combine to form a product which is peaked in one energy range, known as the Gamow window. The Gamow window is shaded.

Putting this all together, the stellar reaction rate that is typically tabulated is given by

$$N_{\mathrm{A}}\langle\sigma v\rangle = \sqrt{\frac{8}{\mu\pi}}\frac{1}{(k_{\mathrm{B}}T)^{3/2}}\int_0^\infty E\sigma(E)\exp(-E/k_{\mathrm{B}}T)\,\mathrm{d}E\,. \tag{1.7}$$

Even for very high astrophysical temperatures, the maximum of the Maxwell-Boltzmann distribution is at very low energies. At these low energies, the cross section of reactions that involve two charged particles is very low because of the Coulomb barrier. Figure 1.1 shows how the factors of the $v(e)\sigma(E)P(E)$ product vary over energy, resulting in a peak in the product. The energy region of this peak, which contributes the most to the integral of $\langle\sigma v\rangle$, is called the "Gamow window". To best determine the stellar reaction rate, it is important to measure the cross section as close to the Gamow window as possible.

To express the cross section in terms of the experimental parameters, we will consider the situation illustrated in Figure 1.2, in which a beam with velocity $v$ contained within the bounds of an area $A_b$ impinges upon a target contained in a volume bounded by an area $A_t$

and a thickness $x_t$. First, we count the number of reactions ($N_r$) and multiply the reaction rate from Equation (1.3) by the duration of observation ($t$).

$$N_r = Rt = \sigma n_b v n_t V t \tag{1.8}$$

The beam current density can be written as the beam intensity ($i_b$) divided by the beam area, i.e. $j_b = i_b/A_b$, and the target volume can be written as the product of its area and thickness, i.e. $V = A_t x_t$. This gives us

$$N_r = \sigma(i_b/A_b) n_t (A_t x_t) t. \tag{1.9}$$

However, we must only consider the area in which the beam and target overlap. If the beam is smaller than the target and $A_b$ completely overlaps $A_t$, we can limit $V$ to the volume of area $A_b$ and thickness $x_t$. This results in the following for the experimental measure of the cross section:

$$\sigma = \frac{N_r}{i_b n_t x_t t}. \tag{1.10}$$

### 1.2.1 Hauser-Feshbach

For reactions that proceed through an intermediate compound nucleus, the Hauser-Feshbach statistical model is commonly used to calculate nuclear cross sections. The results from this model are used for the $^{34}$Ar($\alpha$,p)$^{37}$K reaction rate in x-ray burst calculations.

In the case of a reaction $i^{\mu}(j,k)l^{\nu}$, and in which nuclei $i$ and $j$ are in states $\mu$ and $\nu$, the

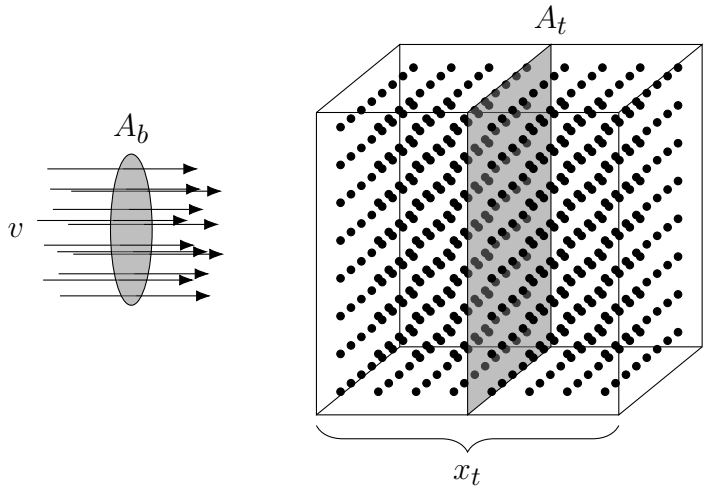


Figure 1.2: An illustration of the experimental scenario of a beam of particles impinging on a target. The beam travels through an area of $A_b$ with a velocity of $v$. The target occupies a volume of thickness $x_t$ and area $A_t$.

cross sections is expressed as

$$\begin{aligned}\sigma_{jk}^{\mu\nu}(E_{ij}) =& \frac{\pi\hbar^2}{2\mu_{ij}E_{ij}} \frac{1}{(2J_i^\mu+1)(2J_j+1)} \\ & \times \sum_{J\Pi}(2J+1)\frac{T_j^\mu(E,J,\Pi,E_i^\mu,J_i^\mu,\Pi_i^\mu)T_k^\nu(E,J,\Pi,E_l^\nu,J_l^\nu,\Pi_l^\nu)}{\sum_m T_m(E,J,\Pi)},\end{aligned} \tag{1.11}$$

where $E_{ij}$ is the center of mass energy; $\mu_{ij}$ is the reduced mass of the incoming projectile-target system; $E$, $J$, and $\Pi$ are the energy, total angular momentum and parity of a state, respectively; $T_j^\mu(E,J,\Pi,E_i^\mu,J_i^\mu,\Pi_i^\mu)$ is the transmission coefficient between the compound nucleus in state with the parameters $(E,J,\Pi)$ and particle $i$ in state $\mu$, which has the parameters $(E_i^\mu,J_i^\mu,\Pi_i^\mu)$ via emission or capture of particle $j$; and $T_m(E,J,\Pi)$ is the transmission coefficient for the emission of a particle $m$ to all possible final states. The individual transmission coefficients $T_j^\mu(E,J,\Pi,E_i^\mu,J_i^\mu,\Pi_i^\mu)$ are found by solving the Schrödinger equation

using an optical model. $T_m$ can be expressed as

$$\begin{aligned} T_m(E, J, \Pi) = &\sum_{\lambda=0}^{\omega} T_m^{\lambda}(E, J, \Pi, E_m^{\lambda}, J_m^{\lambda}, \Pi_m^{\lambda}) \\ &+ \int_{E_m^{\omega}}^{E-S_m} \sum_{J_m \Pi_m} T_m(E, J, \Pi, E_m, J_m, \Pi_m) \rho(E_m, J_m, \Pi_m)\, \mathrm{d}E_m \,, \end{aligned} \tag{1.12}$$

where $\omega$ is the highest known state in $k$, $S_m$ is the separation energy, and $\rho(E_m, J_m, \Pi_m)$ is the level density of the compound nucleus. This is split into two parts: a sum over all known states, and an integral over the level density to account for all remaining states. The sum in Equation (1.11) implies that, for any incoming energy $E_{ij}$, resonant states for any spin $J$ and parity $\Pi$ can be populated. This requires a sufficiently high level density in the compound nucleus at the energies of interest [15–20].

In the case of $^{34}\mathrm{Ar}(\alpha,\mathrm{p})^{37}\mathrm{K}$, the accuracy of Hauser-Feshbach predictions is in doubt. The critical level density at which it is appropriate to use the statistical model is estimated to be $(5\text{–}10)\,\mathrm{MeV}^{-1}$ [21]. In the excitation range of (6–12) MeV for $^{38}$Ca—the range populated in this experiment—the level density is near this threshold; however, the effective level density is lower when taking into account the fact that only natural parity states can be populated because the reactants are both even-even nuclei. If the level density is low, resonances from single levels play a larger role, and the statistical model breaks down.

The particulars of the optical model potentials used to calculate the transmission coefficients also greatly affect the Hauser-Feshbach predictions. Section 1.2.1 show some predictions of the cross section from the Hauser-Feshbach codes TALYS [22] and SMOKER [21]. This shows that predictions can vary by orders of magnitude.

Similar reactions have been directly measured and have found that the cross sections was significantly different than the Hauser-Feshbach predictions. The $^{23}\mathrm{Na}(\alpha,\mathrm{p})^{26}\mathrm{Mg}$ reaction

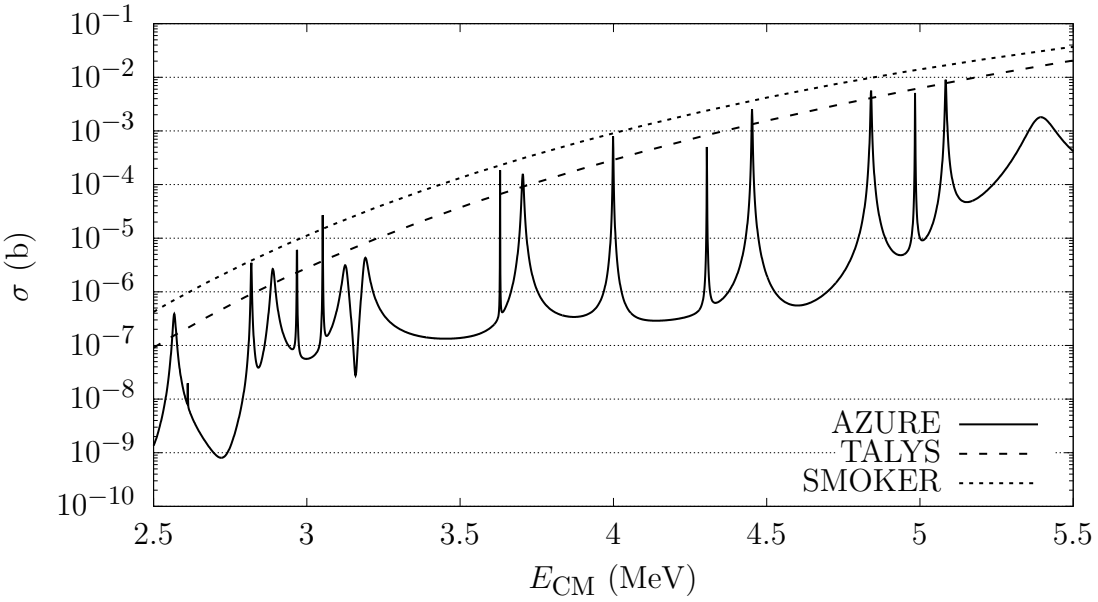


Figure 1.3: Predictions of the $^{34}$Ar(α,p)$^{37}$K cross section [21–23].

was directly measured [24], and it was found that the reaction rate is about a factor of 40 larger than the rate in the REACLIB database [25]. The $^{22}$Mg(α,p)$^{25}$Al reaction was also directly measured [26]; the cross section was found to be smaller that Hauser-Feshbach predictions by a factor of about 8, but the astrophysical reaction rate was found to be higher than rates determined by other indirect experimentally constrained methods by a factor of $10^3$ at 1 GK.

## 1.3 Measurement of $^{34}$Ar(α,p)$^{37}$K

The $^{34}$Ar(α,p)$^{37}$K reaction has never been directly measured before. There have been attempts to constrain the cross section using indirect methods; however, they have their limitations [26]. [27–30] used the $^{40}$Ca(p,t)$^{38}$Ca reaction to determine the excitation energies in $^{38}$Ca, the compound nucleus in the $^{34}$Ar(α,p)$^{37}$K reaction. These levels are important for determining the resonances of the reaction. Section 1.2.1 shows the cross section obtained

from this level information using the R-matrix code AZURE. The cross section is on average orders of magnitude lower than the Hauser-Feshbach calculations.

[31, 32] describe the measurement of the $^{37}$K(p,$\alpha$)$^{34}$Ar reaction, the time-inverse reaction of $^{34}$Ar($\alpha$,p)$^{37}$K. The time-inverse reaction can be used to calculate the forward reaction using detailed balance [33]. Preliminary results from [31] are an order of magnitude lower than the NON-SMOKER predictions for the $^{37}$K(p,$\alpha$)$^{34}$Ar cross section. The astrophysical reaction rate for $^{34}$Ar($\alpha$,p)$^{37}$K reported in [32] differs from Hauser-Feshbach predictions by 1 order of magnitude at 1 GK up to 3 orders of magnitude at 3 GK.

In this thesis, the first direct measurement of the $^{34}$Ar($\alpha$,p)$^{37}$K cross section was performed. To perform such a measurement, we must have a beam of either $^{4}$He or $^{34}$Ar impinging on a target of the other. Because $^{34}$Ar is radioactive, it is not feasible to have a $^{34}$Ar target. Therefore, we must perform the experiment in what is called the "inverse kinematics" frame, in which the heavier reactant is the projectile and the lighter reactant is the target. This requires a facility that can deliver radioactive beams. An advantage of conducting the experiment in the inverse kinematics frame is that the heavy recoil escapes the target and can be detected because the energy in the lab frame is so high. Additionally, the light ejectiles of the elastic scattering reaction are limited to only forward angles ($< 90°$), meaning that only ejectiles from ($\alpha$,p) reactions are seen at angles $> 90°$.

# Chapter 2

# Experimental Setup

NSCL experiment E15232 took place at the National Superconducting Cyclotron Laboratory (NSCL) from May 6 to May 19, 2016. It was designed to directly measure the cross section of $^{34}$Ar($\alpha$,p)$^{37}$K.

The NSCL provided a reaccelerated $^{34}$Ar radioactive beam. The JENSA system (see Section 2.2) was used to create a windowless supersonic $^{4}$He jet target intersecting with the beam. This system allows for a high target purity and for the reaction to happen at a precise location and energy. An ionization chamber was placed downstream of the target to detect the unreacted beam and the more massive reaction products (recoils). The protons produced in the reaction (ejectiles) were detected by an array of silicon detectors surrounding the target.

## 2.1 Beam Production

The experimental beam was produced via in-flight beam fragmentation, a process in which intermediate-energy nuclei impinging upon a target are broken up into smaller nuclei [34]. An $^{36}Ar^{7+}$ primary beam was created in the ECR ion source and sent to the K500 cyclotron. After being accelerated to 13.06 MeV/u in the K500, the beam impinged upon a 600 µg/cm$^2$ C stripping foil, producing an $^{36}Ar^{18+}$ beam. This beam then was accelerated to 150 MeV/u in the K1200 cyclotron, and impinged on a 1089 mg/cm$^2$ thick $^{9}$Be production

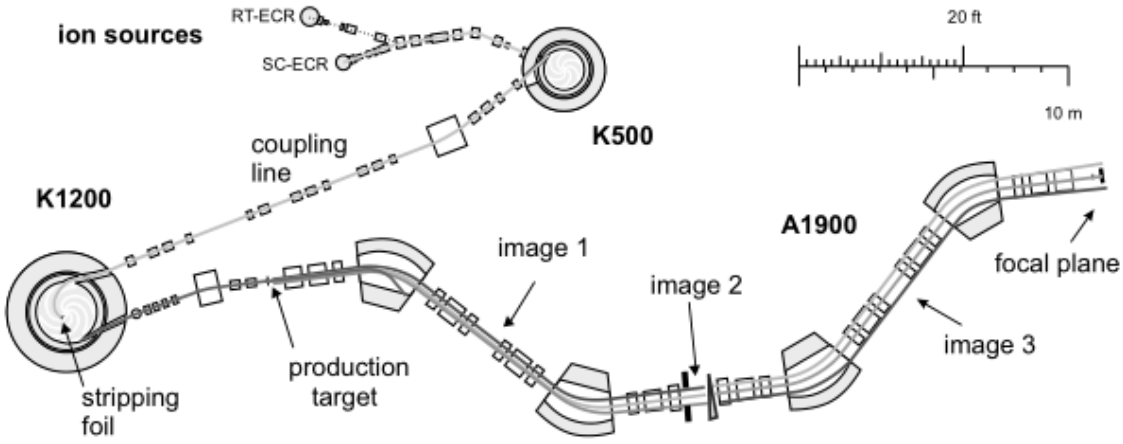


Figure 2.1: The Coupled Cyclotron Facility and the A1900 Fragment Separator.

target, producing a beam of a variety of nuclides.

$^{34}Ar^{18+}$ was extracted from this mixed beam using the A1900 separator [35]. The first two dipole magnets were set to select for nuclei with a magnetic rigidity of $B\rho = 2.745\,\mathrm{T\,m}$. The beam then passed through an energy-degrading wedge with an effective thickness of $148.296\,\mathrm{mg/cm^2}$, which changed the magnetic rigidity depending on element number. Finally, two more dipole magnets selected for nuclei with a magnetic rigidity of $2.617\,\mathrm{T\,m}$. This resulted in a beam of $55\,\%$ $^{34}Ar^{18+}$, with an energy of $93\,\mathrm{MeV/u}$ and a typical intensity of $6 \times 10^6$ pps.

The $93\,\mathrm{MeV/u}$ $^{34}Ar$ beam is too energetic to be relevant for the astrophysical site of interest. In order to deliver the beam at astrophysically relevant energies, it was stopped and re-accelerated to a lower energy. The beam was stopped using a system of two solid Al degraders and a linear gas cell. The first degrader had an effective thickness of $512\,\mu\mathrm{m}$ and the second degrader was wedge-shaped with an average effective thickness of $1710\,\mu\mathrm{m}$. The use of a wedge degrader is important because it allows particles with different energies, which are physically separated, to be degraded by different amounts. The degraders are able

to be rotated, which changes the effective thickness, i.e. $t_{\text{eff}} = t/\cos(\theta)$, where $t_{\text{eff}}$ is the effective thickness, $t$ is the thickness normal to the surface, and $\theta$ is the rotation angle. This allows for the energy degradation to be finely tuned [36–38]. The degraders were rotated by 37.0° and 28.5°. The beam then was stopped in a gas cell filled with 55 Torr of He and was extracted using a three-stage system of electrostatic fields, propulsion through a supersonic nozzle, and a radio frequency quadrupole (RFQ) [38, 39]. The entire system is located on a platform of high voltage, that accelerates the particles to the next stage.

The next stage of re-acceleration is charge-state breeding in the electron-beam ion trap (EBIT) [40]. The ions are decelerated as they approach the EBIT, which is on a high-voltage platform of up to 60 kV, injected into the EBIT at energies above the potential barrier, and then ionized by an electron beam before they can escape. The ions are charge bred for the selected ionization state and then extracted with an energy of (20–60) keV times the charge state by changing the potential barrier at the EBIT entrance. This method also causes the beam to be bunched, which is useful in the experiment for separating different events [40]. The beam is then accelerated to 600 keV/u in an RFQ. From there, a superconducting linear accelerator with three quarter-wave resonator cryomodules capable of accelerating or decelerating the beam to (0.3–6) MeV/u [41] accelerates the beam to the experimental energy.

The beam delivered to the experiment was $^{34}\text{Ar}^{15+}$, with a typical intensity of ($10^3$–$10^4$) pps at (5.5–5.9) MeV. The charge state of 15+ was chosen due to intensity and purity considerations. An $^{34}\text{Ar}^{18+}$ beam would be a good candidate, except that the low extraction efficiency would result in a beam intensity too low for the experiment; an $^{34}\text{Ar}^{17+}$ beam would be contaminated with many low-mass nuclides because $Q/A = 1/2$; and an $^{34}\text{Ar}^{16+}$ beam would be significantly contaminated with $^{17}\text{O}^{8+}$. $^{34}\text{Ar}^{15+}$ had a high extraction

efficiency and was only contaminated by the decay daughters $^{34}Cl^{15+}$ and $^{34}S^{15+}$.

The ideal energy at which to do the measurement would be in the Gamow window, the energy range over which most reactions occur for a reaction in an astrophysical environment and at specific astrophysical conditions (see Section 1.2) [42]. Using

$$E_0 = \left[ \left( \frac{1}{4\pi\epsilon_0} \right)^2 \left( \frac{\pi}{\hbar} \right)^2 \left( Z_0 Z_1 e^2 \right)^2 \left( \frac{m_{01}}{2} \right) (k_B T)^2 \right]^{1/3} \tag{2.1}$$

from [42], the Gamow peak is located at an energy of $E_0 = 2.035\,\mathrm{MeV}$ for $^{34}\mathrm{Ar}(\alpha,\mathrm{p})^{37}\mathrm{K}$ in a 1 GK x-ray burst. At this energy, however, it would take too long to conduct the experiment because the cross section is too low. The experimental energies were chosen to balance measuring as close to the Gamow peak as possible with obtaining a reasonably precise measurement. Using Hauser-Feshbach predictions for the cross section (see Section 1.2) and the predicted beam intensities, the center of mass energies of 6.12 MeV and 5.82 MeV were chosen so that 200 $^{34}\mathrm{Ar}(\alpha,\mathrm{p})^{37}\mathrm{K}$ reactions could be detected for each energy using 68 h and 103 h of beam time, respectively. These energies correspond to 1.71 MeV/u and 1.625 MeV/u in the lab frame. The actual beam energies delivered to the target during the experiment were slightly different; they were 1.68 MeV/u and 1.59 MeV/u.

The $^{34}$Ar beam delivered to the experiment was contaminated with the daughter and granddaughter nuclei, $^{34}$Cl and $^{34}$S. $^{34}$Ar decays into $^{34}$Cl with a half-life of 843.8 ms. $^{34}$Cl, in two states, decays into $^{34}$S with half-lives of 1.5266 s and 31.99 min [43], respectively.

Figure 2.2 shows an example spectrum that is used to identify the constituents of the beam. The different species can be identified by comparing their energy loss in different sections of the PSIC (see Section 2.3.2) because they have different stopping powers in isobutane. Typical fractions of $^{34}$Ar, $^{34}$Cl, and $^{34}$S were approximately 60 %, 30 %, and

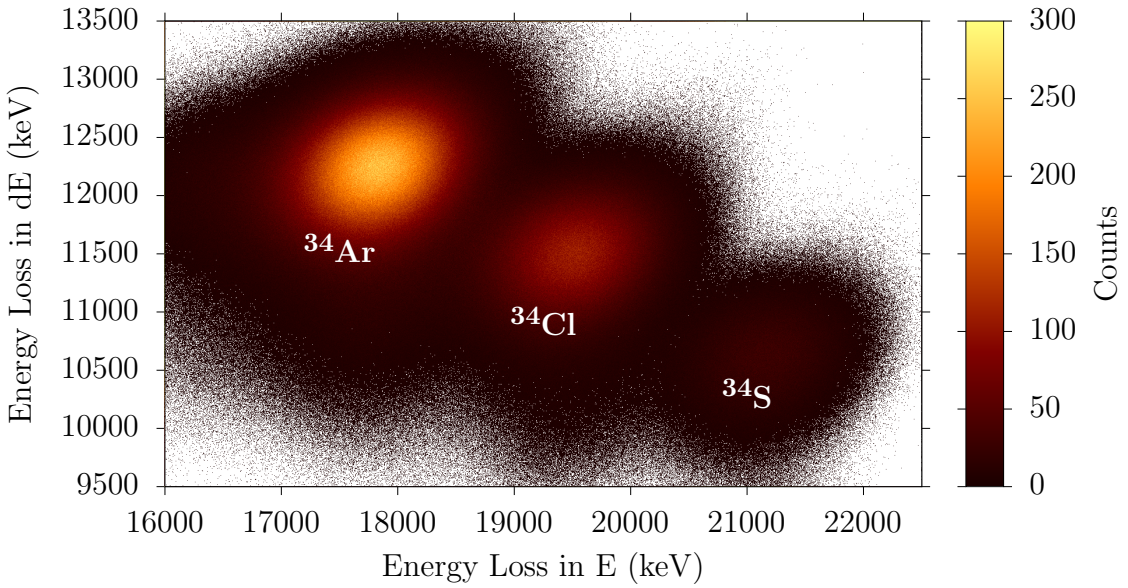


Figure 2.2: Spectrum showing the identification of beam species using the energy loss in two sections of the PSIC. The energy loss in the dE section is plotted against the energy loss in the E section.

10 %, respectively.

## 2.2 JENSA

The target was produced using the Jet Experiments in Nuclear Structure and Astrophysics (JENSA) gas jet target [44]. It is designed for studies in nuclear structure and nuclear astrophysics. For this purpose, JENSA was designed to be a windowless, dense, localized, recirculating, pure gas target. It is able to achieve an areal density of $9 \times 10^{18}$ atoms/cm$^2$, with a typical width of 5 mm and a standard distance between nozzle and catcher of 12 mm.

The fact that there is no window confers some benefits: the energy of the beam is not significantly affected before reaching the target, allowing for measurements at more precise energies; the beam experiences less angular straggling; and reactions occurring in a window, which would produce background, are avoided. A dense target allows for more reactions to

occur during the experiment, which allows for a greater sensitivity for lower cross section measurements. Because the target is localized, the position of the reaction is precisely known, which allows for more precise measurements of angular distributions. The fact that it is recirculating means that it saves gas, which is especially important when expensive gases are used. Target purity is important to avoid background from reactions with other target constituents or impurities. The gas jet target also has the advantage that there is no target degradation from the beam.

JENSA creates a supersonic jet by sending high-pressure gas through a nozzle into a vacuum chamber. The gas is collected in two conically-shaped catchers, which are pumped by multiple stages of pumps to a compressor. The compressor re-pressurizes the gas before it is sent to the nozzle again. A diagram of the pumping configuration can be seen in Figure 2.3, and typical values for the pressure gauges and other instruments can be found in Table 2.1.

The gas is compressed by a PDC-4-100-500 two-stage compressor system; the first compression stage is a PDC-4-100 compressor and the second is a PDC-4-500. Ballast tanks stabilize the pressure before, after and between the two compression stages.

The compressor requires at least 1 atm at its inlet to be able to operate. Normally, this pressure is maintained by the gas flowing through the nozzle, creating the jet target, and being pumped back to the inlet of the compressor. However, there are times during which it is either desired or necessary to not produce the jet and send gas through the pumping system. In order to maintain the required 1 atm in these situations, when the compressor is isolated from the pumping stages, a path was added for gas to flow directly from the outlet of the compressor back to the inlet. The amount of gas that flows through this path, which affects the pressure difference between the inlet and outlet, is controlled by a needle valve, $\mathrm{NV}_{\mathrm{loop}}$.

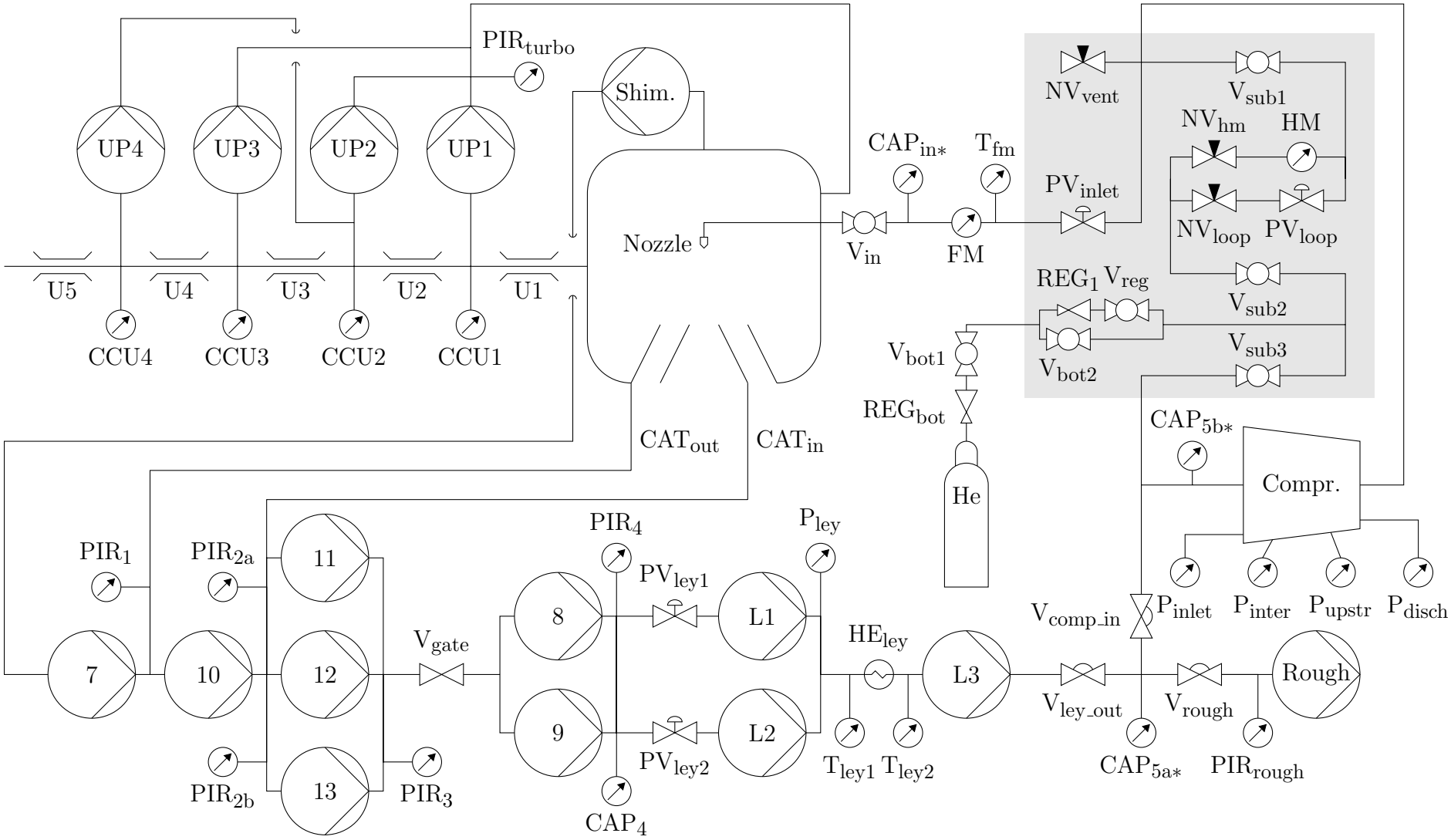


Figure 2.3: Diagram of the JENSA gas system.

Table 2.1: Typical values measured during a JENSA experiment.

| Gauge | Pressure (Torr) |
|---|---|
| $PIR_1$ | 1.2 [i] |
| $PIR_{2a}$ | _ [iv] |
| $PIR_{2b}$ | $> 1.5$ [i] |
| $PIR_3$ | $> 1.5$ [i] |
| $PIR_4$ | $> 1.5$ [i] |
| $CAP_4$ | 30 |
| $P_{ley}$ | $2 \times 10^2$ |
| $CAP_{5a}$ | 800 |
| $CAP_{5b}$ | 780 [ii] |
| $CAP_{in}$ | $1.5 \times 10^4$ [ii] |

| Gauge | Pressure (Torr) |
|---|---|
| $PIR_{turbo}$ | $2 \times 10^{-1}$ [i] |
| $PIR_{ch}$ | $1 \times 10^{-1}$ [i] |
| CCU1 | $1 \times 10^{-4}$ |
| CCU2 | $3 \times 10^{-5}$ |
| CCU3 | _ [iv] |
| CCU4 | $5 \times 10^{-7}$ |

| Gauge | Pressure (psig) |
|---|---|
| $P_{inlet}$ | 0.5 |
| $P_{inter}$ | 70 |
| $P_{upstr}$ | 320 |
| $P_{disch}$ | 300 |

| Instrument | Measurement |
|---|---|
| HM | _ [v] |
| FM | 29.5 CFM [iii] |
| $T_{ley1}$ | 40 °C |
| $T_{ley2}$ | 24 °C |
| $T_{fm}$ | 32 °C |
| $CAP_{ic}$ | 15 Torr |

[i] These pressures were measured with pirani gauges, the measurements of which are gas-dependent. During the experiment, the pressures measured were in the range for which pirani gauges provide inaccurate measurements [45]. pirani gauges reading (0.15–5) Torr could be corrected, but those reading $> 5$ Torr could only be corrected to $> 1.5$ Torr.

[ii] These pressures were measured with MKS Baratron Capacitance Manometers with a full range of (1–25 000) Torr operated by MKS vacuum gauge controllers with a full range of (1–20 000) Torr. Because of this, the measurement must be corrected by factor of 5/4, e.g. $CAP_{5a} = \frac{5}{4} CAP_{5a*}$. Measurements with a star (*) represent the uncorrected value, and those without a star indicate a corrected value.

[iii] Flow meter measurements depend on pressure, temperature, and specific gravity of the gas. The measurement is corrected for these factors using $FM = \frac{FM_*}{f_1 f_2 f_3}$, where $f_1 = \sqrt{\frac{114.7\,\text{psi}}{p}}$, where $p$ is the pressure in psi; $f_2 = \sqrt{\frac{T}{530\,\text{K}}}$, where $T$ is the temperature in K; and $f_3 = \sqrt{SG}$, where $SG$ is the specific gravity. Measurements with a star (*) represent the uncorrected value, and those without a star indicate a corrected value.

[iv] These gauges were not functioning properly during the experiment.

[v] This instrument, a hygrometer, was not used during the experiment.

From the compressor, there is a line going to the nozzle, where the pressure, flow, and temperature are measured by $CAP_{in*}$, FM, and $T_{fm}$. The gas then flows through a nozzle, creating a supersonic jet in the experimental chamber, and the jet is caught by two concentric catchers. The nozzle is threaded and screws into the nozzle receiver, and the catchers sit on top of larger receivers that connect to the pipes. These designs mean that the nozzle and catchers can be easily switched out with different designs. The nozzle used in this experiment was the E design (see Figure 2.5), and the inner and outer catchers had diameters of 20 mm and 30 mm, respectively. Using this setup, 90 % of the gas was caught in the inner catcher, 9 % was caught in the outer catcher, and 1 % escaped into the chamber.

The gas not collected by the catchers contributes to the ambient pressure of the experimental chamber. This gas is pumped out by a Shimadzu TMP-3203LMC-A1 turbomolecular pump, which is backed by one RUVAC WSU 501 roots vacuum pump. This is pumped into the outer catcher (pumping stage 1).

To return the gas to the 1 atm required to operate the compressor, there are multiple pumping stages between the jet and the compressor. The first stage, composed of one RUVAC WSU 2001 roots vacuum pump, pumps the gas from the outer receiver. The next stage, composed of three RUVAC WSU 2001, pumps this gas and also the gas from the inner receiver, which accounts for all of the gas in the system. Two RUVAC WSU 1001 comprise the next stage, and, as the final pumping stage, two DRYVAC DV 650, a heat exchanger, and one more DRYVAC DV 650 return the gas to the compressor.

To prevent gas from escaping into the beamline and contaminating the accelerator, as well as to prevent energy loss of the projectiles before interacting with the target, the system contains four stages of differential pumping upstream of the experimental chamber. Brass apertures were installed to restrict gas flow to the upstream pumping volumes. Between the

chamber and the first pumping volume, there was a 6 mm aperture; between the first and second, there was an 8 mm aperture; and between the third and fourth, there was a 12 mm aperture. The apertures were kept as small as possible to prevent gas flow to the upstream pumping volumes as much as possible without blocking the beam. Since the beam is focused at the target location, the beam diameter is larger when it is further from the target; because of this, the aperture sizes change with distance along the beamline. The first two volumes are pumped with a TURBOVAC 1000 C turbomolecular pump back into the chamber; the third is pumped with a TURBOVAC 600 C into the chamber; and the fourth is pumped with a TURBOVAC 600 C into the second pumping volume. Finally, the ReA3 beamline is separated from the JENSA beamline by an interlocked gate valve; if CCU4 $> 1 \times 10^{-5}$ Torr, the gate valve automatically closes.

See Appendix A for JENSA operating instructions.

### 2.2.1 Jet Characteristics

Ahead of the experiment, some tests were performed to determine the characteristics of the jet. Areal density, size of the jet, and pressures along the beamline were measured for different nozzles, receivers, and pumping configurations.

The areal number density of the target, $\rho_A$, is an important quantity for calculating the reaction cross section (see Section 3.6). It is defined as

$$\rho_A(x, y) = \int \rho(x, y, z)\, \mathrm{d}z\,, \tag{2.2}$$

where $\rho$ is the volumetric density, $x$ and $y$ are the coordinates orthogonal to the beam axis, and $z$ is the coordinate parallel to the beam axis.

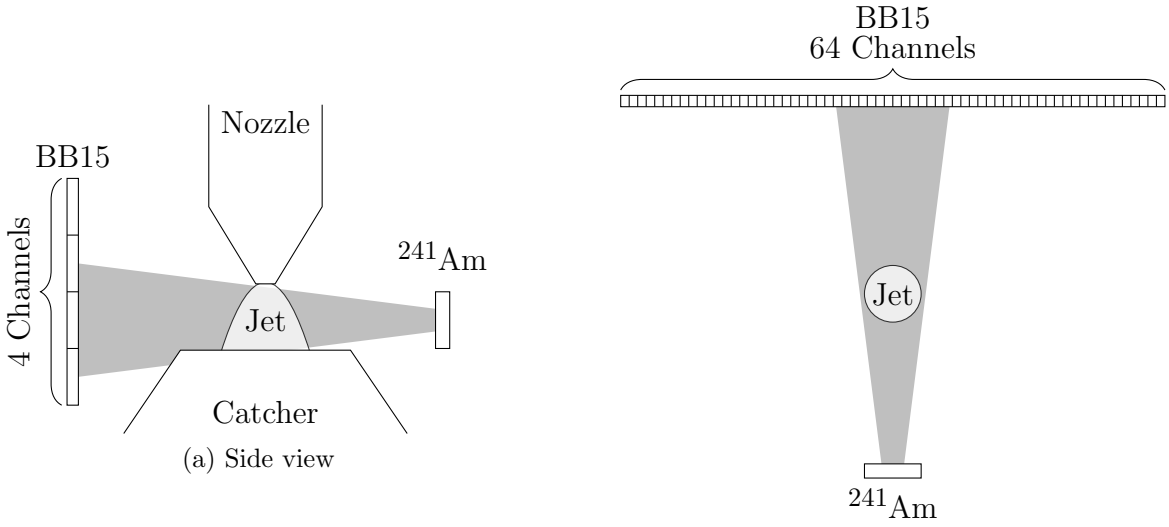


(a) Side view

(b) Above view

Figure 2.4: These diagrams show the setup for measuring the areal density of the jet. On opposite sides of the jet are a $^{241}$Am α-particle source and a Micron BB15 silicon detector. The difference in energy of the detected α-particles between runs with and without a jet is used to determine the areal density of the jet. The detector's 64 front-side channels allow for the areal density to be measured in the left-right direction, and the four back-side channels allow for it to be measured in the up-down direction. (a) shows the setup from the side, and (b) shows the setup from above.

The areal density of the jet was determined by measuring the energy loss of 5.486 MeV α-particles [46] emitted by an $^{241}$Am source. This was done by measuring the energy deposited by the α-particles in a Micron BB15 silicon detector without a jet being produced and then measured again with the jet. The setup is shown in Figure 2.4. He in He energy loss data [47] was then used to calculate the areal density of the jet using

$$\rho_A = S(E) \cdot \Delta E, \tag{2.3}$$

where $S(E)$ is the stopping power of α-particles in He gas at energy $E$ and $\Delta E$ is the measured energy loss.

Because of the spatial resolution of the detector (see Section 2.3), the radial distribution

of the areal density could be determined. Two strips along the jet axis determined how the jet expands as it moves away from the nozzle.

These tests also allowed us to see how the distribution changed with different nozzle designs [48]. The nozzle chosen for this experiment, shown in Figure 2.5, was the nozzle which produced the most dense jet at the reaction location. The resulting jet had an areal density of $6 \times 10^{18}$ atoms/cm$^2$, and a width of 5 mm for $P_{disch} = 250$ psig. These data were used as the calibration for the relationship between $CAP_{in}$ and the areal density of the jet during the experiment. See [48], [44], and Section 3.6 for more detailed explanations of measuring the areal density of the jet.

The gas pressure outside of the jet along the beam axis is important for two main reasons. The pressure past the last pumping stage must be below $10^{-5}$ Torr, so that the gas does not affect beam transport or disrupt the operation of the reaccelerator. Also, the pressure up to the target should be as low as possible to minimize the energy loss and energy spread before the beam reaches the target and to prevent reactions outside of the jet area.

The pressure along the beamline was measured for different sizes of the catchers into which the jet flowed. The catchers tested were outer catchers with diameters of 20 mm, 25 mm, and 30 mm and inner catchers with diameters of 10 mm, 15 mm, and 20 mm. Table 2.2 shows the results of these tests. The pressure was measured at CCD4 and at a compressor discharge pressure ($P_{disch}$) of 300 psig. CCD4 records the pressure in the fourth pumping stage downstream of the jet. The 30 mm outer catcher and 20 mm inner catcher were used in the experiment to minimize the pressure outside of the jet.

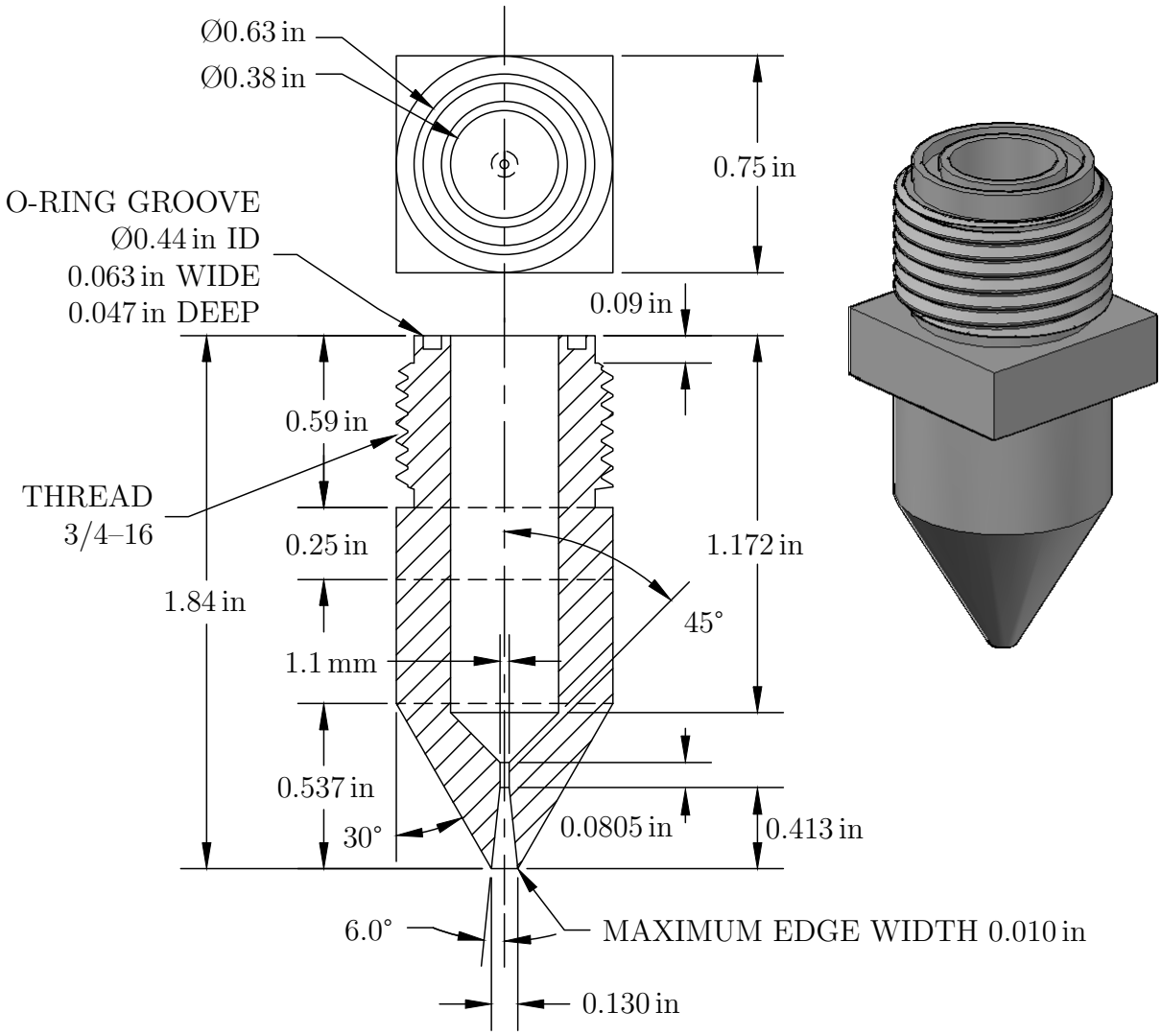


Figure 2.5: The nozzle used in this experiment.

Table 2.2: The pressures measured at CCD4 for different catchers with a compressor discharge pressure ($P_{disch}$) of 300 psig.

| Catcher Diameter | | |
|---|---|---|
| Outer (mm) | Inner (mm) | Pressure (μTorr) |
| 20 | 10 | 23 |
| 20 | 15 | 23 |
| 20 | 20 | 23 |
| 25 | 10 | 9.4 |
| 25 | 15 | 1.5 |
| 25 | 20 | 2.1 |
| 30 | 10 | $> 170$ [i] |
| 30 | 15 | 1.6 |
| 30 | 20 | 1.5 |

The pumping configuration of the turbomolecular pumps along the beamline was changed to minimize the pressure in the fourth differential pumping stage. Two competing factors were at play. Pumping gas into another pumping stage increases the pressure in that stage; however, a turbomolecular pump's pumping efficiency is affected by the pressure at its exhaust. Therefore, it is possible that the increase in pumping efficiency outweighs an increase in pressure at a prior pumping stage along the beamline. These tests led to switching from Figure 2.6a, in which all pumps exhaust into the main chamber, to Figure 2.6b, in which the exhaust of UP4 feeds into the cavity pumped by UP2.

[i] The pressure given is a lower limit because the roots blower pumps overloaded before reaching 300 psig.

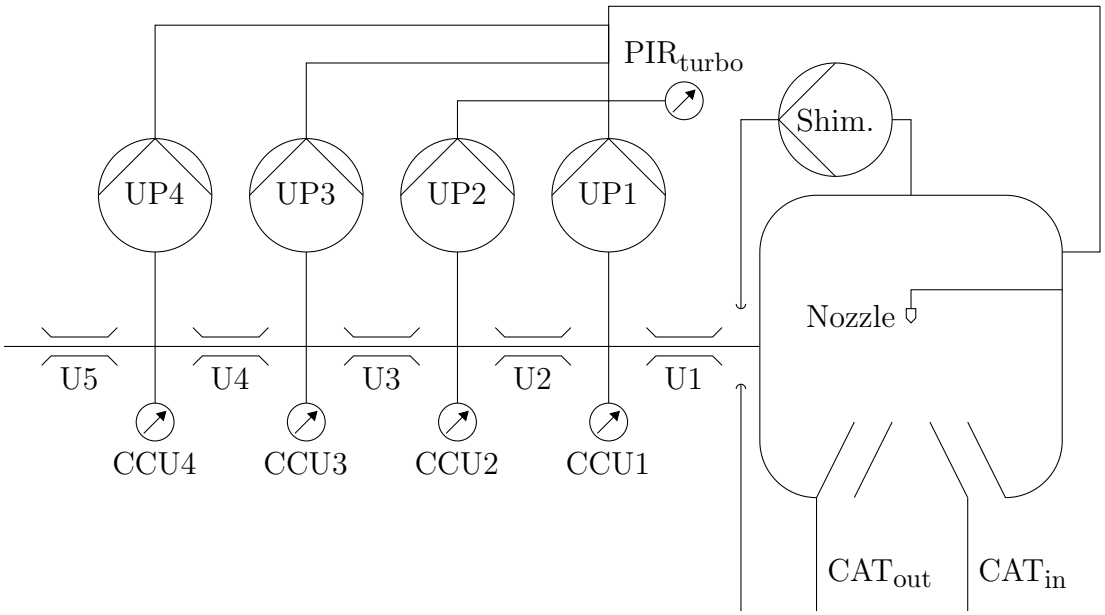


(a)

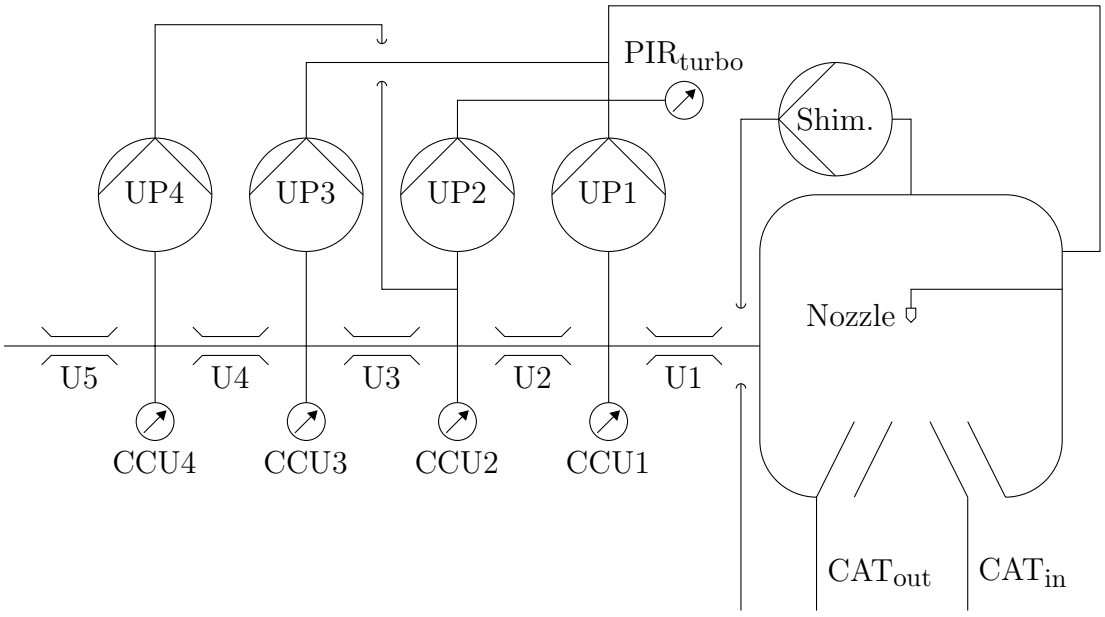


(b)

Figure 2.6: Two pumping configurations tested to decrease the pressure at CCU4. (a) shows the first approach in which the exhaust of all pumps feed into the main chamber. (b) shows the configuration used in the experiment in which the exhaust from UP4 feeds into the cavity pumped by UP1.

## 2.3 Detectors

The detector setup, shown in Figure 2.7, was designed by considering the reactions that were expected to occur: (α,α) and (α,p) induced by each beam species. Because the heavy recoils are emitted in a small forward-focused cone and because of the high beam rate, an ionization chamber was placed downstream of the target along the beam axis to detect the heavy recoils and unreacted beam. The light ejectiles, however, are emitted in a much wider range of directions, so an array of silicon detectors was installed surrounding the target. Figure 2.8 shows the energies and angles at which the particles are emitted.

### 2.3.1 Silicon Detector Array

The silicon detector array is designed to detect the light ejectiles, α-particles and protons. As shown in Figure 2.8, only protons are emitted at polar angles of $\theta > 90°$, but at polar angles of $\theta < 90°$, both α-particles and protons are emitted. In this range where both species are seen, they are distinguished using particle identification telescopes. These "telescopes" consist of two detectors each: a thin one in which the particle loses some of its energy and a thick one in which it loses its remaining energy. Because the stopping power of different

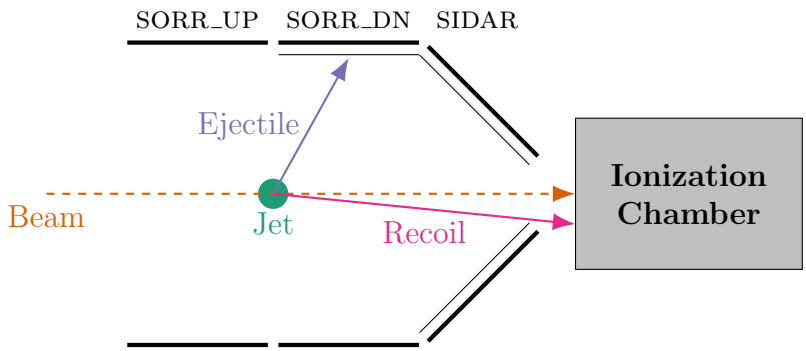


Figure 2.7: A diagram of the detectors used in the experiment and the reaction products they detect.

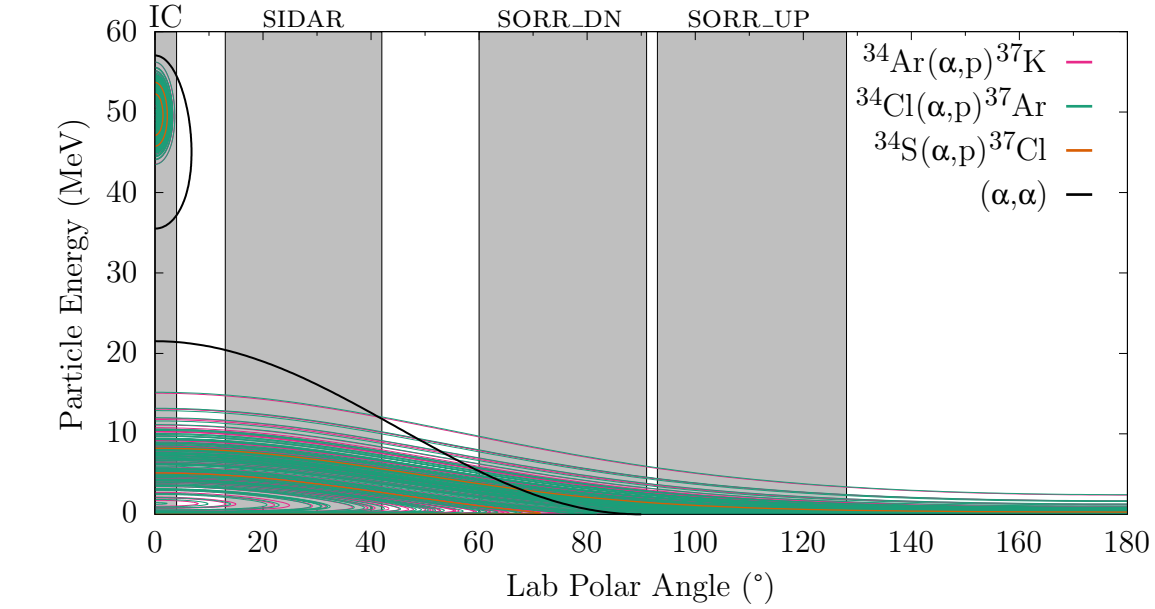


(a)

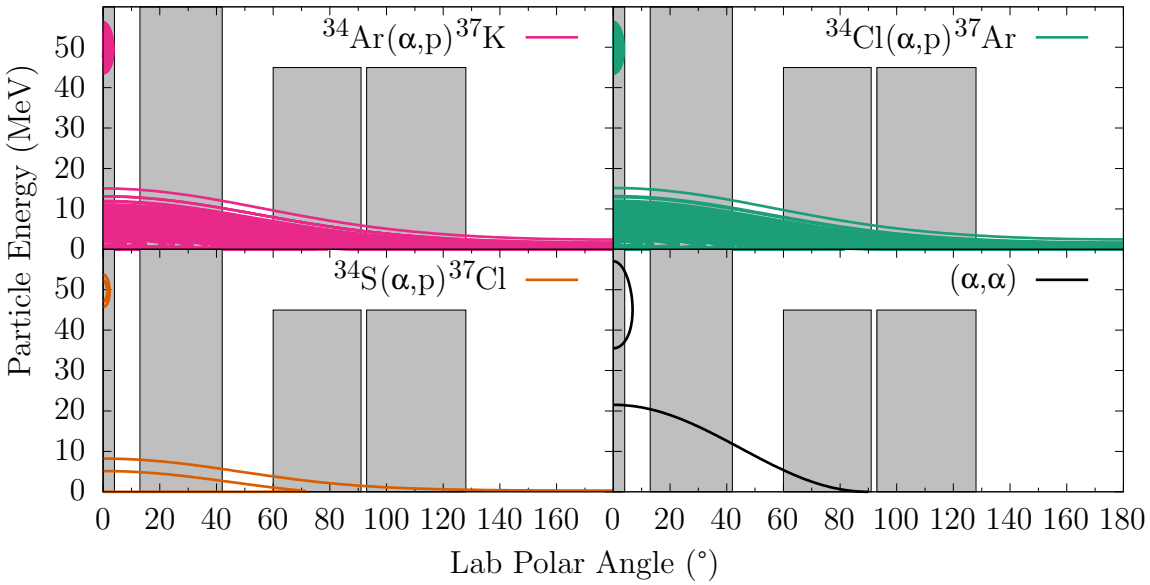


(b)

Figure 2.8: The relationship between particle energies and the polar angle at which they are emitted for the reactions that occur in this experiment. (a) shows the different reactions together, and (b) shows them separately. The angular ranges that are covered by detectors are shown. The high energy ($> 30\,\text{MeV}$) lines correspond to the recoils, and the low energy ($< 30\,\text{MeV}$) lines correspond to the ejectiles. For each (α,p) reaction, there are multiple levels that can be populated in the recoil nucleus, and for each of these levels, there is a different relationship between energy and angle. For elastic scattering, this is not the case, so there is only one line per particle.

species of charged particles in the detector material is different, the relationship between the energy loss in the two detectors can be used to determine the species of the ejectile.

The array uses detectors from the Oak Ridge National Laboratory SuperORRUBA [49] and SIDAR [50] arrays, and consists of three sections: SORR_UP, SORR_DN, and SIDAR. Figure 2.9 shows the names and positions of the detectors. The detectors numbers count up clock-wise starting with the upstream detectors (detectors numbered 5 and 12 were removed before the experiment started). Detectors labeled E$N$ are detectors thick enough for particles to be stopped in them, and the back-sides of those detectors are labeled bE$N$. Detectors labeled dE$N$ are thin detectors in a telescope setup.

The SORR_UP section of the array covers lab polar angles 90° to 130°. Because the detectors are fully upstream of the target, the α-particles from elastic scattering are not seen in these detectors. Because there is no need to distinguish between (α,α) and (α,p) and because the energy of the protons are $< 6$ MeV, only one layer of detectors was used. Therefore, six 1 mm thick BB15 detectors were used in this section.

The SORR_DN section of the array covers lab polar angles 60° to 90°. In this polar angle range, both protons and α-particles are seen. Because of this, telescopes must be used to distinguish between the two. One part of this section, SORR_DNT, consists of four telescopes, each with a 60 µm thick Micron BB10 detector in front of a 1 mm thick Micron BB15 detector. The other part, SORR_DNS, consists of two single-layer detectors. This setup was chosen because detecting the α-particles from elastic scattering would be useful for beam normalization, but near 90°, where the cross section is highest, the energy is so low that they would be stopped in the first layer, and the energy deposited would be hard to distinguish from the noise.

The SIDAR section of the array covers lab polar angles 10° to 35°. In this polar angle

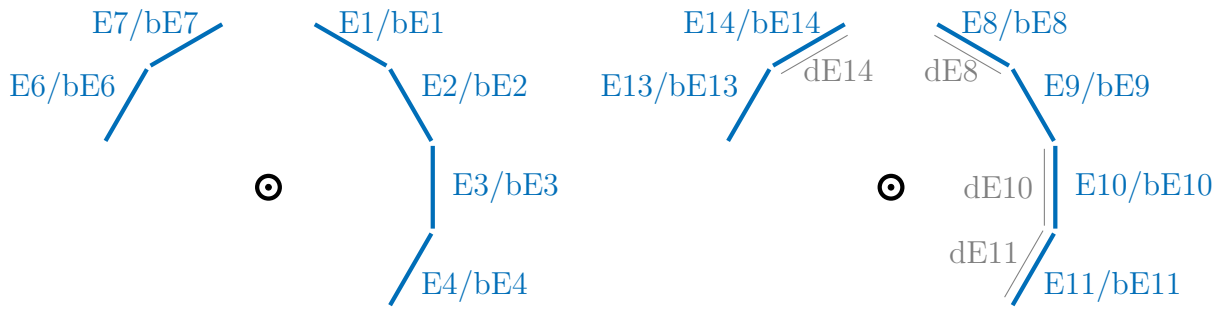


(a) SORR_UP (b) SORR_DN

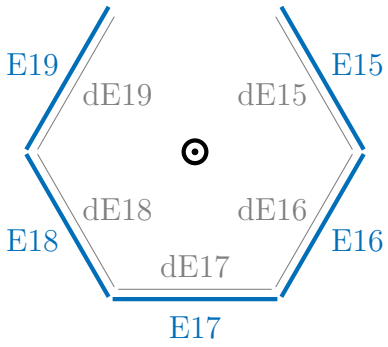


(c) SIDAR

Figure 2.9: The silicon detector array used in this experiment, looking upstream, toward the source of the beam. The detector naming counts up going clockwise, starting at the upstream section and repeating for each subsequent downstream section. Detectors 5 and 12 were removed to accommodate jet and beam tuning hardware.

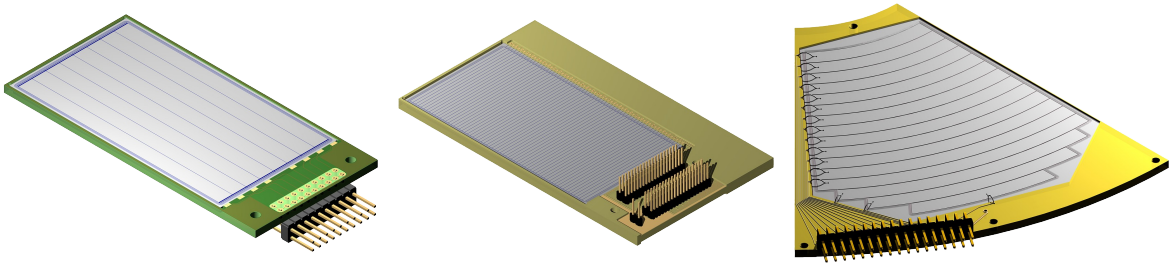

(a) (b) (c)

Figure 2.10: The silicon detectors used in this experiment are (a) 4 60 µm-thick Micron BB10s, (b) 12 1 mm-thick Micron BB15s, and (c) 5 60 µm-thick and 5 1 mm-thick Micron YY1s.

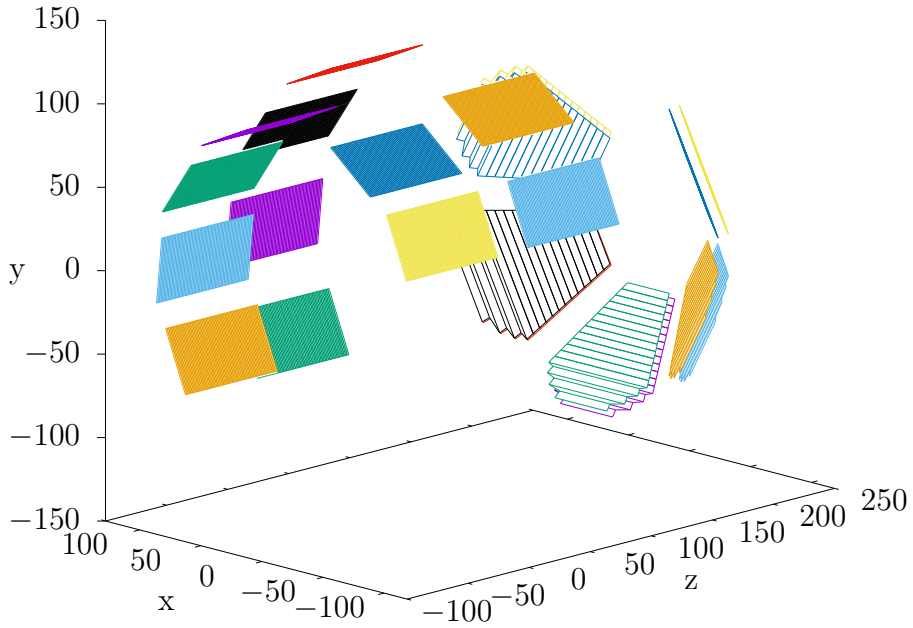


Figure 2.11: The positions of the silicon detectors in the experiment. The z-axis is the beam axis and the y-axis is the jet axis, meaning the reaction location is at the origin.

range, both protons and alphas are seen, so a two-layer setup of 60 µm and 1 mm Micron YY1 detectors were used.

### 2.3.2 Position-Sensitive Ionization Chamber

The ANASEN position-sensitive ionization chamber (PSIC) [51, 52] was placed at the end of the beamline to detect the recoils and beam particles. The PSIC consists of a series of electrode grids stacked along the beam axis, with a separation of 18.3 mm between neighboring grids. The grids alternated between grounded electrodes and electrodes that were biased at 150 V. These grids were separated into four sections. The first two, X and Y, were position sensitive; they each consist of 32 channels that read out signals from individual grid wires separately. The different channels correspond to different left-right positions in the X section and different up-down positions in the Y section. The following sections, dE

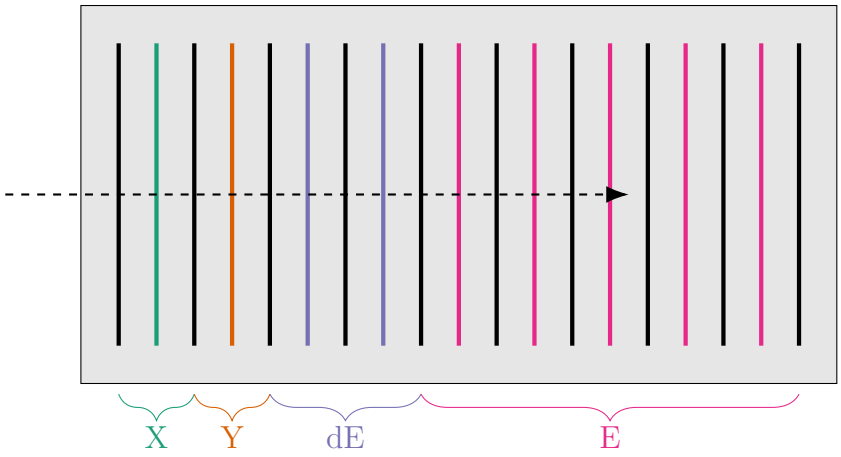


Figure 2.12: A diagram showing the different sections of the ionization chamber. Each signal is read from a wire or set of grids biased at 150 V. The biased grids have grounded grids between them. The X and Y sections consist of 32 channels each, which allows for the calculation of the outgoing angles of the recoils. The dE and E sections consist of 1 channel, which combines the signal from multiple grids, each.

and E, consisted only of one signal each. The dE section combined the signal from two biased electrodes, and the E section combined the signal from five biased electrodes. Figure 2.12 illustrates this configuration. The chamber was filled with 15 Torr of isobutane. This was chosen over carbon tetrafluoride to optimize for energy resolution and separation of different beam species in the E section.

## 2.4 Data Acquisition

Multiple data acquisition systems were used in this experiment: the Experimental Physics and Industrial Control System (EPICS) [53, 54] was set up to record continuous time series data of pressure gauges and beam currents throughout the experiment, and the NSCLDAQ system [55, 56] was set up to record the signals from the detectors. The data can be correlated because the EPICS data is stored with an absolute timestamp for each point, and the NSCLDAQ data has an absolute timestamp at the start of each run and a relative

timestamp for each event in that run.

The EPICS data recorded gauge measurements during the experiment. The most important measurements were $CAP_{in}$, and $CAP_{ic}$. $CAP_{in}$ corresponds to the pressure just before the nozzle, which is important because it is correlated to the density of the jet (see Section 3.6). $CAP_{ic}$ corresponds to the pressure in the ionization chamber, which is important because it affects the energy that particles lose while traveling through the ionization chamber.

Two independent NSCLDAQ data streams were combined to create the final event data stream for the experiment. The silicon detector data were recorded in the VME stream, which specializes in recording a large number of channels. The PSIC data were recorded in the DDAS stream, which specializes in recording signals with high data rates.

The silicon detector array (described in Section 2.3.1) was composed of 12 BB15 (64 front-side and 4 back-side channels each), 4 BB10 (8 front-side channels each), and 10 YY1 detectors (16 front-side channels each). This results in 1008 channels total. To record so many channels, the detectors were fed into a system of HINP16C application-specific integrated circuits (ASICs) [57]. Each HINP16C chip consists of 16 channels. Each channel has a charge sensitive amplifier, which is split and sent to two circuits: one for fast processing of timing information and one for slow processing of energy information. Two chips were combined on one chipboard, and up to 10 chipboards were connected to a motherboard. The energy signals for each motherboard are sent to a JTEC Model XLMXXV module to be digitized and then sent to a data acquisition computer via a VMEBus. The timing signals were combined as described in Section 2.4.1 to create signals triggering the readout of the data acquisition system.

The DDAS system, which was composed of XIA Pixie-16 modules, was used for two

reasons: because 1) the PSIC detected the beam and recoils and 2) there were relatively few channels.

### 2.4.1 Trigger Logic

Combining two independent NSCLDAQ systems means that care must be taken to ensure the two systems are synchronized. To do this, a 100 Hz pulser is fed into both systems and used as a clock. This requires the DDAS system to be configured to accept an external timestamp and the VME system to be configured to use a scaler module as the timestamp. The setup of the electronics is shown in Figure 2.13.

In the ASICs system, the motherboards are configured to send a trigger signal when the front side of a silicon detector receives a signal. When this happens, we want to record signals from all other channels that also received a signal, whether they were configured to send a trigger or not. To do this, the logical OR of the motherboard triggers is sent to the XLMXXV modules to start trigger the processing and recording of the signal. This signal is vetoed if any of the XLMXXV modules are not ready. In order to not lose data, the VM-USB must wait until each XLMXXV module has received and processed data for that event before sending the data to the data acquisition computer. The XLMXXV sends a complete signal when it finishes processing data, and these are used to create a signal to trigger the VM-USB module to send the data to the data acquisition computer. The complete signal from each XLMXXV is sent to its own latch module as the start signal. The VM-USB trigger is the logical AND of these signals. This signal is sent to the VM-USB module to trigger read-out, but also is sent to the latch modules as the stop signal. Altogether, this means that once all motherboard signals have been processed, the data is sent to the data acquisition computer, and the system is ready for the next event.

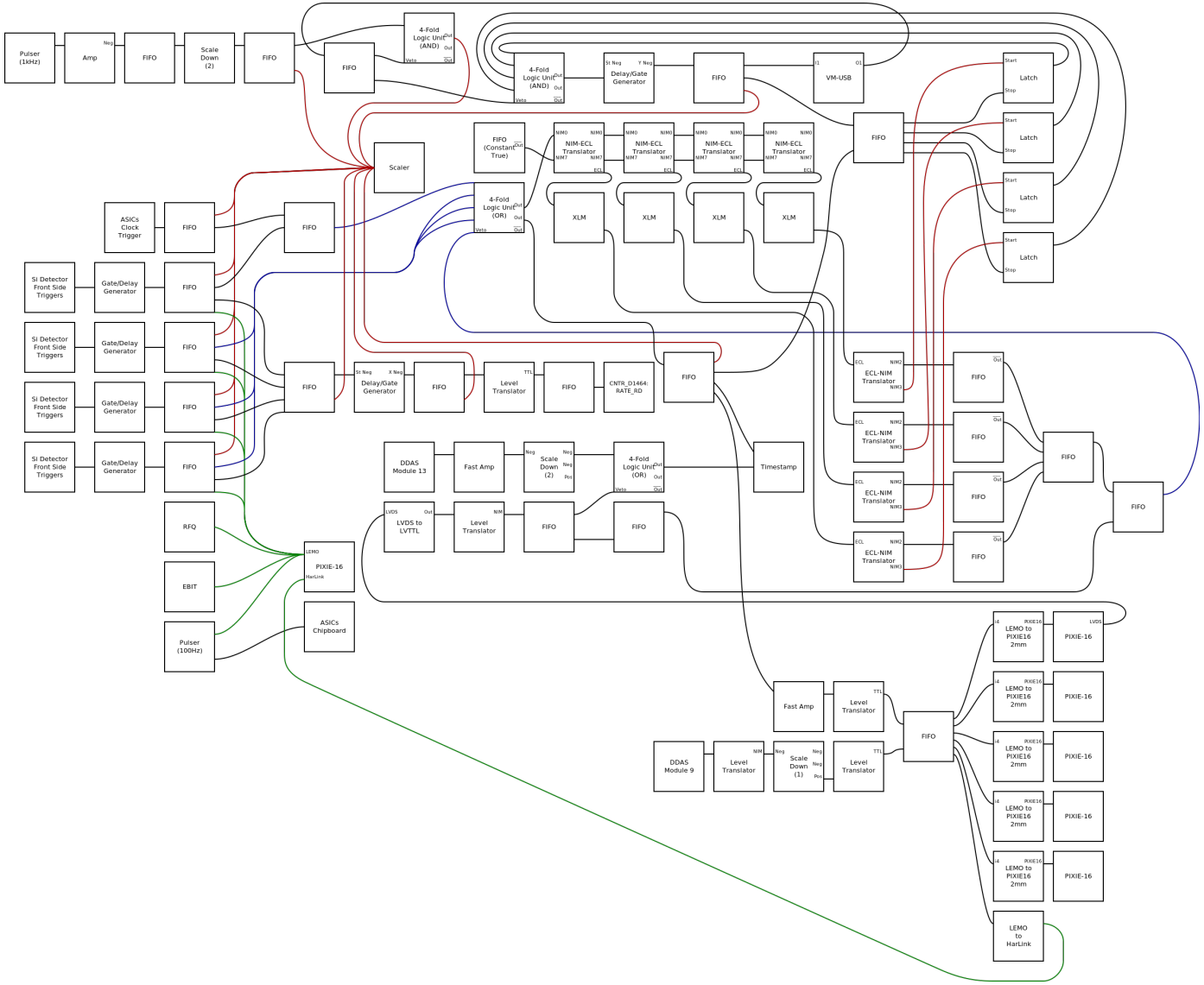


Figure 2.13: A diagram showing the electronics used to produce the signals used to trigger the data acquisition systems to record data.

A problem can occur if the signals are not grouped properly into events. For example, if for some reason one complete signal is missing, the latches will be open until the missing complete signal occurs in the next event. This causes an error to occur in the next event, which propagates to all subsequent events. To prevent this, the OR of the motherboard triggers is also used to stop the latches. Figure 2.14 shows an illustrated example of how these signals are combined to create the VM-USB trigger and how the OR of the motherboard triggers is used to fix errors that can occur with missed signals.

See Appendix A of [58] for a more detailed explanation of the ASICs setup.

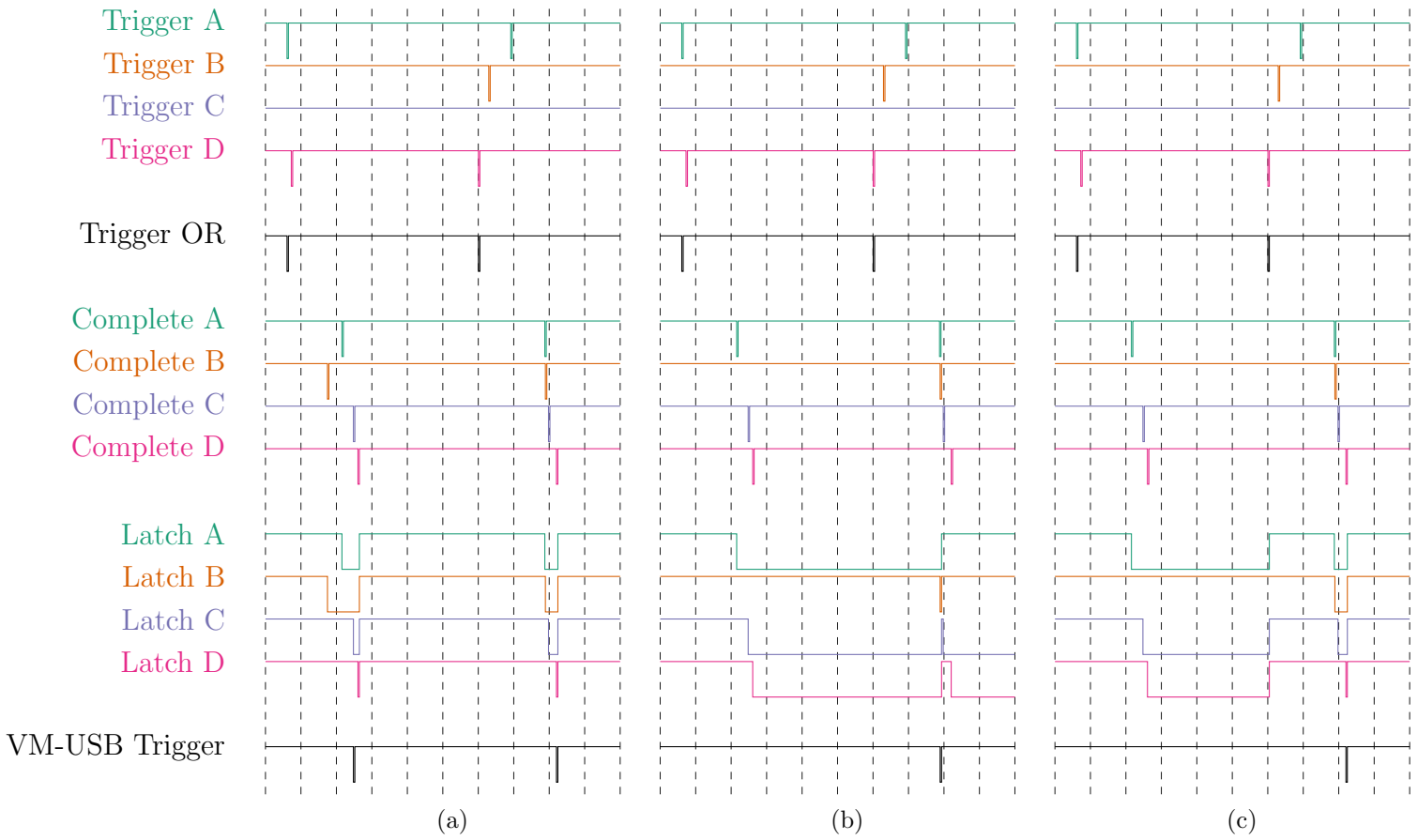


Figure 2.14: An example showing how the four ASICs motherboard triggers are combined to create the VM-USB trigger. (a) shows two events during normal operation. (b) shows how a missing complete signal can propagate errors to subsequent events. (c) shows how the OR of the motherboard triggers can be used to prevent this error from propagating to other events.

# Chapter 3

# Analysis

## 3.1 Beam Energy

The experiment was conducted at two experimental energies. At the first energy—the higher of the two—an $^{34}Ar^{15+}$ beam with a total kinetic energy of $(57.04 \pm 0.75)$ MeV was delivered to the target. At the second, the $^{34}Ar^{15+}$ beam had a total kinetic energy of $(54.19 \pm 0.73)$ MeV.

The reaccelerator accelerates particles to the same velocity. Because $E = \frac{1}{2}mv^2$, $E/m$ is the same for each species, and the total kinetic energy for particle $x$ is $E_x = \frac{m_x}{m_{^{34}\mathrm{Ar}}} E_{^{34}\mathrm{Ar}}$.

While traveling through the target, the beam loses energy. This means that the average energy at which reactions occur is less than the beam energy. The energy loss of the beam constituents through $10^{19}$ atoms/cm$^2$ of He was calculated using ATIMA [59]. For a thin target, the average energy of the beam in the target is the incoming energy minus half of this energy loss. This is not necessarily the average beam energy at which reactions happen because the cross section may change much within the energy range of the target; this is particularly true if the cross section exhibits resonances. The various beam energies are shown in Table 3.1.

Table 3.1: The experimental beam energies.

| | Beam Species | Energy Before Target (MeV) | Energy Loss in Target (MeV) | Average Lab Energy (MeV) | Average Center of Mass Energy (MeV) |
|---|---|---|---|---|---|
| E1 | $^{34}S^{15+}$ | $57.02 \pm 0.75$ | $1.649 \pm 0.007$ | $56.20 \pm 0.75$ | $5.924 \pm 0.079$ |
| | $^{34}Cl^{15+}$ | $57.03 \pm 0.75$ | $1.790 \pm 0.007$ | $56.14 \pm 0.75$ | $5.917 \pm 0.079$ |
| | $^{34}Ar^{15+}$ | $57.04 \pm 0.75$ | $1.932 \pm 0.007$ | $56.07 \pm 0.75$ | $5.909 \pm 0.079$ |
| E2 | $^{34}S^{15+}$ | $54.17 \pm 0.73$ | $1.674 \pm 0.007$ | $52.50 \pm 0.73$ | $5.534 \pm 0.077$ |
| | $^{34}Cl^{15+}$ | $54.18 \pm 0.73$ | $1.817 \pm 0.007$ | $52.36 \pm 0.73$ | $5.519 \pm 0.077$ |
| | $^{34}Ar^{15+}$ | $54.19 \pm 0.73$ | $1.960 \pm 0.007$ | $52.23 \pm 0.73$ | $5.504 \pm 0.077$ |

## 3.2 Detector Solid Angles

Accurately knowing where the detectors were positioned with respect to the target is important for determining the fraction of reactions that was actually observed during the experiment. How much solid angle was covered and the angles at which the detectors were positioned were calculated analytically using a program written for this purpose [60].

The first step is to describe the surface of the detector as a function of two coordinates. A coordinate system to describe the location of the detector surface, $\mathbf{r_0}(u, v)$, is chosen for each individual detector so that one coordinate is constant along each edge of a detector strip. This condition simplifies integration over the surface. To satisfy this condition, the CartesianZ coordinate system (Equation (3.1)) was used for the BB10 and BB15 detectors, and the PolarZ coordinate system (Equation (3.2)) was used for the YY1 detectors. These coordinate systems are show in Figure 3.1.

$$\text{CartesianZ:} \quad \mathbf{r_0}(u, v) \coloneqq \langle u, v, 0 \rangle \tag{3.1}$$

$$\text{PolarZ:} \quad \mathbf{r_0}(u, v) \coloneqq \langle u \cos(v), u \sin(v), 0 \rangle \tag{3.2}$$

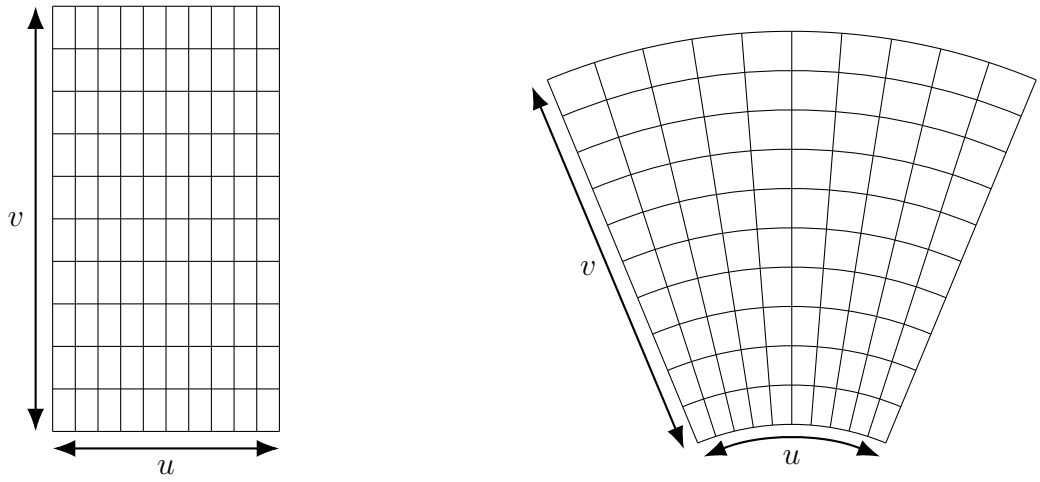


(a) BB10s and BB15s

(b) YY1s

Figure 3.1: The coordinate systems used to describe BB10s and BB15s (a) and YY1s (b).

Next, the detector surfaces $\mathbf{r_0}(u, v)$ described in their individual local coordinate systems are transformed into surfaces $\mathbf{r}(u, v)$ in a common coordinate system that describes the entire setup. This common coordinate system is one in which: the reaction location is the origin, the $z$-axis is the beam axis, the $x$-axis is the horizontal axis perpendicular to the beam axis, and the $y$-axis is the vertical axis perpendicular to the beam axis. Two types of transformations are used here: translation and rotation. The translation operation has one parameter: the displacement $\mathbf{d}$, and it is defined as

$$\mathrm{T}(\mathbf{d})\mathbf{r} = \mathbf{r} + \mathbf{d}. \tag{3.3}$$

The rotation operator has two parameters: a unit vector $\hat{\mathbf{u}}$, which—along with the origin—

describes the axis of rotation and the angle of rotation $\theta$. It is defined as

$$\mathrm{R}(\hat{\mathbf{u}},\theta)\mathbf{r} = \begin{pmatrix} u_x^2+(1-u_x^2)\cos\theta & u_xu_y(1-\cos\theta)-u_z\sin\theta & u_xu_z(1-\cos\theta)+u_y\sin\theta \\ u_xu_y(1-\cos\theta)+u_z\sin\theta & u_y^2+(1-u_y^2)\cos\theta & u_yu_z(1-\cos\theta)-u_x\sin\theta \\ u_xu_z(1-\cos\theta)-u_y\sin\theta & u_yu_z(1-\cos\theta)+u_x\sin\theta & u_z^2+(1-u_z^2)\cos\theta \end{pmatrix}\mathbf{r}. \quad (3.4)$$

The coordinate systems and transformations are supplied as input to the program, so this may be used for different experimental setups.

For example, the transformations applied to detector E1 are

$$\begin{aligned} \mathrm{R}_1 &= \mathrm{R}\big(\langle 1,0,0\rangle, 90^\circ\big), \\ \mathrm{T}_2 &= \mathrm{T}\big(\langle 0, 8.6, -80.2\rangle\,\mathrm{mm}\big), \\ \mathrm{R}_3 &= \mathrm{R}\big(\langle 0,0,1\rangle, 6.0^\circ\big), \\ \mathrm{T}_4 &= \mathrm{T}\big(\langle 0, 95.3, 0\rangle\,\mathrm{mm}\big), \text{ and} \\ \mathrm{R}_5 &= \mathrm{R}\big(\langle 0,0,1\rangle, 330.0^\circ\big). \end{aligned}$$

When these are all applied, the position of the detector is

$$\begin{aligned} \mathbf{r}(u,v) &= \mathrm{R}_5\mathrm{T}_4\mathrm{R}_3\mathrm{T}_2\mathrm{R}_1\langle u,v,0\rangle \\ &= \langle 51.1 + 0.914v, 90.4 - 0.406v, -80.2 + u\rangle\,\mathrm{mm}. \end{aligned} \quad (3.5)$$

Listing 3.1 is a configuration for this setup.

Listing 3.1: An example configuration for Detector E1

```
{
  "templates": {
    "BB15": {
      "coords": "CartesianZ",
      "u_limits": [0.0, 75.0],
      "v_limits": [-20.0, 20.0]
    },
    "SORR_UP": {
      "template": "BB15",
      "transformations": [
        {"Rotation": [0, -90, 0]},
        {"Rotation": [0, 0, 90]},
        {"Translation": [0, 8.636, -80.2386]},
        {"Rotation": [0, 0, 6.03]},
        {"Translation": [0, 95.25, 0]}
      ]
    }
  },
  "detectors": [
    {
      "template": "SORR_UP",
      "transformations": [
        {"Rotation": [0, 0, -30]}
      ]
    }
  ]
}
```

The solid angle can be found using the surface area, $\mathbf{S}$, using

$$\mathrm{d}\mathbf{S} = \frac{\partial \mathbf{r}}{\partial u} \times \frac{\partial \mathbf{r}}{\partial v}\,\mathrm{d}u\,\mathrm{d}v \text{ and} \tag{3.6}$$

$$\mathrm{d}\Omega = \frac{\mathbf{r}\cdot\mathrm{d}\mathbf{S}}{|r|^3}. \tag{3.7}$$

Using this coordinate system, arbitrary functions can be minimized with respect to $u$

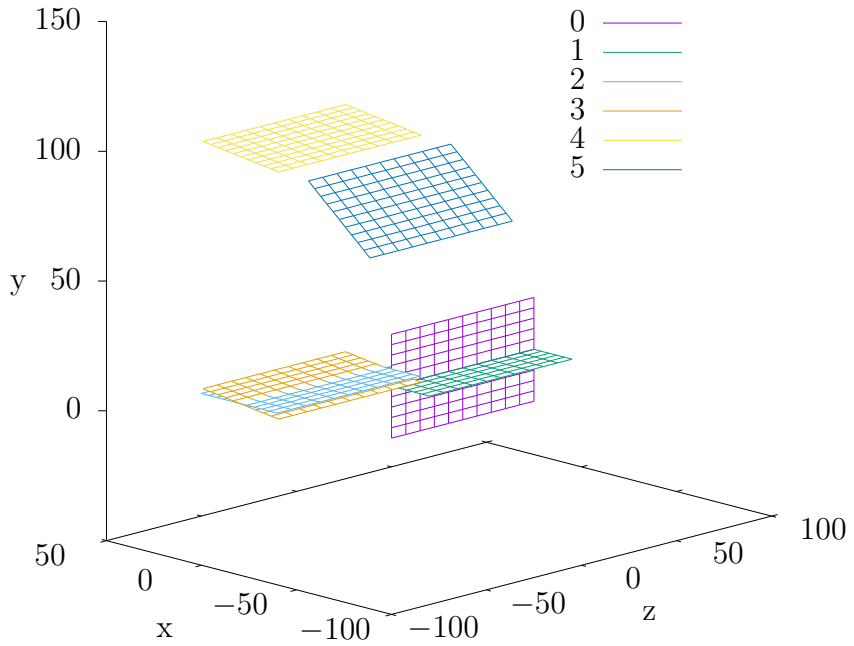


Figure 3.2: The location of detector E1 with an increasing number of transformations applied until the detector is at the experimental location. The reaction location is at $\langle 0, 0, 0 \rangle$.

and $v$. The average value can also be found using

$$f_{\text{avg}} = \frac{\iint f \, \mathrm{d}\Omega}{\iint \mathrm{d}\Omega}, \tag{3.8}$$

where $\Omega$ is the solid angle and $f$ is the function of interest. The spherical coordinates, which are defined as

$$r(u,v) = \sqrt{x(u,v)^2 + y(u,v)^2 + z(u,v)^2}, \tag{3.9}$$

$$\theta(u,v) = \arccos\left(\frac{z(u,v)}{r(u,v)}\right), \text{ and} \tag{3.10}$$

$$\phi(u,v) = \arctan\left(\frac{y(u,v)}{x(u,v)}\right), \tag{3.11}$$

are examples of functions that were averaged using Equation (3.8).

Shadows can be applied to a detector. Shadows are surfaces that block the path from the

origin to the detector. This allows for any obstruction to be described as above, independent of the coordinate system of the detector itself. For this analysis, shadows that correspond to the nozzle and receiver were applied to the detectors above and below the target because they partially block those detectors.

The positions and solid angles calculated in this way were used to efficiency calculations detailed in Section 3.6. The total solid angle covered by the silicon detector array is $(3.8 \pm 0.5)\,\mathrm{sr}$.

The input into the calculation of the detector positions are not perfect and have some measurement uncertainty associated with them, which leads to an uncertainty in the values calculated. To account for this, a Monte Carlo method is used. The input values are randomly varied according to a Gaussian distribution described by their mean and standard deviation. The mean and standard deviation of the results are then calculated from 10 000 runs. Figure 3.3 shows the results from such a calculation. The input values come from a combination of technical drawings, alignment tools, and hand measurement. The source of uncertainty is dominated by the hand measurements. For SORR_UP and SORR_DN, the translation uncertainties are 1 mm. For SIDAR, the distance to the target was inconsistently recorded; to account for this, the translation uncertainties for the final translation were 20 mm along the beam axis and 3 mm perpendicular to the beam axis.

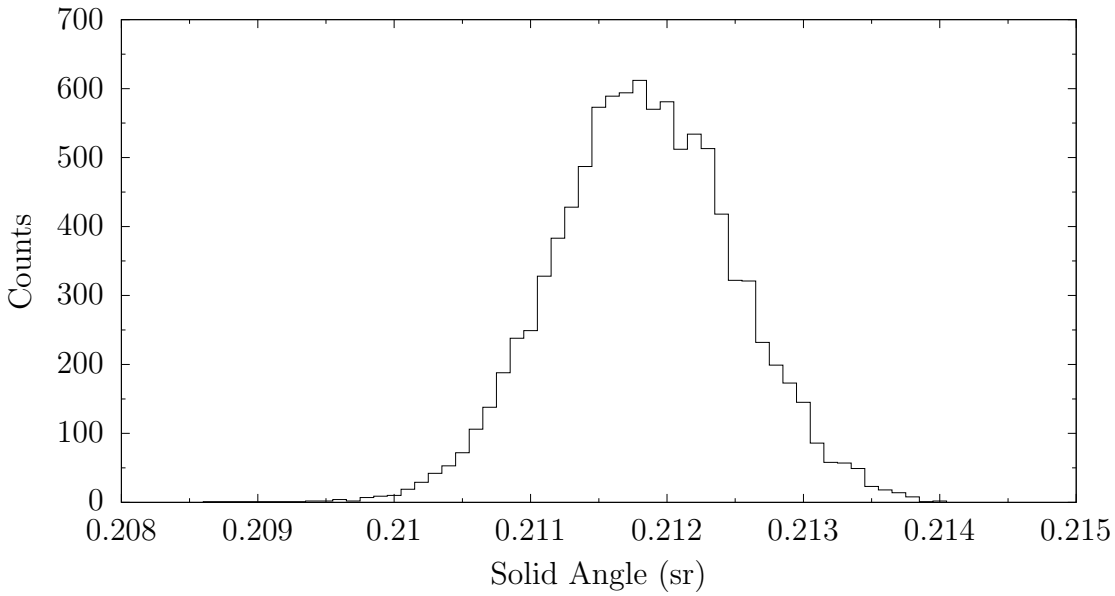


Figure 3.3: An example of Monte Carlo results of the solid angle for detector E1.

## 3.3 Energy Calibrations

Both the ionization chamber and the silicon detectors measure the amount of energy deposited by a particle traveling through them. The particle causes ionization in the detector material. The resulting charge is collected and converted to a voltage change, which is then processed by the electronics and stored as a digitized channel in the data acquisition system. The signal height is linearly related to the energy deposited in the detector, so the energy calibration function is

$$E = aCh + b, \tag{3.12}$$

where $E$ is the energy deposited in the detector and $Ch$ is the digitized signal value, referred to as the "channel".

### 3.3.1 Silicon Detectors

The energy calibration was done in two steps. First, the channel which corresponds to zero energy was found. Second, the channel which corresponds to a known energy was found. Using these two points, a linear relationship between channel and energy was determined.

The zero-energy channel is the same as the zero-voltage channel, which can be found using two different pulser signals with known voltage ratios, regardless of the absolute voltage input into each channel. This is important because the pulser signal is split among all channels sharing the same hardware input (possibly not equally), so the exact voltage is not known. However, as long as the ratio between the different pulser signals is known, the zero-voltage channel can be found.

$$\begin{aligned}
\frac{Ch(V_2) - Ch(V{=}0)}{Ch(V_1) - Ch(V{=}0)} &= \frac{AV_2}{AV_1} \\
Ch(V_2) - Ch(V{=}0) &= \frac{V_2}{V_1}\left(Ch(V_1) - Ch(V{=}0)\right) \\
\left(\frac{V_2}{V_1} - 1\right) Ch(V{=}0) &= \frac{V_2}{V_1}\, Ch(V_1) - Ch(V_2) \\
Ch(V{=}0) &= \frac{R\, Ch(V_1) - Ch(V_2)}{R - 1}
\end{aligned} \tag{3.13}$$

After the zero-energy channel is found, the slope of the calibration can be found using the detection of a particle with a known energy from a radioactive source. In this experiment, the 5.486 MeV peak from the $\alpha$-decay of an $^{241}$Am source was used.

$$
\begin{aligned}
E_{^{241}\mathrm{Am}} &= s(Ch_{^{241}\mathrm{Am}} - Ch_0) \\
s &= \frac{E_{^{241}\mathrm{Am}}}{Ch_{^{241}\mathrm{Am}} - Ch_0}
\end{aligned}
\tag{3.14}
$$

There are some channels that could not be calibrated using this method because some or all of the peaks necessary for calibration were missing. This included all BB10 channels because there were no pulser data. Figure 3.4 shows some examples of channels that could not be calibrated. These were not used in the analysis.

### 3.3.2 Ionization Chamber

The ionization chamber detects beam particles and reaction recoils, both of which have a much higher energy than the particles emitted from a radioactive source. Because of this, the ionization chamber could not be calibrated using a radioactive source. Instead, the beam and recoils were used.

Uncertainty and spread in the energy detected in each section of the ionization chamber is introduced for each material through which the beam travels before reaching that section. These sections are shown in Table 3.2. The materials in which energy is lost before the first detecting section of the ionization chamber are the He target, the Mylar window, and the non-detecting dead layer of isobutane in the ionization before the first grid. Because of this, it is ideal to calibrate the ionization chamber using runs that did not have the beam traveling through the target. This, however, was possible only for the dE and E sections and the central wires of the X and Y sections. The outer wires of the X and Y sections

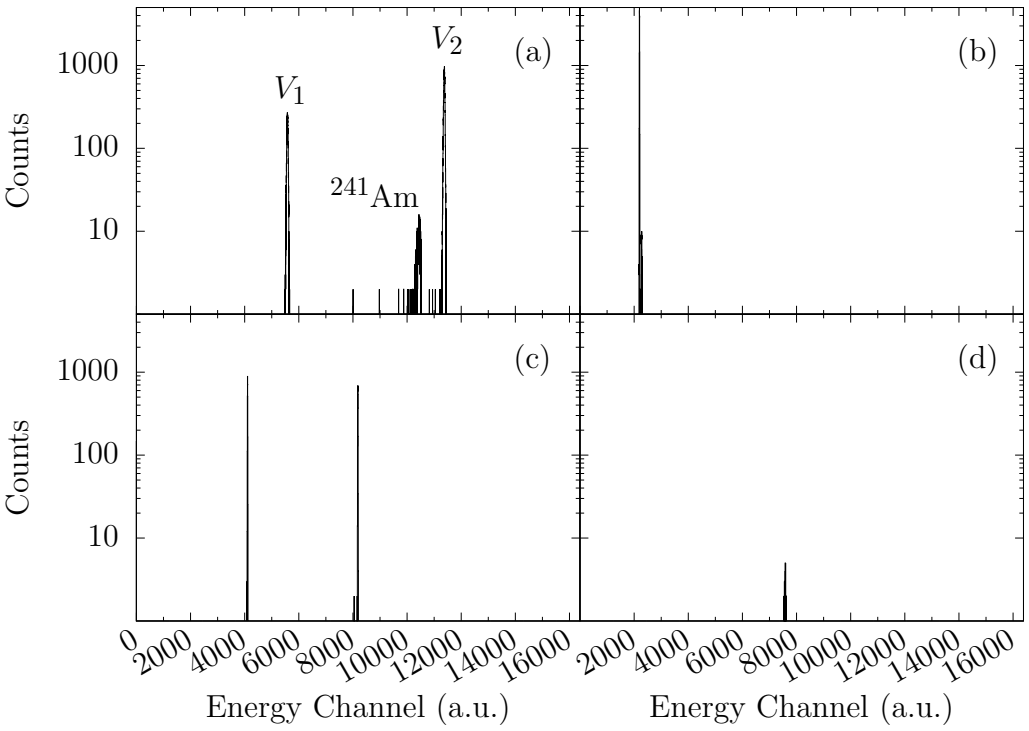


Figure 3.4: Spectra from silicon detector calibrations. (a) shows a normal channel with a $^{241}$Am peak and two pulser peaks. (b) shows a channel with only one pulser peak. (c) shows a channel with no $^{241}$Am. (d) shows a channel with no pulser peaks.

Table 3.2: The layers through which the beam passes and loses energy.

| Section | Material | Thickness |
|---|---|---|
| target | He | (5–8) $\times 10^{18}$ atoms/cm$^2$ |
| window | Mylar | 3 µm |
| dead layer | isobutane | 2 cm |
| X | isobutane | 3.66 cm |
| Y | isobutane | 3.66 cm |
| dE | isobutane | 7.32 cm |
| E | isobutane | 18.30 cm |

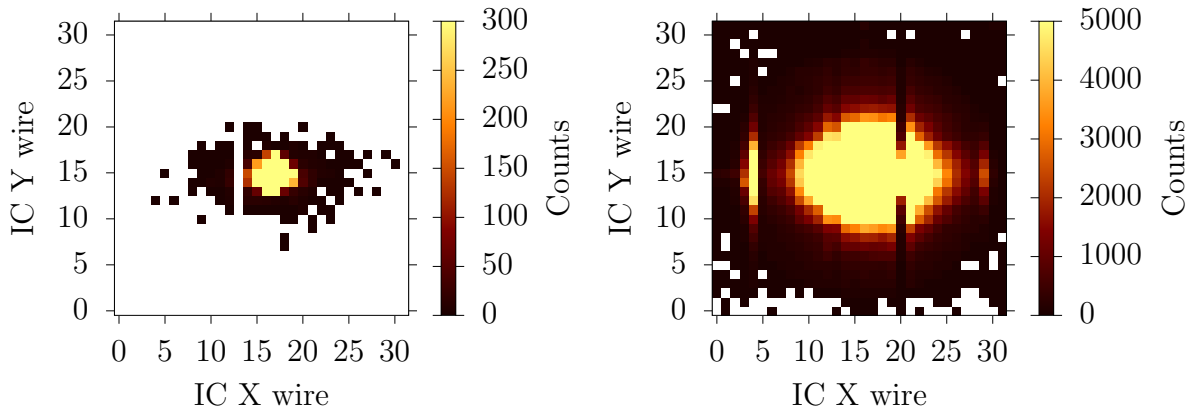


(a) Without jet

(b) With jet

Figure 3.5: The hit pattern in the ionization chamber (a) without and (b) with the jet present.

could not be calibrated using these runs because there was no jet where the beam particles could scatter off to reach these channels. Instead, these channels were calibrated using the scattered beam from the experimental runs. Figure 3.5 shows the difference in number of events in each pixel of the ionization chamber for the runs with and without the jet.

The energy to be used in the calibration was calculated using the energy loss code ATIMA [59]. The energy loss in each section was calculated by integrating along the path of the projectile. These energy losses depend on the density of the target and the pressure inside the ionization chamber, which varied throughout the experiment, as is shown in Figure 3.6.

These changes were tracked using the pressure gauges $CAP_{in}$ and $CAP_{ic}$, which were recorded by EPICS (see Section 2.4), with a sampling frequency of 0.2 Hz.

The pressure inside the ionization chamber was measured by a capacitance gauge $CAP_{ic}$. There were some gaps in the measurements because an EPICS system restart caused the gauge to stop being read. This limits the number of runs that could be used for calibration.

The areal density was determined using the pressure of the gas immediately before the nozzle (see Section 2.2.1). During the experiment, this was measured in $CAP_{in*}$. The method used to determine the relationship between $CAP_{in}$ and the areal density of the jet is detailed in Section 3.6.

The channels used in the the calibration are the centroids of fits of the peaks in the energy spectra of the corresponding sections. However, the different beam species ($^{34}$S, $^{34}$Cl, and $^{34}$Ar) are hard to distinguish in the one-dimension energy spectra of the X, Y, and dE sections. In the E section, the beam species are easy to distinguish, so this is used to create two-dimension spectra with the E section, and gate on the peaks to create a one-dimension spectrum for each species. Figure 3.7 shows the resulting fits.

Figure 3.8 shows the results of this process. The $^{34}$Ar and $^{34}$Cl points fit on a line. However, the $^{34}$S peaks systematically deviate; these peaks were consistently fit at a lower channel than expected. In Figure 3.7, it can be seen that there is overlap between the $^{34}$Cl and $^{34}$S peaks, and since there are many more counts in the $^{34}$Cl peak, the tail of that peak can significantly affect the shape of the $^{34}$S peak. Because of this, the $^{34}$S peaks were not used for calibration.

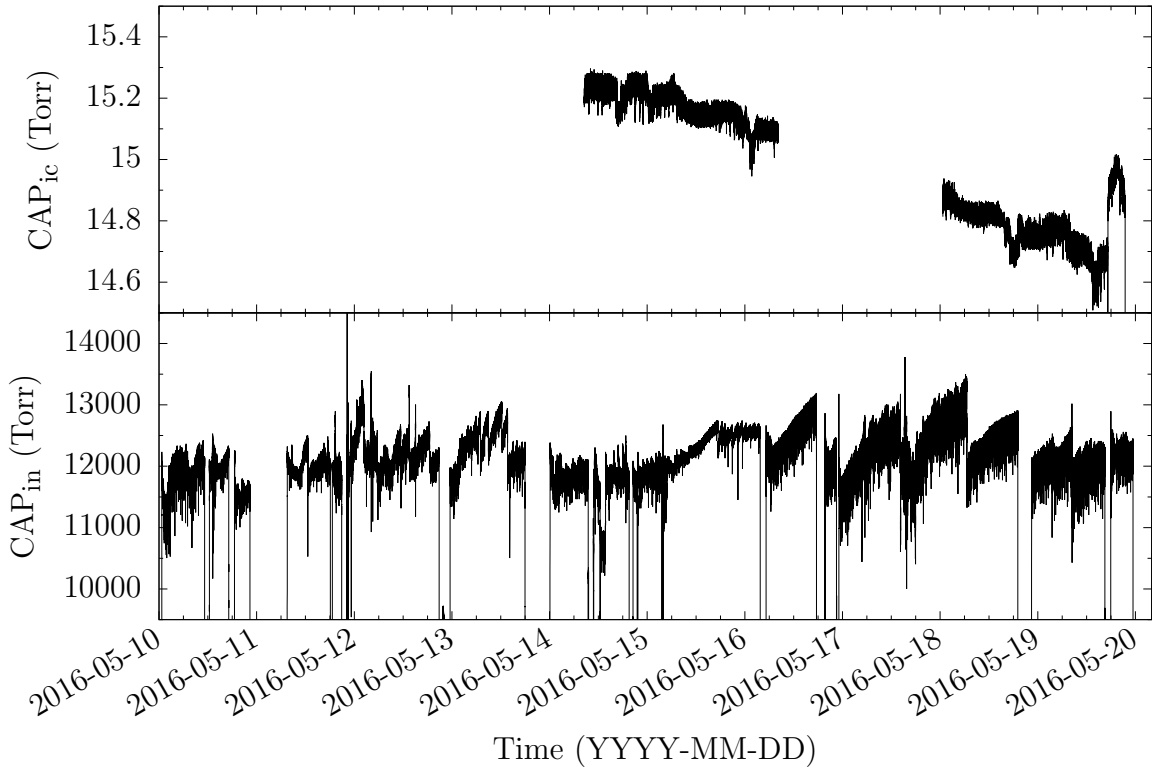


Figure 3.6: The time series data for the pressures measured by $\mathrm{CAP_{ic}}$ and $\mathrm{CAP_{in}}$. $\mathrm{CAP_{ic}}$ measured the pressure in the ionization chamber; for parts of the experiment, it was not recorded by the EPICS system. $\mathrm{CAP_{in}}$ measured the pressure immediately before entering the nozzle; this was used to determine the areal density of the jet.

Table 3.3: The ionization chamber energy calibration values.

| Section | Channel (0-based) | Slope | Intercept |
|---|---|---|---|
| X | 16 | 2.903 | $2126 \pm 19$ |
| | 17 | 2.903 | $1892 \pm 11$ |
| | 0–15, 18–31 | 2.903 | $1951 \pm 195$ |
| Y | 15 | 3.411 | $1482 \pm 25$ |
| | 16 | 3.411 | $1485 \pm 34$ |
| | 0–14, 17–31 | 3.411 | $1483 \pm 37$ |
| dE | 0 | 9.984 | $-530 \pm 73$ |
| E | 0 | 6.358 | $11\,264 \pm 88$ |

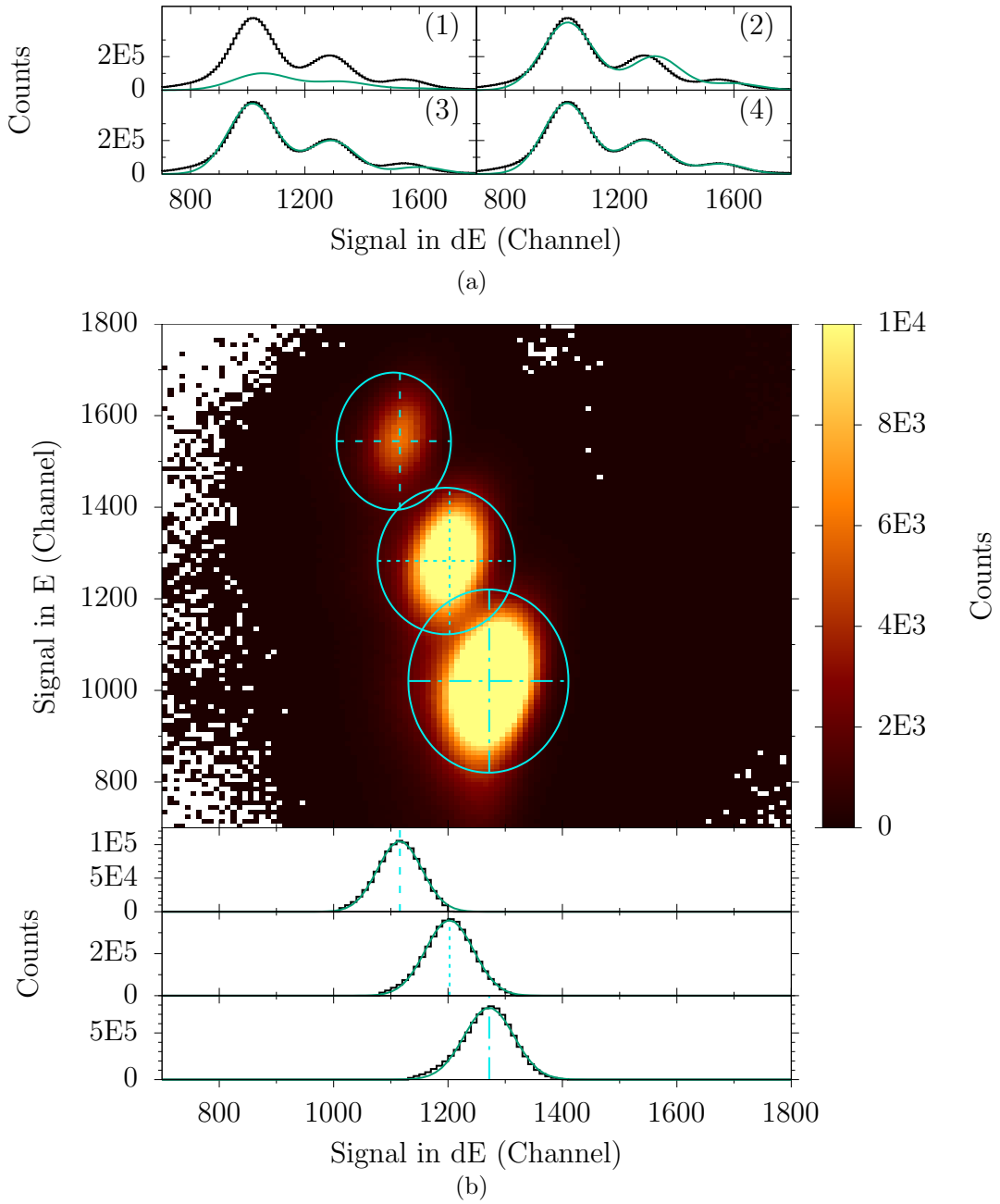


Figure 3.7: The peaks in the ionization chamber were fit in multiple steps. First, the E section is fit, as shown in (a) because it is the channel in which the peaks are most easily distinguished. The peaks are not as well separated in the remaining channels, so the information from the E channel is used. (b) shows the elliptic gates around the peaks in the E vs. dE spectrum and how the separate peaks in the dE channel are fit after using these gates.

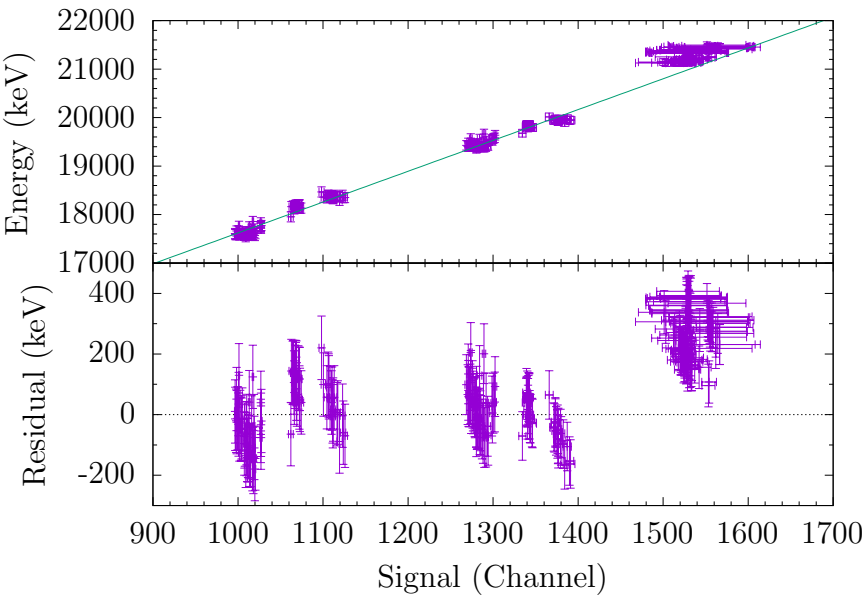


Figure 3.8: The calibration curve for the E section of the ionization chamber. The lowest energy group corresponds to $^{34}$Ar, the middle $^{34}$Cl, and the highest $^{34}$S. The $^{34}$S points do not agree with the the $^{34}$Ar and $^{34}$Cl points. This is likely due to interference from the larger $^{34}$Cl peak.

## 3.4 Timing

The silicon detectors and the ionization chamber register hits from the same reaction at a fixed time difference that is determined by the flight times of the particles from the reaction point as well as electronics delays. In order to separate random coincidences from actual coincidences, we can gate on the time difference between the two systems.

The time difference between hits in the two systems contains many peaks, as shown in the "Ungated" plot in Figure 3.9. To determine where to gate for true coincidences, we need to identify hits that we know originate from the same reaction. We used the elastic scattering events by gating on the alpha particles detected in the silicon detectors near 90° in the lab frame. Figure 3.10 shows the relation between the energy detected and polar angle in detectors E9 and E13. These are the detectors without a thin detector layer in front of the thick detector. In these detectors, $\alpha$-particles from elastic scattering can be seen. Gating

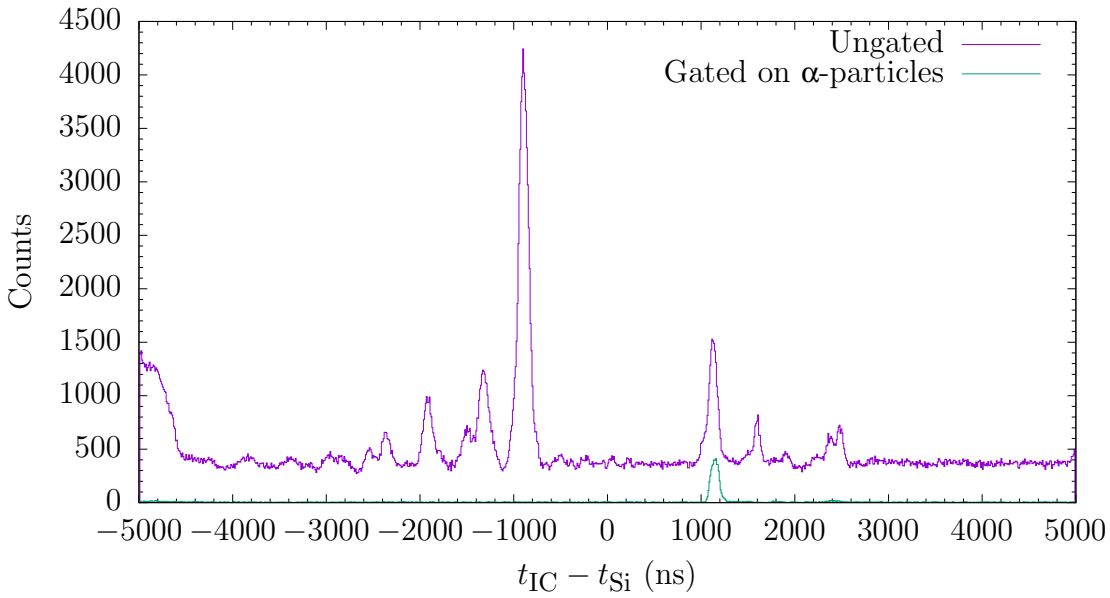


Figure 3.9: The time difference between hits in the ionization chamber and the silicon detectors. "Ungated" shows this for all hits. "Gated on α-particles" shows this only for hits in E9 and E13 inside the α-partcle gate shown in Figure 3.10.

on this region gives a single peak in time difference, as shown in the "Gated on α-particles" plot in Figure 3.9.

Fitting a Gaussian curve to this peak, we get the following fit:

$$f(x) = a \exp\left(-\frac{(x-b)^2}{2c^2}\right) + d, \tag{3.15}$$

with parameters $a = 414 \pm 5$, $b = 1147 \pm 1$, $c = 43 \pm 1$, and $d = 5 \pm 1$. Using a $3\sigma$ (99.7 %) confidence interval to make a gate, we set the gate at (1016–1278) ns.

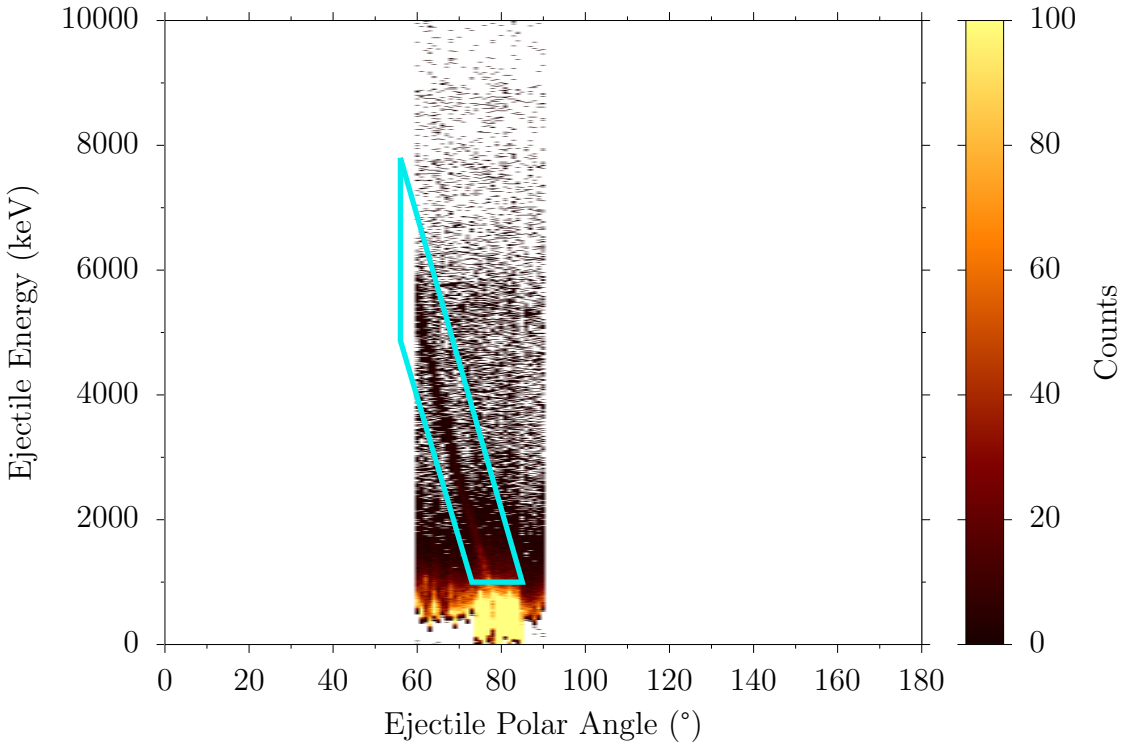


Figure 3.10: The energy-polar angle relationship in E9 and E13, the detectors without a thin detector in front of the thick detectors. These detectors can clearly see the α-particles from elastic scattering. A gate is drawn around these hits and used as the gate in Figure 3.9.

## 3.5 Particle Identification

During this experiment, there were a variety of reactions that occurred. There were three beam species, and for each of those species, there were two reactions, (α,α) and (α,p). In order to distinguish between all of these reactions, we must know which particles are being detected. There are two properties that are used to determine the species of a detected particle: kinematics and energy loss.

Figure 3.11 shows a kinematics diagram of these reactions. There are a few degrees of freedom: the polar and azimuthal angles in the center of mass frame ($\theta^{\mathrm{CM}}$ and $\phi^{\mathrm{CM}}$, respectively) and the excitation energy of the outgoing recoil ($E_{\mathrm{ex}}$). $\theta^{\mathrm{CM}}$ and $E_{\mathrm{ex}}$ affect $\theta_{\mathrm{r}}^{\mathrm{lab}}$, $\theta_{\mathrm{e}}^{\mathrm{lab}}$, $E_{\mathrm{r}}^{\mathrm{lab}}$, and $E_{\mathrm{e}}^{\mathrm{lab}}$. $\phi^{\mathrm{CM}}$ affects $\phi_{\mathrm{r}}^{\mathrm{lab}}$ and $\phi_{\mathrm{e}}^{\mathrm{lab}}$. The relationship between $\theta^{\mathrm{lab}}$ and $E^{\mathrm{lab}}$ for each particle can be plotted as a series of lines, as in Figure 2.8. Each line corresponds to a different $E_{\mathrm{ex}}$, and along each of those lines, $\theta^{\mathrm{CM}}$ varies.

The first step of particle identification involves distinguishing particles based on $\theta^{\mathrm{lab}}$ and $E^{\mathrm{lab}}$. The recoils are only emitted with $\theta^{\mathrm{lab}} < 10^{\circ}$ and $E^{\mathrm{lab}} > 30\,\mathrm{MeV}$. This means that recoils are detected only in the ionization chamber, and because the energy of the ejectiles is too low to be detected in the ionization chamber, we know that the ionization chamber only detects recoils and unreacted beam. Because α-particles are limited to $\theta^{\mathrm{lab}} < 90^{\circ}$, we know that any particles detected in SORR_UP should be protons. And in SORR_DN and SIDAR, protons and α-particles can be distinguished using energy loss, as described below.

In addition, background events may be detected in all detectors by reactions in gas outside of the jet, beam scattered off of apertures, gas impurities, multiply scattered particles, electronic noise, etc. However, the cleanness of the spectra after applying the coincidence gates (shown in Figure 3.13) suggests that this is minimal.

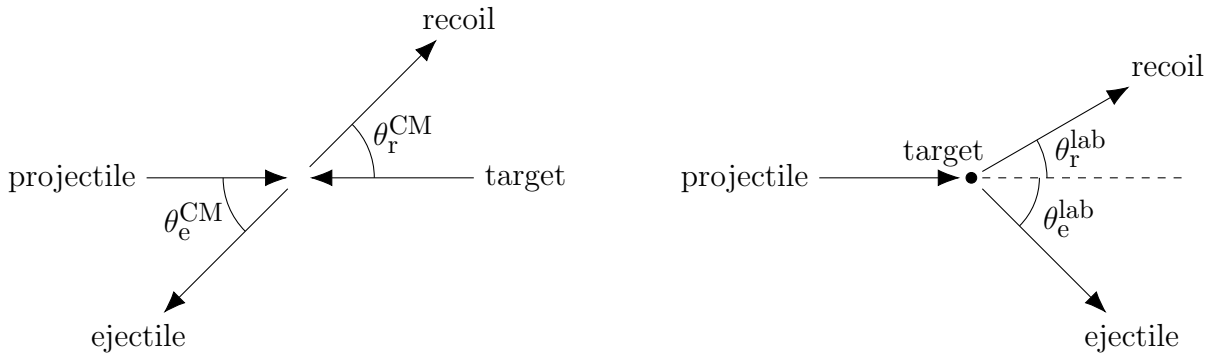


(a) Center of Mass Frame

(b) Lab Frame

Figure 3.11: Diagram showing the incoming and outgoing particles in the reactions of this experiment in the (a) center of mass reference frame and the (b) lab reference frame.

Two different particles that travel through the same material will lose energy at different rates. This property, the stopping power, depends on the energy of the particle. Therefore, this is measured with multiple stages of detection: one which measures the energy loss and another which measures all residual energy. In the silicon detectors, this involves a thin detector and a thick detector in a "telescope" configuration. In the ionization chamber, this involves splitting the detector into multiple sections, which are read out separately.

### 3.5.1 Ejectiles

The ionization chamber detects a high rate of unreacted beam, which partially overlaps with the recoils. In order to exclude random coincidences of silicon detector hits with unreacted beam, we negatively gate on the central angles of the ionization chamber ($< 0.6°$). This excludes only events which wouldn't be detected anyway because of the following reasons: 1) the ejectile angle is too low or 2) the ejectile energy is low.

The single detectors in SORR_UP detect protons at low energies. To distinguish protons from electronic noise, a gate was made to reject signals with $E < 500\,\mathrm{keV}$.

The silicon detector telescopes consist of two detector layers: a 60 µm thick detector in

front of a 1 mm thick detector. These are called the dE and E layers, respectively. Figure 3.12 shows the relationship between the energy loss in the dE layer. Figure 3.12b is gated on the timing gate described in Section 3.4, and Figure 3.12a is not. There are many more α-particles that are not detected in coincidence with an ionization chamber hit. This is because many of the scattered recoils are emitted at an angle larger than that covered by the ionization chamber. This can be seen in Figure 2.8. This is only the case for the (α,α) recoils; the (α,p) recoils are all emitted at angles less than the acceptance angle of the ionization chamber.

The actual thicknesses of the detectors are not exactly the nominal thickness; they deviate from this nominal value by up to 23 %. This affects the energy deposited in that detector. In order to merge events from different detectors, the energy losses were normalized to a dE detector thickness of 60 µm. The correction assumes energy loss is proportional to thickness, resulting in normalized energy loss values of

$$\begin{aligned} dE_{60} &= \frac{60\,\mu\text{m}}{t}\,dE \\ E_{60} &= E + (dE - dE_{60}), \end{aligned} \tag{3.16}$$

where $t$ is the actual thickness of the dE detector, $dE$ and $E$ are the energies detected in the dE and E detectors, respectively, and $dE_{60}$ and $E_{60}$ are the normalized energies.

The range of a 9 MeV α-particle in silicon is 60 µm, which means that α-particles with an energy below 9 MeV are stopped in the dE detectors and are not detected in the E detectors. The energy of scattered α-particles decreases as the scattering angle approaches 90°. The 9 MeV threshold is crossed in the SORR_DN section, and there are two parts of this section: SORR_DNT comprises four telescopes, and SORR_DNS comprises two single detectors with no

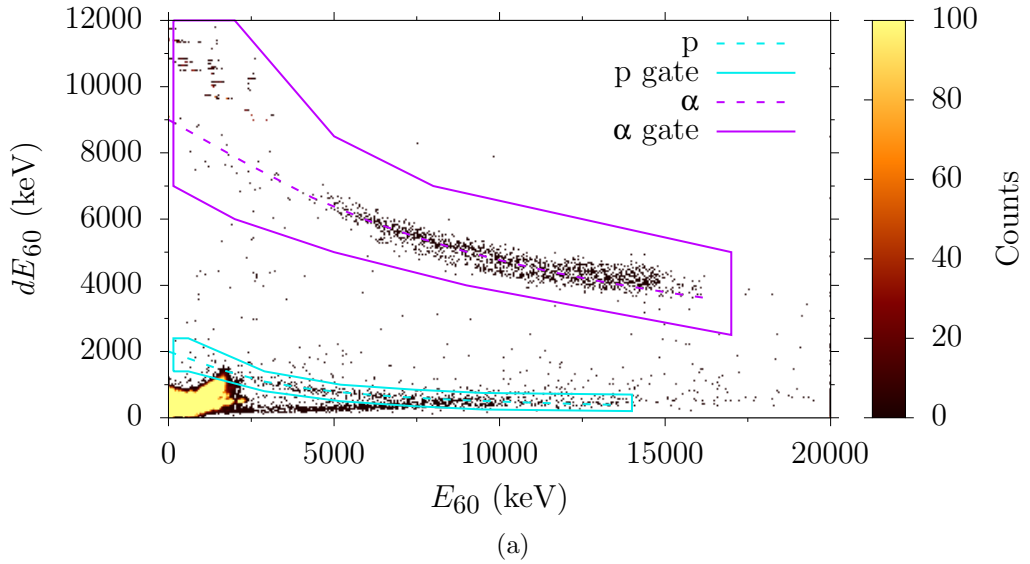


(a)

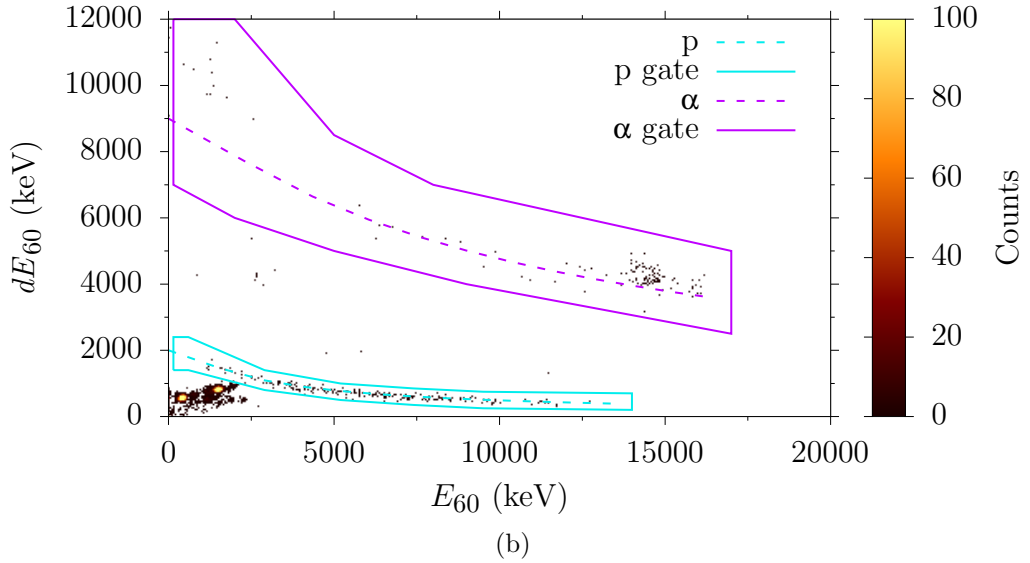


(b)

Figure 3.12: The energy loss in the dE layer vs the energy loss in the E layer of the silicon detector telescopes, corrected for the difference in detector thicknesses. (a) shows this plot without gating on the timing difference described in Section 3.4, and (b) shows the plot gated on this timing. The separate groups for α-particles and protons can be seen. The regions used for gating are shown. The intermediate-energy α-particles are excluded in (b) because the recoils are not detected in the ionization chamber (see Figure 2.8).

Table 3.4: The thickness of the dE detectors.

| Detector | Thickness (µm) |
|---|---|
| dE8 | 63 |
| dE10 | 65 |
| dE11 | 60 |
| dE14 | 63 |
| dE15 | 60 |
| dE16 | 67 |
| dE17 | 67 |
| dE18 | 74 |
| dE19 | 59 |

dE layers. SORR_DNS detects α-particles throughout the whole angular range, but is not capable of particle identification based on energy loss. SORR_DNT detects α-particles in only the most downstream strips.

Ejectiles are thus identified as hits in the silicon detectors; with an energy greater than 500 keV; within the timing gate of a hit in the outer wires of the ionization chamber; and if the hit occurred in SORR_DNT or SIDAR, have $dE_{60}$ and $E_{60}$ within the proton or α-particle gates. Figure 3.13 shows the effect of these gates.

### 3.5.2 Recoils

There are three categories of particles detected in the ionization chamber: unreacted beam, (α,α) recoils, and (α,p) recoils. For each category, there are three species. The unreacted beam and (α,α) recoils are $^{34}$S, $^{34}$Cl, and $^{34}$Ar. The three (α,p) recoils are $^{37}$Cl, $^{37}$Ar, and $^{37}$K.

The unreacted beam is limited to a polar angle of $< 0.6^{\circ}$, so anything with a larger angle is known to be a recoil. The other two can be distinguished by using the information on the ejectile as described in Section 3.5.1.

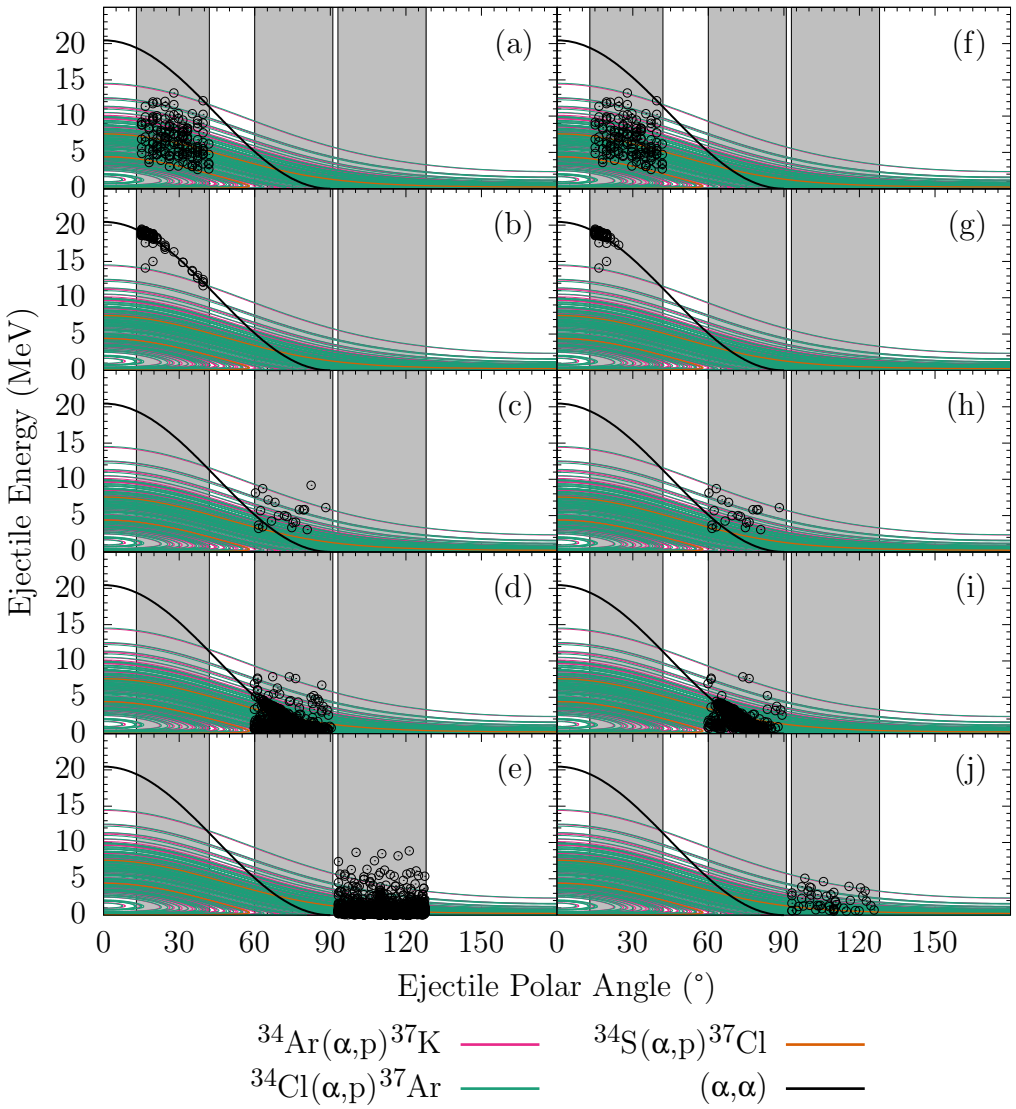


Figure 3.13: The relationship between the energy and the polar angle of the ejectiles for the experimental energy E2. The gates on the recoil polar angle and the ejectile energy are able to separate events caused by the reactions of interest from those caused by random coincidences. (a) and (f) show the events in SIDAR, with an ejectile identified as a proton. (b) and (g) show the events in SIDAR, with an ejectile identified as an α-particle. (c) and (h) show the events in SORR_DNT, with an ejectile identified as a proton. (d) and (i) show the events in SORR_DNS (these events are not used to calculate the cross section). (e) and (j) show the events in SORR_UP. (a)–(e) show events gated only by the timing gate. (f)–(j) show events gated by the timing gate, the $E_{\mathrm{e}}^{\mathrm{lab}} > 500\,\mathrm{keV}$ gate, and the $\theta_{\mathrm{r}}^{\mathrm{lab}} < 0.6°$ gate. The cleanness of these spectra suggest that the number of background events is negligible. The two points below the (α,α) line in (b) and (g) are where α-particles that are only detected in the dE detector would be expected to be seen.

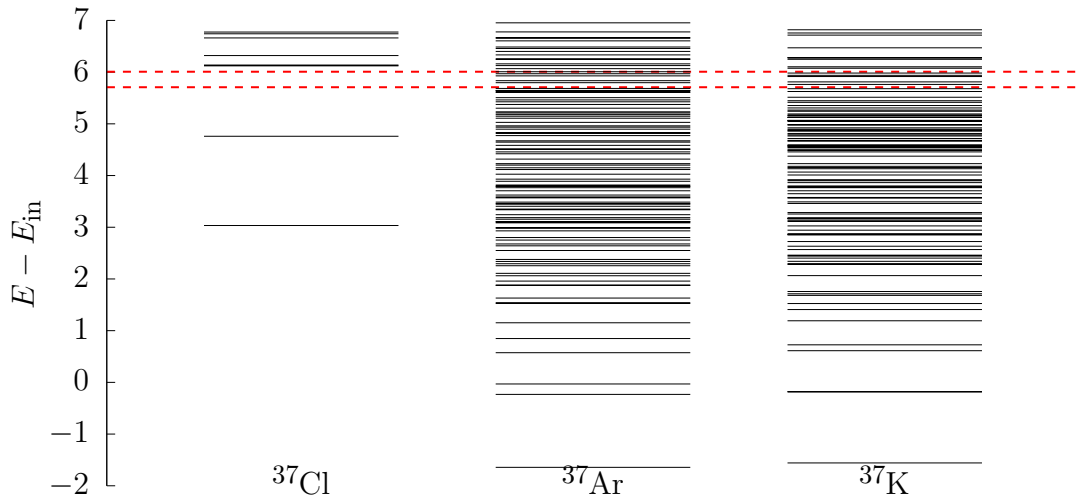


Figure 3.14: The levels in the recoil nuclei $^{37}$Cl, $^{37}$Ar, and $^{37}$K [61], with $E - E_{\text{in}} = 0$ being the energy of the beam and target system, excluding the kinetic energy [62]. The dotted red lines show the energy of the system with the kinetic energies of this experiment.

There are two degrees of freedom in these reactions—center of mass polar angle and excitation energy. They can be determined using the ejectile information. With that information, the energy and angle of the recoil can be predicted. We can then compare these predictions to our measurements and determine which particle identification is most likely. To do this, the probability that an event is an occurrence of $X$ reaction is

$$P_X = \frac{W_X}{\sum_X W_X} \tag{3.17}$$

$$W_X = \left( \frac{\sum_S \left( E_S - E_{S,X}(\theta_{\text{CM}}, E_{\text{ex}}) \right)^2}{\sigma_{\text{sys}}^2 + \sigma_{\text{stat}}^2} \right)^{-1} \tag{3.18}$$

where $W_X$ is the weight for $X$, $S$ is a section of the ionization chamber, $E_S$ is the experimentally measured energy deposited in $S$, and $E_{S,X}(\theta_{\text{CM}}, E_{\text{ex}})$ is the energy predicted to be deposited in $S$ if $X$ occurred with a center of mass polar angle of $\theta_{\text{CM}}$ and a recoil excitation energy of $E_{\text{ex}}$.

The different species are most separated in the section of the ionization chamber where

they are stopped—the E section. The settings for the ionization chamber electronics were optimized using the unreacted beam; however, the recoils have less energy than the unreacted beam. Because of this, the energy detection threshold for the E section was about 11 MeV (see Section 3.3.2), but the recoils deposit less energy than that threshold in the E section. This means the data most useful for determining the identity of the recoils is not available.

If the energy resolution of the other sections were sufficient, it would be possible to determine the the identity of the recoils using the energy deposited in the X, Y, and dE sections. However, that is not the case; instead, this work will report a combined cross section of the $^{34}$Cl($\alpha$,p)$^{37}$Ar, and $^{34}$Ar($\alpha$,p)$^{37}$K reactions (see Section 3.6).

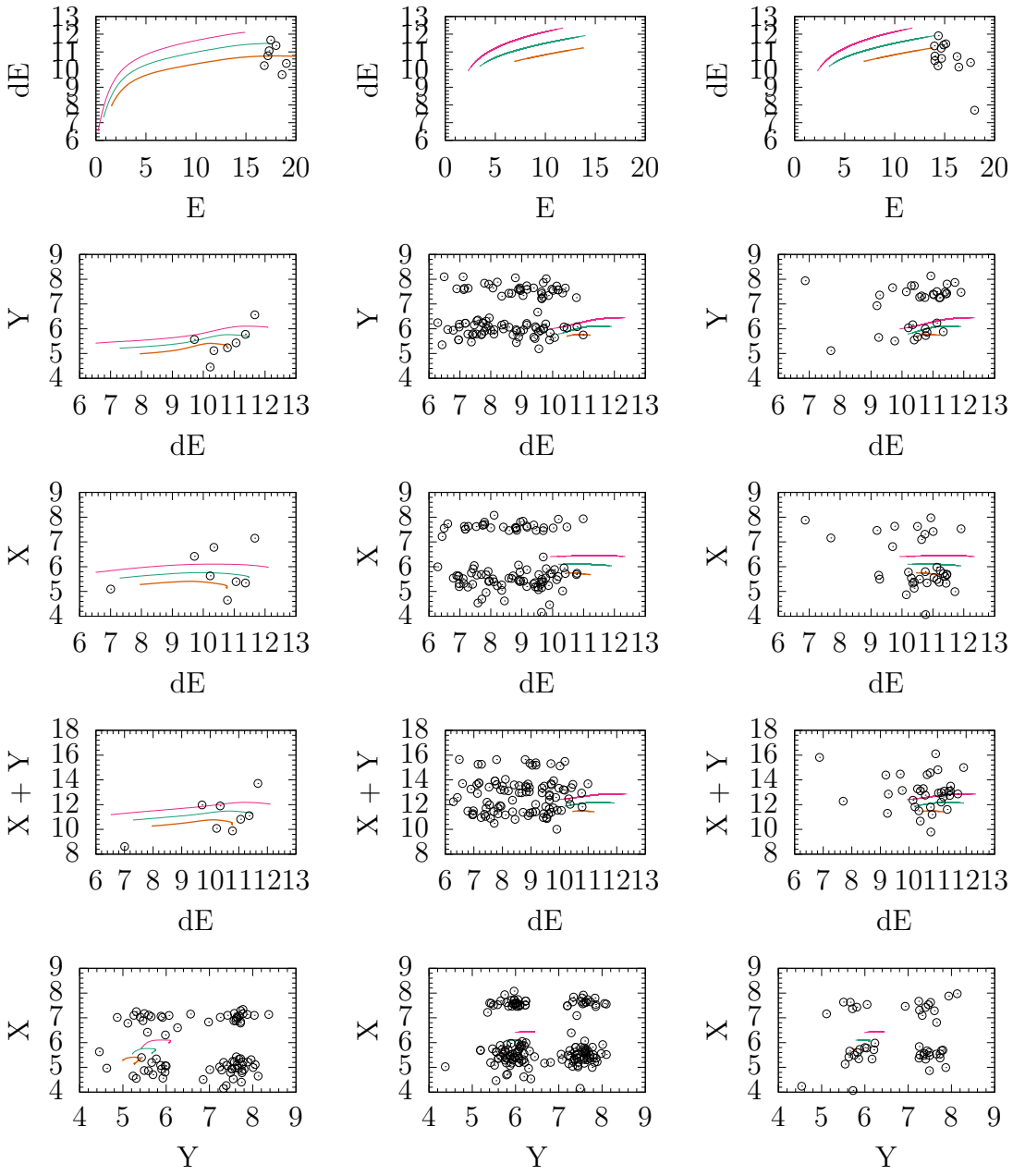


Figure 3.15: The energy deposited in the various sections of the ionization chamber by the recoils. The lines show the energies at which the recoils are expected to be detected. This shows that the recoils cannot be distinguished based on this.

## 3.6 Cross Section

The number of reactions detected is related to the differential cross section, $\frac{\mathrm{d}\sigma}{\mathrm{d}\Omega}$, through

$$N = \iint \varepsilon(\Omega) f_{\mathrm{live}} I(t) \rho_A(t) \frac{\mathrm{d}\sigma}{\mathrm{d}\Omega} \,\mathrm{d}t \,\mathrm{d}\Omega \,, \tag{3.19}$$

where $I(t)$ is the beam intensity, $\rho_A(t)$ is the areal number density, $t$ is time, $\varepsilon(\Omega)$ is the detection efficiency, $f_{\mathrm{live}}$ is the live time fraction, and $\Omega$ is the solid angle. An overall detection efficiency, $\varepsilon$, is introduced, such that

$$\int \varepsilon(\Omega) \frac{\mathrm{d}\sigma}{\mathrm{d}\Omega} \,\mathrm{d}\Omega = \varepsilon\sigma. \tag{3.20}$$

Using Equations (3.19) and (3.20), an equation for the cross section can be found:

$$\sigma = \frac{N}{\varepsilon \int f_{\mathrm{live}} I(t) \rho_A(t) \,\mathrm{d}t}. \tag{3.21}$$

To determine the cross section, we need the number of reactions ($N$), efficiency ($\varepsilon$), beam intensity ($I$), target areal density ($\rho_A$), and live time fraction ($f_{\mathrm{live}}$). $I$, $\rho_A$, and $f_{\mathrm{live}}$ vary from run to run, while $\varepsilon$ does not.

$N$ is measured simply by counting up the number of events that satisfy the criteria in Section 3.5. Specifically, that means:

- the event must contain an ejectile hit in the silicon detectors that either:
  - occurs in a telescope pair of detectors and have $dE_{60}$ and $E_{60}$ signals that fall within the proton gate described in Section 3.5.1 or
  - occurs in SORR_UP and has an energy of $> 500\,\mathrm{keV}$

- the event must contain a recoil hit in the ionization chamber that has a polar angle of $> 0.6^\circ$, and
- the timing difference between the recoil and the ejectile hits falls within the gate described in Section 3.4.

Because of the inability to distinguish between the recoils, the number of reactions measured is that of all three reactions. However, the cross section of the $^{34}$S(α,p$_0$)$^{37}$Cl reaction has been previously measured [63], and that can be used to separate the contribution of $^{34}$S(α,p)$^{37}$Cl from that of $^{34}$Cl(α,p)$^{37}$Ar and $^{34}$Ar(α,p)$^{37}$K. The $^{34}$S(α,p)$^{37}$Cl cross sections at the energies measured in this experiment were $(23.7 \pm 0.8)$ mb for the higher energy and $(25.7 \pm 0.8)$ mb for the lower energy. At the experimental energies, there is only one excited state of $^{37}$Cl that can be populated energetically. According to TALYS-1.8 simulations [22], the cross section of $^{34}$S(α,p)$^{37}$Cl into this excited state is 0 mb at the experimental energies, so the cross section into the ground state is used as the total cross section. $^{34}$Cl(α,p)$^{37}$Ar and $^{34}$Ar(α,p)$^{37}$K are then treated as a single reaction, and so the end result is a cross section of $^{34}$Cl(α,p)$^{37}$Ar and $^{34}$Ar(α,p)$^{37}$K combined.

In the following discussion, $^{34}$S(α,p)$^{37}$Cl, $^{34}$Cl(α,p)$^{37}$Ar, and $^{34}$Ar(α,p)$^{37}$K are referred to as reactions $a$, $b$, and $c$, respectively. The total reactions ($N_{abc}$)—which is what is directly measured—can be split up into the reactions from $a$ and the reactions from $b$ and $c$:

$$N_{abc} = N_a + N_{bc} \tag{3.22}$$

$$= \varepsilon_a f_{\text{live}} \sigma_a \int I_a(t) \rho_A(t)\, \mathrm{d}t + \varepsilon_{bc} f_{\text{live}} \sigma_{bc} \int I_{bc}(t) \rho_A(t)\, \mathrm{d}t\,. \tag{3.23}$$

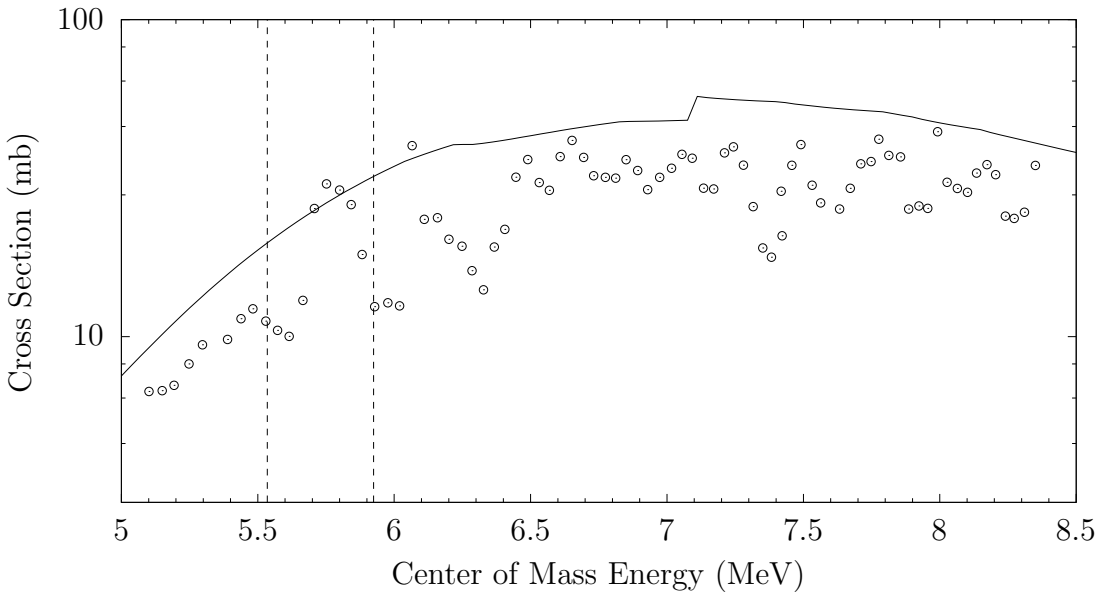


Figure 3.16: The $^{34}$S($\alpha$,p$_0$)$^{37}$Cl cross section data from [63] recreated. The dashed vertical lines indicate the energies at which this experiment was conducted. The solid line shows the cross section calculated by TALYS [22].

Solving for the combined cross section for $b$ and $c$:

$$\sigma_{bc} = \frac{N_{abc} - N_a}{\varepsilon_{bc} \int f_{\text{live}} I_{bc}(t) \rho_A(t)\, \mathrm{d}t}, \text{ where} \tag{3.24}$$

$$N_a = \varepsilon_a \sigma_a \int f_{\text{live}} I_a(t) \rho_A(t)\, \mathrm{d}t\,, \tag{3.25}$$

$\varepsilon_{bc}$ is a combined efficiency for $b$ and $c$, and $I_{bc}$ is the sum of the beam intensities of $b$ and $c$, i.e. $I_{bc} = I_b + I_c$.

The efficiency accounts for all reasons that reactions that occur might not be detected. This includes the intrinsic detector efficiencies, angular coverage, and energy thresholds of the detectors. The intrinsic efficiency of both the silicon detectors and the ionization chamber are assumed to be 100 %. Some detector channels did not function properly; these dead channels were identified using the calibration runs, and they were excluded from the analysis. This effect was accounted for in the efficiency. The angular coverage is calculated as described in

Section 3.2. The angular distribution of the cross section is assumed to be isotropic in the center of mass. In the laboratory reference frame, the reaction is "forward-shifted" because of the reference frame shift; this means the ejectiles are more likely to be detected at angles closer to 0°. The 500 keV energy threshold (described in Section 3.5) affects the ability to detect ejectiles that are emitted closer to 180° and reactions in which the recoil is highly excited.

The efficiency was calculated using a Monte Carlo calculation in which the polar and azimuthal angles and the excitation energy of the recoil are randomized. The angles were chosen isotropically in the center of mass, and the excitation energies were weighted based on Hauser-Feshbach calculations by TALYS-1.8 [22]. Figure 3.17 shows how the efficiency of detecting $^{34}$Ar($\alpha$,p)$^{37}$K reactions changes with respect to the excited state that the $^{37}$K populates. The efficiency increases as excitation energy increases because the ejectiles become more forward-focused, where the detector coverage is greater; it rapidly increases when the ejectiles become fully forward-focused (i.e. all ejectiles are emitted at $> 90°$); and it goes to zero when the ejectiles are so forward-focused that they are not even detected in SIDAR, the most downstream detector section. The calculations were done using the default TALYS parameters in the forward-kinematics frame, meaning the projectiles were $\alpha$-particles with energies of 6.383 MeV and 6.719 MeV. 2, 88, and 94 recoil excited states were used in the calculations for $^{34}$S($\alpha$,p)$^{37}$Cl, $^{34}$Cl($\alpha$,p)$^{37}$Ar, and $^{34}$Ar($\alpha$,p)$^{37}$K, respectively; this accounts for every excited state below the incident energy threshold as reported in [62] (see Figure 3.14). The separate reactions were simulated separately, and with 1 million iterations each, the efficiencies for $^{34}$S($\alpha$,p)$^{37}$Cl, $^{34}$Cl($\alpha$,p)$^{37}$Ar, and $^{34}$Ar($\alpha$,p)$^{37}$K were calculated to be $(30.42 \pm 0.06)\,\%$, $(29.25 \pm 0.05)\,\%$, and $(29.23 \pm 0.05)\,\%$, respectively, with the uncertainties being the statistical uncertainties from the Monte Carlo sampling only. Since

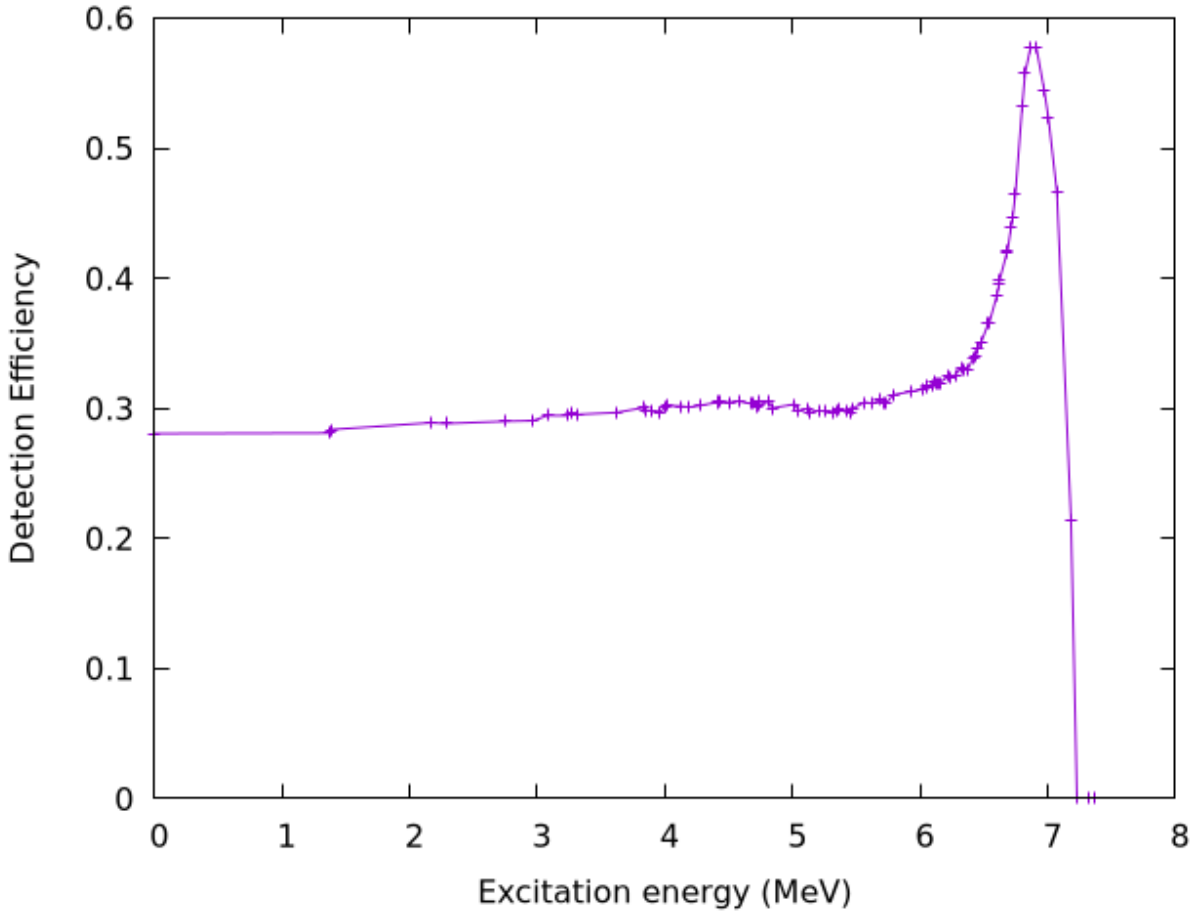


Figure 3.17: The detection efficiency as a function of recoil excitation energy for the $^{34}$Ar(α,p)$^{37}$K reaction. The total detection efficiency is an average of the efficiencies of each level weighted by the relative cross section of the levels.

a combined efficiency is needed for $^{34}$Cl(α,p)$^{37}$Ar and $^{34}$Ar(α,p)$^{37}$K, the average is taken: $\varepsilon_{bc} = (29.24 \pm 0.07)\,\%$. The true efficiency will depend on the ratio of reactions occurring. However, as the two efficiency values agree within uncertainty, the error of the average efficiency encompasses all possibilities.

The uncertainty of the efficiency comes from three sources: 1) the statistical uncertainty from the number of particles that are detected in the Monte Carlo calculation (see above), 2) the weighting of the excited levels, which depends on the Hauser-Feshbach model, and 3) the solid angle. The uncertainty from 2) is estimated from the difference between the overall

detection efficiency and the detection efficiency of the ground state, which is 28.5 %. The uncertainty from 3) is taken from the Monte Carlo calculation in Section 3.2 propagated to the efficiency using $\frac{\sigma_\varepsilon}{\varepsilon} = \frac{\sigma_\Omega}{\Omega} = 0.141$.

The integral of the product of the areal density of the jet and the intensity of beam $x$ will be referred to as $S_x$, i.e.

$$S_x = \int f_{\text{live}} \rho_A(t) I_x(t)\, \mathrm{d}t\,. \tag{3.26}$$

Since the areal density and the beam intensity vary throughout the experiment but vary little throughout a single run, $S_x$ can be expressed as

$$S_x = \sum_i \langle \rho_A \rangle_i \mathfrak{n}_{x,i}, \tag{3.27}$$

where $\langle \rho_A \rangle_i$ is the average areal density for run $i$ and $\mathfrak{n}_{x,i}$ is the number of beam particles of species $x$ delivered to the experiment for run $i$ (this quantity takes into account the factor of $f_{\text{live}}$ because this quantity is measured by a scaler that is vetoed if the DAQ system is unable to read). This means the final equation used to calculated the combined cross section of $^{34}$Cl(α,p)$^{37}$Ar and $^{34}$Ar(α,p)$^{37}$K is

$$\begin{aligned} \sigma_{bc} &= \frac{N_{abc} - N_a}{\varepsilon_{bc} S_{bc}} \\ N_a &= \varepsilon_a \sigma_a S_a \end{aligned} \tag{3.28}$$

The areal density of the target is measured using the pressure of the gas after the compressor and right before entering the nozzle ($\text{CAP}_{\text{in}}$, shown in Figure 2.3). Prior to the experiment, the relationship between $\text{CAP}_{\text{in}}$ and $\rho_A$ was measured, as described in Sec-

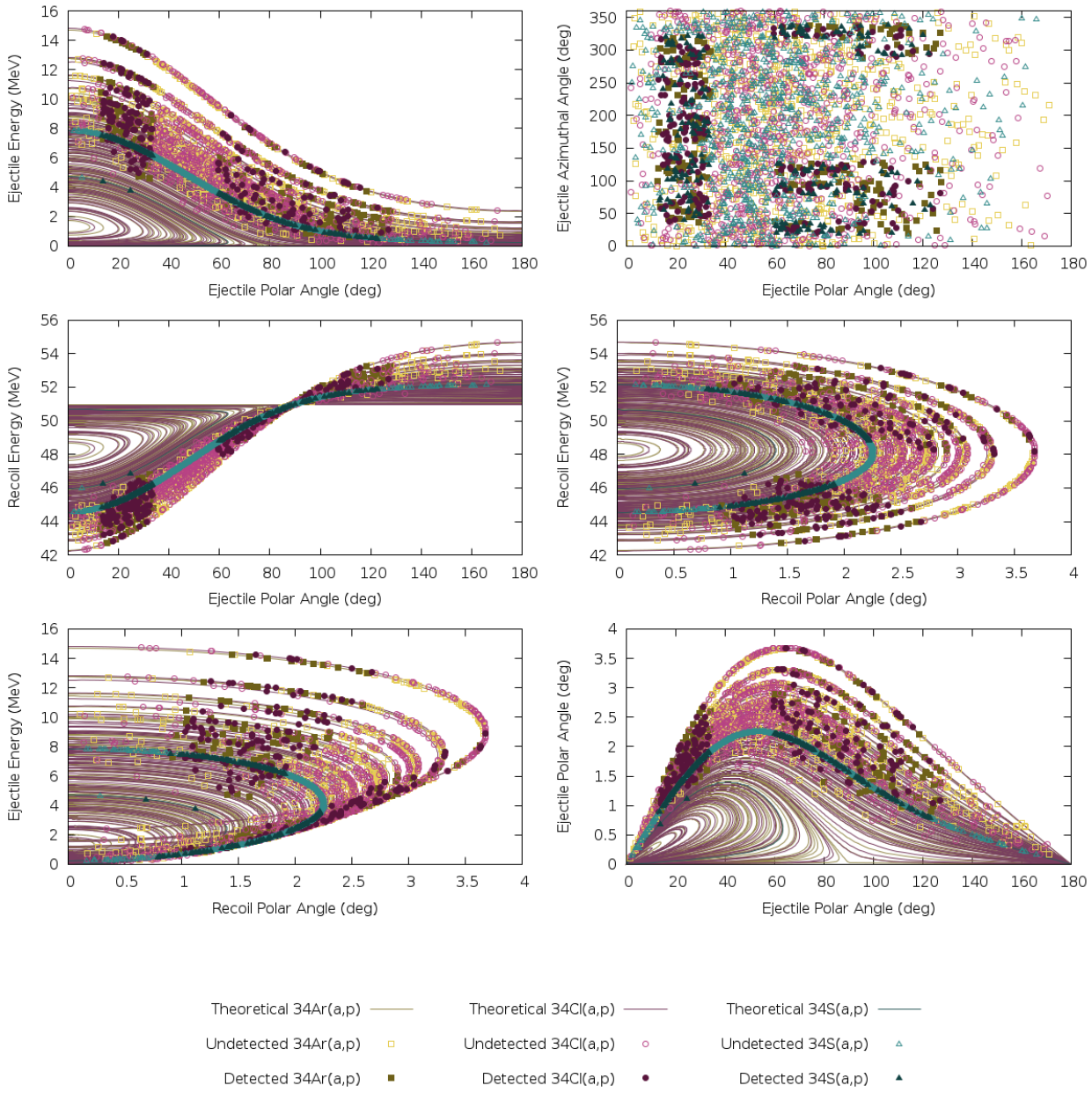


Figure 3.18: An example of a Monte Carlo simulation used to calculate the efficiency of detecting each reaction. The filled shapes are events that are detected, and the unfilled shapes are those that are not detected.

tion 2.2.1.

An $^{241}$Am α-particle source was positioned facing the jet with a Micron BB15 detector on the other side of the jet to detect the α-particles. The α-particles lost energy in the target proportional to the areal density of the target. By measuring the difference between the energy of the α-particles traveling through the jet at a given pressure and the energy of the α-particles traveling through no jet, a $\mathrm{CAP_{in}}$–$\rho_A$ relationship was determined.

Three tests were done with the nozzle used in the experiment, varying the amount of gas in the system. The pressure measured at $\mathrm{P_{disch}}$ for each was (150, 250, and 350) psig. The average measurements for $\mathrm{CAP_{in}}$ for these runs were (6.18, 9.52, and 13.4) $\times 10^3$ Torr, and the areal density through the jet at the height of the beam axis were (4.40, 6.3, and 7.9) $\times 10^{18}$ atoms/cm$^2$ [64].

Figure 3.19 shows the data from this calibration, the calibration function, and the data from the experimental runs to which the calibration is being applied. The calibration function is

$$\rho_A = a(\mathrm{CAP_{in}} - \mathrm{CAP_{in,0}}) + b, \tag{3.29}$$

where $a$ and $b$ are the adjustable parameters of the fit function and $\mathrm{CAP_{in,0}}$ is a constant. $\mathrm{CAP_{in,0}} = 12.5 \times 10^3$ Torr, $a = 4.99 \times 10^{14}$ (atoms/cm$^2$)/Torr, and $b = 7.60 \times 10^{18}$ atoms/cm$^2$. $\mathrm{CAP_{in}}$ was averaged for each run, and this calibration was used to calculate the average areal density for each run.

The time integral $\int I \, \mathrm{d}t$ is the number of beam particles delivered to the target. The beam intensity depends on which reaction is being considered. For the $^{34}$S(α,p)$^{37}$Cl cross section, $I_{^{34}\mathrm{S}}$ is used, for the combined $^{34}$Cl(α,p)$^{37}$Ar and $^{34}$Ar(α,p)$^{37}$K cross section, $I_{^{34}\mathrm{Cl}} + I_{^{34}\mathrm{Ar}}$ is used. The total number of beam particles delivered to the target ($\mathfrak{n}_{\mathrm{tot}}$) is the number

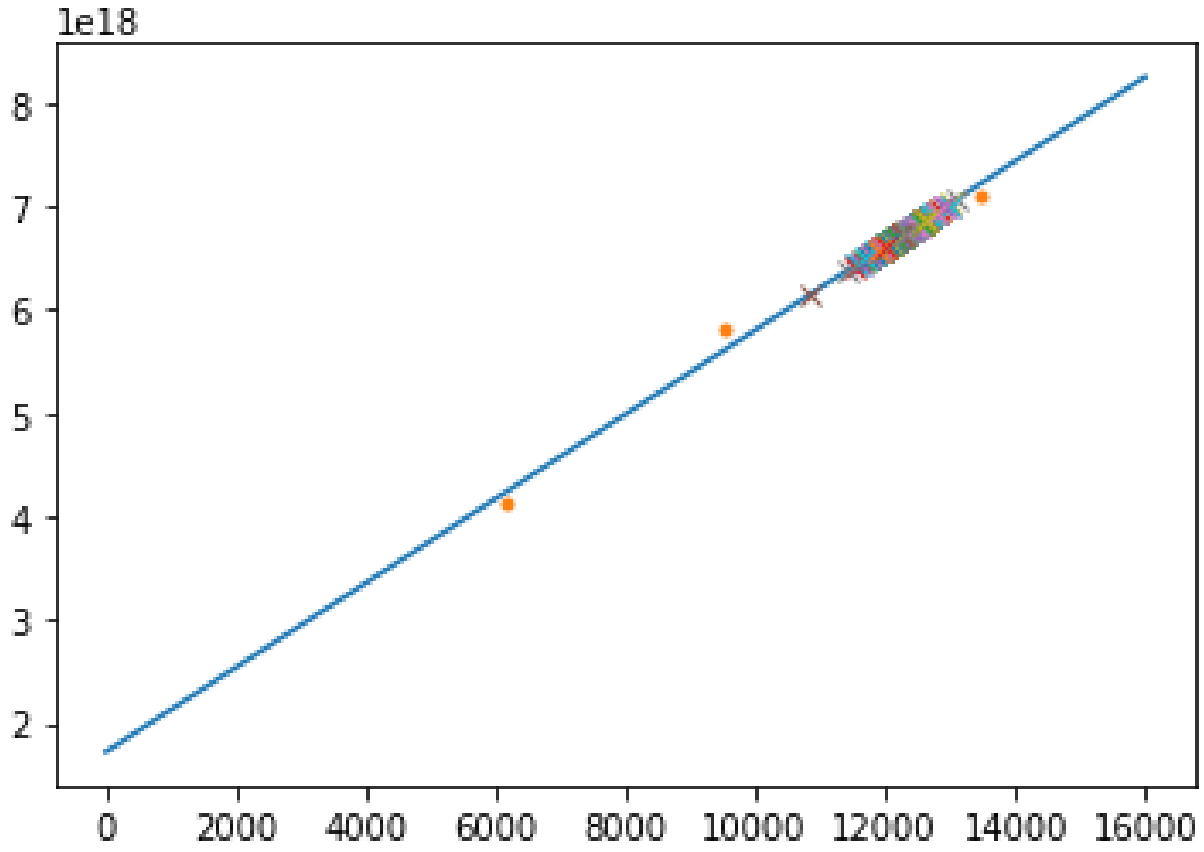


Figure 3.19: The relationship between the target areal density and the pressure measured at $CAP_{in}$. The circles are the calibration points, and the crosses are the experimental values that were calibrated using this fit.

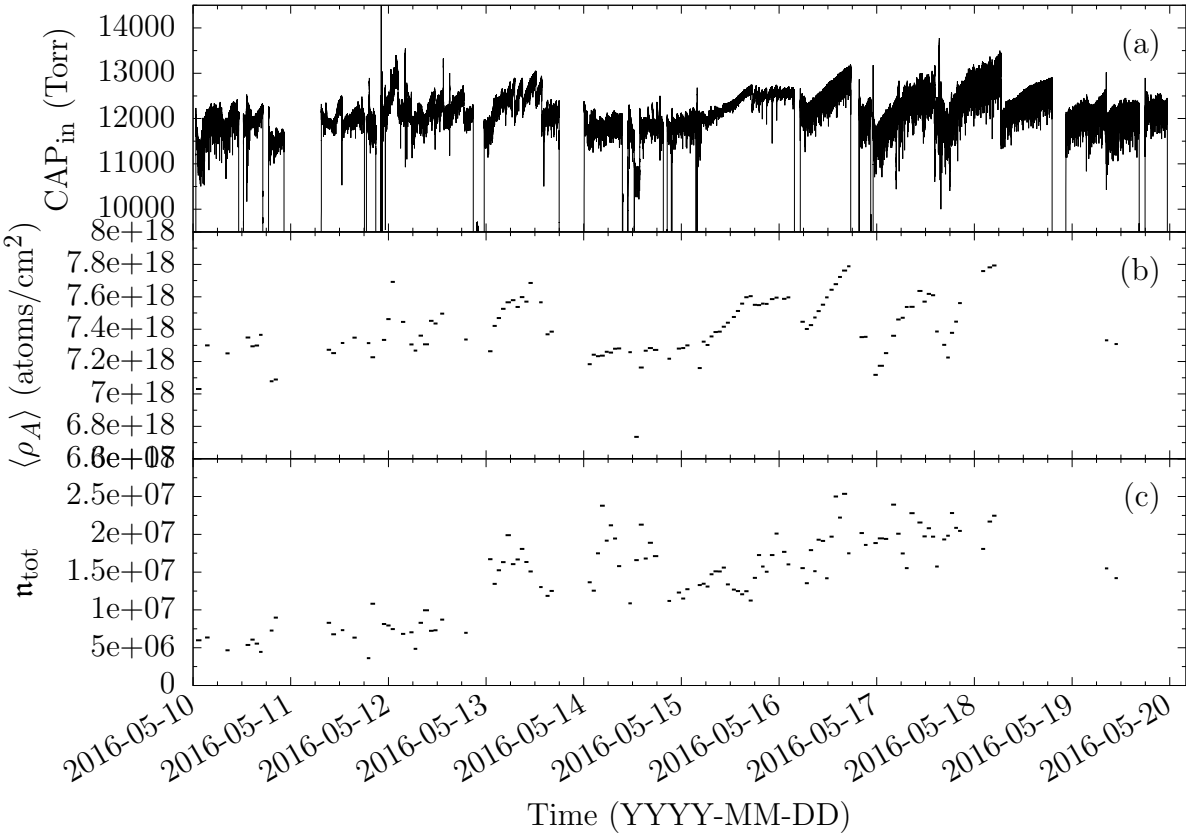


Figure 3.20: The time series data that changes for each run.

of triggers during the run in the dE section of the ionization chamber, counted by a scaler module in the DAQ. The individual values are calculated by $n_X = f_X \mathfrak{n}_{\mathrm{tot}}$, where $X$ is the beam species of interest, and $f_X$ is the fraction of the total beam that is species $X$. The values of $f_X$ are taken as the counts within the gates shown in Figure 3.7b. The values of $f_X$ vary by run.

# Chapter 4

# Results

Equations (3.24) to (3.26) are the equations used to calculated the combined cross section of $^{34}$Cl(α,p)$^{37}$Ar and $^{34}$Ar(α,p)$^{37}$K.

The two experimental energies are $(5.91 \pm 0.08)$ MeV and $(5.51 \pm 0.08)$ MeV in the center of mass frame (see Section 3.1). They are referred to as E1 and E2, respectively. For E1, 67 total reactions were detected, leading to a statistical uncertainty of 8 for the cross section determination; $1.6 \pm 0.1$ of these were attributed to $^{34}$S(α,p)$^{37}$Cl. The beam weighting ratios were $S_b/S_{bc} = 32.3\,\%$ and $S_c/S_{bc} = 67.7\,\%$, where $S_x$ is given in Equation (3.26), $b$ refers to $^{34}$Cl(α,p)$^{37}$Ar, $c$ refers to $^{34}$Ar(α,p)$^{37}$K, and $bc$ refers to the combination of the two. The resulting combined cross section for $^{34}$Cl(α,p)$^{37}$Ar and $^{34}$Ar(α,p)$^{37}$K is $(70 \pm 21)$ mb, where the uncertainty of 21 mb is composed of a 9 mb statistical uncertainty and a 12 mb systematic uncertainty.

For E2, 216 total reactions were detected, leading to a statistical uncertainty of 15 for the cross section determination; $4.4 \pm 0.3$ of these were attributed to $^{34}$S(α,p)$^{37}$Cl. The beam weighting ratios were $S_b/S_{bc} = 33.5\,\%$ and $S_c/S_{bc} = 66.5\,\%$. The resulting combined cross section for $^{34}$Cl(α,p)$^{37}$Ar and $^{34}$Ar(α,p)$^{37}$K is $(52 \pm 13)$ mb, where the uncertainty of 13 mb is composed of a 4 mb statistical uncertainty and a 9 mb systematic uncertainty.

The relative uncertainties of the inputs of Equation (3.24) are shown in Table 4.1. The largest source of uncertainty in this experiment is the systematic uncertainty of the efficiency,

Table 4.1: The relative uncertainties of the quantities used to calculate the combined $^{34}$Cl(α,p)$^{37}$Ar and $^{34}$Ar(α,p)$^{37}$K cross section.

| | | Statistical | Systematic |
|---|---|---|---|
| E1 | $N_{abc}$ | 12 % | – |
| | $\sigma_a$ | – | 6 % |
| | $\varepsilon_x$ | 0.2 % | 17 % |
| | $S_x$ | 0.3 % | 3 % |
| E2 | $N_{abc}$ | 7 % | – |
| | $\sigma_a$ | – | 7 % |
| | $\varepsilon_x$ | 0.2 % | 17 % |
| | $S_x$ | 0.2 % | 4 % |

which comes from the uncertainty in the solid angle (see Section 3.2).

## 4.1 Discussion

To compare to the predictions of Hauser-Feshbach theory, Hauser-Feshbach predictions of the cross sections were calculated using TALYS-1.8 [22]. The cross section for $^{34}$Cl(α,p)$^{37}$Ar was calculated to be 142.8 mb and 89.8 mb at E1 and E2, respectively, and the corresponding values for $^{34}$Ar(α,p)$^{37}$K were 95.0 mb and 52.2 mb. To compare these Hauser-Feshbach predictions to the combined cross section that we determined in this experiment, a weighted average of the two was calculated:

$$\sigma_{bc} = \frac{S_b}{S_{bc}}\sigma_b + \frac{S_c}{S_{bc}}\sigma_c. \tag{4.1}$$

These weights, $S_x/S_{bc}$, factor in how much beam and target are interacting in each experimental run. This gives a prediction of 110.4 mb for E1 and 64.8 mb for E2. A comparison of these predictions with the experimental results is shown in Figure 4.1.

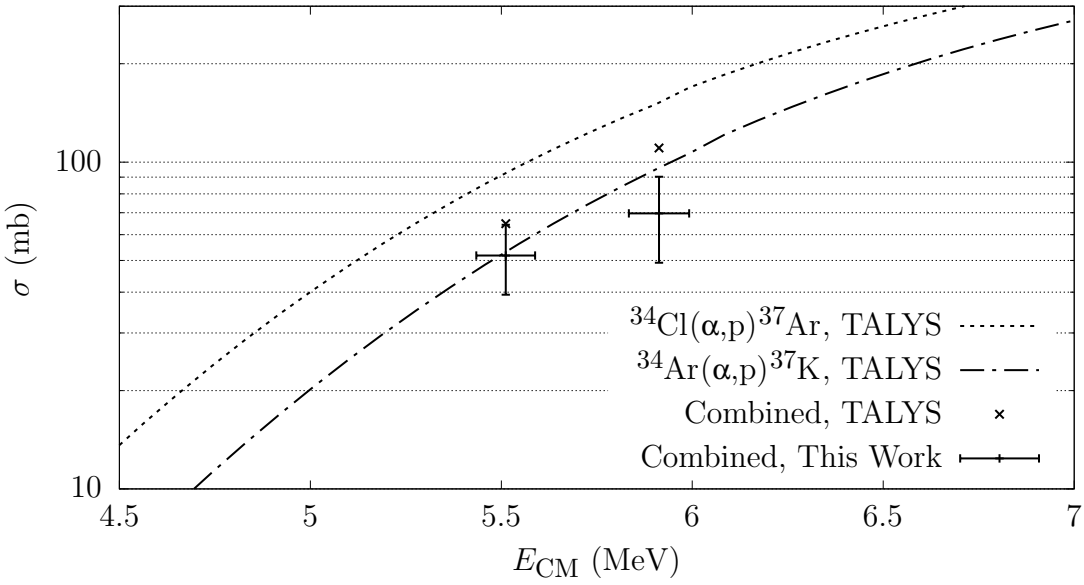


Figure 4.1: The experimentally measured $^{34}$Cl(α,p)$^{37}$Ar + $^{34}$Ar(α,p)$^{37}$K cross section, with the Hauser-Feshbach predictions, calculated using TALYS-1.8 [22]. The predicted cross sections are weighted averages of the two cross sections, which are also shown. The weights for the $^{34}$Ar(α,p)$^{37}$K cross section are 67.7 % for E1 and 66.5 % for E2.

# Chapter 5

# Conclusions

The purpose of this experiment was to directly measure the $^{34}$Ar(α,p)$^{37}$K cross section. Because of the contamination of the $^{34}$Ar beam with the daughter and grand-daughter $^{34}$Cl and $^{34}$S nuclides and the inability to distinguish between the recoils of the three (α,p) reactions in the ionization chamber, an individual measurement of the $^{34}$Ar(α,p)$^{37}$K reaction was not possible. However, the contribution from $^{34}$S(α,p)$^{37}$Cl could be isolated because it had been previously measured, and a combined cross section for $^{34}$Cl(α,p)$^{37}$Ar and $^{34}$Ar(α,p)$^{37}$K could be determined.

This combined cross section can now be used to test Hauser-Feshbach model predictions. The experimental combined cross sections are 37 % and 20 % lower than Hauser-Feshbach predictions at E1 and E2, respectively. The conclusion is, therefore, that Hauser-Feshbach calculations overestimate these reaction rates by a factor of 1.25–1.58. Given typical uncertainties of the Hauser-Feshbach method, this can be considered reasonable agreement, especially for unstable nuclei.

Previous measurements have been conducted to indirectly inform the astrophysical reaction rate. [29] and [30] report $N_A\langle\sigma v\rangle$ to be approximately a factor of 0.05 lower than Hauser-Feshbach predictions; however, a rate with enhanced α-spectroscopic factors, to account for α-clustering, is on the same order of magnitude as the predictions. An example cross section [23] from a Monte Carlo analysis in [30] (shown in Section 1.2.1) shows a dis-

crepancy with Hauser-Feshbach predictions of up to 3 orders of magnitude. Preliminary results from [31], which have not been published, show the rate of the inverse reaction, $^{37}$K(p,$\alpha$)$^{34}$Ar, to be about an order of magnitude lower than Hauser-Feshbach predictions.

The results from this work show that the hypothesis that Hauser-Feshbach overestimates the reaction rate by orders of magnitude is unlikely to be true at these energies, indicating the possibility that $\alpha$-clustering enhancements compensate for the low level density. However, because the contributions from $^{34}$Cl($\alpha$,p)$^{37}$Ar and $^{34}$Ar($\alpha$,p)$^{37}$K cannot be distinguished, it is possible that one reaction is overestimated by Hauser-Feshbach and the other is underestimated.

A similar story has played out for $^{22}$Mg($\alpha$,p)$^{25}$Al. Indirect measurement had suggested that the astrophysical rate would be much lower than predicted by Hauser-Feshbach [65]. The direct measurement reports a cross section that, while still lower than the Hauser-Feshbach prediction, is much closer than indirect measurements would suggest [26]. However, unlike in this work, the discrepancy is still a factor of 8, much larger than our (20–40) %. This may indicate that for heavier mass reactions Hauser-Feshbach calculations become more reliable.

Given that these results indicate that Hauser-Feshbach overpredicts the results by less than a factor of 2, but the previous measurements of $^{22}$Mg($\alpha$,p)$^{25}$Al indicates that Hauser-Feshbach overpredicts the results by a factor of 8, it appears more data, especially in the Gamow window, is needed to see if this overprediction is systematic, and if so, how large it is at the astrophysically relevant energies.

This experiment demonstrates the ability to measure the ($\alpha$,p) cross sections on the important waiting points in the $\alpha$p-process that occurs in x-ray bursts using the JENSA gas jet target system with the SuperORRUBA and SIDAR Si detectors.

Future experiments could improve upon this method by using a beam stopping detector—

such as an ionization chamber—that can handle the intensity of the delivered beam, and can measure the energy with enough precision to differentiate the different recoil species. This would allow for the different ($\alpha$,p) reactions to be identified, and the reaction rate for each could be measured. Alternatively, the $^{34}$Cl($\alpha$,p)$^{37}$Ar cross section could be measured separately, which would allow for the contribution from that reaction to be subtracted in the same way that the contribution from $^{34}$S($\alpha$,p)$^{37}$Cl is subtracted in this work. The uncertainty can be decreased by increasing the intensity of the beam or increasing the density of the target; however, a thicker target also increases the energy spread of the beam.

# Appendix A

# JENSA Manual

## Vacuum System Startup

This is the procedure to evacuate the chamber side of the system. It assumes that the pumps are turned off and the system is either filled with gas or being held at a static vacuum. This does not evacuate the compressor (See Compressor Startup).

1. Seal the main chamber.
2. Close $V_{in}$ and $V_{comp\_in}$, isolating the compressor from the chamber.
3. Turn on cooling water.
   (a) Open return valve.
   (b) Open intake valve.
   (c) Close loop valve.
   (d) Check flow meters under the compressor to ensure cooling water is flowing. If the flow does not increase, make sure the cooling water valves under the compressor are open.
   (e) Check flow meters next to the turbo pumps to ensure cooling water is flowing. If the flow does not increase, make sure the cooling water valves next to the turbo pumps are open.

4. Start the Roughing Pump.

5. Slowly open $V_{rough}$.

6. Turn on the Leybold Control Panel.

7. Slowly open $V_{ley\_out}$. Gas will enter the Roughing Pump and it will start working harder. To prevent damage to the Roughing Pump, limit the flow of gas into it by opening $V_{ley\_out}$ only a little.

8. Open $V_{gate}$.

9. Wait until $PIR_{ch} \leq 100\,\text{Torr}$.

10. Turn on Pump L1–Pump L3 with the "Start System" button on the Leybold Control Panel.

11. Press Reset Button on the Leybold Control Panel to override faulty valve $V_{ley1}$.

12. Turn on the Motor Control Panel panel by pulling the silver button.

13. Turn on Pump 8–Pump 9, waiting 10 s after each. Check that they each spin up. If the noise enclosure is closed, it may be difficult to notice.

14. Turn on Pump 11–Pump 13, waiting 10 s after each. Check that they each spin up.

15. Turn on Pump 10. Check that it is spinning up.

16. Turn on Pump 7. Check that it is spinning up. Wait until $PIR_{ch} \leq 1 \times 10^{-1}\,\text{Torr}$.

17. Turn on Shimadzu. Wait until the pump speed is $> 5\,\%$ and $PIR_{turbo} \leq 5 \times 10^{-2}\,\text{Torr}$.

18. Turn on UP1–UP4 and (if attached) DN1–DN4. Start with UP1 and DN1 and increment to UP4 and DN4, waiting 20 s after each start.

19. Turn on pressure sensors CCU1–CCU4 and (if attached) CCD1–CCD4.

# Compressor Evacuation

This procedure is for removing the gas from the compressor. This must be done before filling the compressor with the desired gas. If the desired gas is already in the compressor or it is already evacuated, it is not necessary to do this.

This assumes the compressor is isolated from the main chamber and pumps ($V_{in}$ and $V_{comp\_in}$ are closed) and that the Roughing Pump is on.

1. If the main chamber and pumps are not evacuated,
   (a) Close $V_{ley\_out}$, isolating them from the Roughing Pump.
   (b) Wait until $PIR_{rough} \leq 100\,\text{Torr}$.
2. Close $V_{104\_man}$ and $V_{air1}$, and open $V_{air2}$. This will open the internal valves, making the compressor one connected vessel that can be evacuated all at once. It is normal to hear compressed air being loudly vented.
3. Close $V_{gauge}$. This ensures that the 3 psi gauge stays within its range. Going outside of its range could damage the spring, affecting its calibration.
4. Slowly open $V_{comp\_in}$. Gas from the compressor will enter the Roughing Pump and it will start working harder. To prevent damage to the Roughing Pump, limit the flow of gas into it by opening $V_{comp\_in}$ only a little.
5. Wait until $P_{inter}$, $P_{inter}$, $P_{upstr}$, and $P_{disch}$ all $\approx 0\,\text{psig}$.
6. Close $V_{comp\_in}$.
7. Close $V_{air2}$, and open $V_{104\_man}$ and $V_{air1}$.

# Compressor Startup

This procedure is for starting the compressor and creating a loop of gas going from the compressor outlet, through $NV_{loop}$, and into the compressor inlet.

It assumes the compressor is either evacuated or filled with the target gas. If this is not the case, see Compressor Evacuation.

It also assumes the compressor is isolated from the main chamber and pumps. This means $V_{in}$ and $V_{comp\_in}$ must be closed.

$V_{104\_man}$ and $V_{air1}$ must be open, and $V_{air2}$ must be closed. The compressed air lines should not be making noise. This is the normal operating setup. If the compressor shuts off after the 30 s interlock stage and there is enough gas in the system, it may be because $V_{104\_man}$ is closed.

1. Turn on the Compressor Control Panel.
2. Open $PV_{loop}$ using the EPICS control panel.
3. Open $NV_{loop}$ completely.
4. Close $NV_{hm}$ completely.
5. Close $V_{gauge}$. This ensures that the 3 psi gauge stays within its range. Going outside of its range could damage the spring, affecting its calibration.
6. Close $REG_{bot}$ completely by turning the dial counter-clockwise.
7. Open $V_{bot1}$.
8. Adjust $REG_{bot}$ to 30 psi downstream.

9. Increase $P_{inlet}$ to 15 psig by opening valve $V_{bot2}$. Close $V_{bot2}$ when 15 psig is reached.

10. Start the compressor by pressing the green start button on the Compressor Control Panel.

11. After about 30 s, the interlock stage will end, and the second stage of the compressor will open. $P_{disch}$ will increase, and $P_{inlet}$ will decrease.

12. Add gas (see Adjusting Compressor Pressures) so that $4\,\text{psig} \leq P_{inlet} \leq 5\,\text{psig}$ and $150\,\text{psig} \leq P_{disch} \leq 200\,\text{psig}$.

# Adjusting Compressor Pressures

The density of the jet can be changed by changing $P_{disch}$. This can be done by adjusting $NV_{loop}$, which affects the ratio of gas going through the nozzle to gas going through the bypass loop. This also affects $P_{inlet}$, so amount of gas in the system must be adjusted to assure that the compressor is able to run.

It is important to note that $NV_{loop}$ affects $P_{inlet}$ and $P_{disch}$ non-linearly. When $NV_{loop}$ is closed, small changes affect the pressures significantly, but when $NV_{loop}$ is open, it must be opened or closed a lot in order to affect the pressures.

This assumes $V_{bot1}$ is open and $REG_{bot}$ is set to allow gas to flow into the system.

## Increasing $P_{disch}$, Decreasing $P_{inlet}$

1. Close $NV_{loop}$ while $P_{inlet} \geq 0.5\,\text{psig}$. This will redirect gas from the bypass loop to the nozzle, increasing $P_{disch}$ and decreasing $P_{inlet}$.

2. Open $V_{bot2}$ while $P_{inlet} \leq 1.0\,\text{psig}$. This will add gas to the system, increasing $P_{disch}$ and $P_{inlet}$.

3. Repeat from step 1, maintaining $0.5\,\text{psig} \leq P_{inlet} \leq 1\,\text{psig}$, until $P_{disch}$ is at the desired setting.

## Decreasing $P_{disch}$, Increasing $P_{inlet}$

1. Open $NV_{loop}$ while $P_{inlet} \leq 1.0\,\text{psig}$. This will redirect gas from the nozzle to the bypass loop, decreasing $P_{disch}$ and increasing $P_{inlet}$.

2. Open $NV_{vent}$ while $P_{inlet} \geq 0.5\,\text{psig}$. This will remove gas to the system, decreasing

$P_{disch}$ and $P_{inlet}$.

3. Repeat from step 1, maintaining $0.5\,\text{psig} \leq P_{inlet} \leq 1\,\text{psig}$, until $P_{disch}$ is at the desired setting.

# Jet Startup

This procedure will start a jet in the main chamber. This assumes that the vacuum system is running and the compressor is on (see Vacuum System Startup and Compressor Startup) and that the main chamber and pumps are separated from the compressor.

This assumes $V_{rough}$ and $PV_{inlet}$ are open. It also assumes $V_{bot1}$ is open and $REG_{bot}$ is set to allow gas to flow into the system.

1. Close D1483 using the EPICS control panel. This ensures that if there is a failure that leads to gas filling the chamber, the beamline and accelerator are not affected.

2. Open $V_{bot2}$ to add gas to the system until $4\,\text{psig} \leq P_{inlet} \leq 5\,\text{psig}$.

3. Close $V_{rough}$.

4. Slowly open $V_{comp\_in}$ and maintain $0.5\,\text{psig} \leq P_{inlet} \leq 1\,\text{psig}$ (see Adjusting Compressor Pressures). This will cause gas to enter the pumps and main chamber and $P_{inlet}$ to decrease. Because of this, adding gas will be necessary.

5. Slowly open $V_{in}$ and maintain $0.5\,\text{psig} \leq P_{inlet} \leq 1\,\text{psig}$ (see Adjusting Compressor Pressures). Pump loads will increase.

6. After adjustments, open valve $V_{gauge}$ to observe $P_{inlet}$ pressure more precisely on the 3 psig gauge.

7. Close $V_{bot2}$.

# Shutdown

This procedure is for turning off the jet and turning off all of the pumps in the system. This leaves the system in a state that requires no oversight.

This assumes all the pumps are on and the jet is flowing, i.e. the compressor is on and $V_{in}$ and $PV_{inlet}$ are open.

1. Reduce the gas by adjusting $P_{disch}$ to (150–200) psig (see Adjusting Compressor Pressures).
2. Turn off CCU1 – CCU4 and (if attached) CCD1 – CCD4.
3. Isolate the compressor from the main chamber and pumps by closing $V_{in}$ and $V_{comp\_in}$.
4. Slowly open $V_{rough}$.
5. Turn off the compressor by pressing red button on the Compressor Control Panel.
6. Turn off UP1 – UP4 and (if attached) DN1 – DN4. Start with UP4 and DN4 and decrement to UP1 and DN1. Wait 10 s after each stop.
7. Turn off Shimadzu.
8. Turn off Pump 7.
9. Wait 10 s
10. Turn off Leybold WSU2001 pumps in the following order and wait 10 s after each: switches 10, 13, 12, 11.
11. Turn off Pump 9 and Pump 8 and wait 10 s after each.

12. Turn off Pump L1 – Pump L3 with the "System Stop" button on the Leybold Control Panel.

13. Wait for pumps to spin down.

14. Close $V_{rough}$.

15. Turn off the Roughing Pump.

16. Turn off the Motor Control Panel.

17. Turn off the Leybold Control Panel.

18. To vent the chamber with air, slowly open $NV_{vent2}$.

## Emergency Shutdown

This procedure is for when there is a failure in any part of the system, such as the compressor shutting off or one of the roots blowers shutting off. Such circumstances, if left unresolved, could lead to damaging the pumps or experimental equipment. The remedy is to isolate the compressor from the main chamber and pumps and to evacuate the main chamber and pumps.

1. Close $V_{in}$.
2. Close $V_{comp\_in}$.
3. Open $V_{rough}$.

# BIBLIOGRAPHY

# BIBLIOGRAPHY


[1] C. Iliadis, *Nuclear Physics of Stars* (Wiley-VCH, 2015), pp. 31–33.

[2] H. Schatz and K. E. Rehm, Nucl. Phys. A **777**, 601 (2006) DOI: 10.1016/j.nuclphysa.2005.05.200.

[3] C. J. Hansen and H. M. van Horn, Astrophys. J. **195**, 735 (1975) DOI: 10.1086/153375.

[4] H. Schatz et al., Phys. Rev. Lett. **86**, 3471 (2001) DOI: 10.1103/physrevlett.86.3471.

[5] B. Paczynski, Astrophys. J. **267**, 315 (1983) DOI: 10.1086/160870.

[6] M. Sztajno et al., Astrophys. J. **299**, 487 (1985) DOI: 10.1086/163715.

[7] W. Penninx et al., Astron. Astrophys. **208**, 146 (1989), https://ui.adsabs.harvard.edu/abs/1989A&A...208..146P.

[8] E. Kuulkers et al., Astron. Astrophys. **382**, 947 (2002) DOI: 10.1051/0004-6361:20011656.

[9] J. van Paradijs et al., Mon. Not. R. Astron. Soc. **221**, 617 (1986) DOI: 10.1093/mnras/221.3.617.

[10] G. Zhang et al., Mon. Not. R. Astron. Soc. **398**, 368 (2009) DOI: 10.1111/j.1365-2966.2009.15148.x.

[11] J. L. Fisker, F.-K. Thielemann, and M. Wiescher, Astrophys. J. **608**, L61 (2004) DOI: 10.1086/422215.

[12] R. H. Cyburt et al., Astrophys. J. **830**, 55 (2016) DOI: 10.3847/0004-637x/830/2/55.

[13] L. Bildsten, in AIP conference proceedings (2000), DOI: 10.1063/1.1291736.

[14] H. Schatz et al., Astrophys. J. **524**, 1014 (1999) DOI: 10.1086/307837.

[15] W. Hauser and H. Feshbach, Phys. Rev. **87**, 366 (1952) DOI: 10.1103/physrev.87.366.

[16] J. J. Cowan, F.-K. Thielemann, and J. W. Truran, Phys. Rep. **208**, 267 (1991) DOI: 10.1016/0370-1573(91)90070-3.

[17] T. Rauscher, F.-K. Thielemann, and K.-L. Kratz, Nucl. Phys. A **621**, 331 (1997) DOI: 10.1016/s0375-9474(97)00266-2.

[18] H. Schatz et al., Phys. Rep. **294**, 167 (1998) DOI: 10.1016/s0370-1573(97)00048-3.

[19] C. Iliadis, *Nuclear Physics of Stars* (Wiley-VCH, 2015), pp. 133–137.

[20] A. Koning, S. Hilaire, and S. Goriely, *TALYS-1.8: A nuclear reaction program – User Manual* (Dec. 2015), pp. 83–92.

[21] T. Rauscher and F.-K. Thielemann, At. Data Nucl. Data Tables **75**, 1 (2000) DOI: 10.1006/adnd.2000.0834.

[22] A. J. Koning, S. Hilaire, and M. C. Duijvestijn, in ND2007 (2007), DOI: 10.1051/ndata:07767.

[23] A. M. Long, Private communication, 2016.

[24] S. Almaraz-Calderon et al., Phys. Rev. Lett. **112**, DOI: 10.1103/physrevlett.112.152701 (2014) DOI: 10.1103/physrevlett.112.152701.

[25] R. H. Cyburt et al., Astrophys. J. Suppl. Ser. **189**, 240 (2010) DOI: 10.1088/0067-0049/189/1/240.

[26] J. S. Randhawa et al., (2020).

[27] S. O'Brien et al., in AIP conference proceedings (2009), DOI: 10.1063/1.3087029.

[28] S. P. O'Brien, "Exploring the αp-process with high precision (p,t) reactions", PhD thesis (University of Notre Dame, 2010), https://curate.nd.edu/show/rj430289f1w.

[29] A. M. Long, "An Indirect Study of the Astrophysical $^{34}$Ar(α,p)$^{37}$K Reaction and its Influence on Type-1 X-ray Burst Light Curves", PhD thesis (University of Notre Dame, 2016), https://curate.nd.edu/show/rx913n22m9v.

[30] A. M. Long et al., Phys. Rev. C **95**, DOI: 10.1103/physrevc.95.055803 (2017) DOI: 10.1103/physrevc.95.055803.

[31] C. Deibel et al., in Proceedings of XII international symposium on nuclei in the cosmos — PoS(NIC XII) (Apr. 2013), DOI: 10.22323/1.146.0044.

[32] A. C. Lauer, "Studying the Reaction $^{34}$Ar(α,p)$^{37}$K and its Impact on XRB Nucleosynthesis and Observables", PhD thesis (Louisiana State University at Baton Rouge, 2017), https://digitalcommons.lsu.edu/gradschool_dissertations/4118.

[33] C. Iliadis, *Nuclear Physics of Stars* (Wiley-VCH, 2015), pp. 75–77.

[34] D. J. Morrissey and B. M. Sherrill, in *The Euroschool Lectures on Physics with Exotic Beams, Vol. I*, edited by J. S. Al-Khalili and E. Roeckl (Springer-Verlag Berlin Heidelberg, 2004), pp. 113–135.

[35] D. J. Morrissey et al., Nucl. Instrum. Methods Phys. Res. B **204**, 90 (2003) DOI: 10.1016/s0168-583x(02)01895-5.

[36] H. Geissel et al., Nucl. Instrum. Methods Phys. Res. A **282**, 247 (1989) DOI: 10.1016/0168-9002(89)90148-4.

[37] L. Weissman et al., Nucl. Phys. A **746**, 655 (2004) DOI: 10.1016/j.nuclphysa.2004.09.045.

[38] L. Weissman et al., Nucl. Instrum. Methods Phys. Res. A **540**, 245 (2005) DOI: 10.1016/j.nima.2004.11.048.

[39] K. Cooper et al., Nucl. Instrum. Methods Phys. Res. A **763**, 543 (2014) DOI: 10.1016/j.nima.2014.06.075.

[40] A. Lapierre et al., J. Instrum. **5**, c07001 (2010) DOI: 10.1088/1748-0221/5/07/c07001.

[41] O. Kester et al., Proceedings of the SRF2009, Berlin, Germany, 57 (2009).

[42] C. Iliadis, *Nuclear Physics of Stars* (Wiley-VCH, 2015), pp. 163–167.

[43] N. Nica and B. Singh, Nucl. Data Sheets **113**, 1563 (2012) DOI: 10.1016/j.nds.2012.06.001.

[44] K. A. Chipps et al., Nucl. Instrum. Methods Phys. Res. A **763**, 553 (2014) DOI: 10.1016/j.nima.2014.06.042.

[45] *The Vacuum Technology Book, Volume II* (Pfeiffer Vacuum GmbH, 2013), https://www.pfeiffer-vacuum.com/en/know-how/.

[46] M. S. Basunia, Nucl. Data Sheets **107**, 2323 (2006) DOI: 10.1016/j.nds.2006.07.001.

[47] C. Hanke and J. Laursen, Nucl. Instrum. Methods **151**, 253 (1978) DOI: 10.1016/0029-554x(78)90497-4.

[48] K. Schmidt et al., Nucl. Instrum. Methods Phys. Res. A **911**, 1 (2018) DOI: 10.1016/j.nima.2018.09.052.

[49] D. W. Bardayan et al., Nucl. Instrum. Methods Phys. Res. A **711**, 160 (2013) DOI: 10.1016/j.nima.2013.01.035.

[50] D. W. Bardayan et al., Phys. Rev. C **63**, DOI: 10.1103/physrevc.63.065802 (2001) DOI: 10.1103/physrevc.63.065802.

[51] J. Lai et al., Nucl. Instrum. Methods Phys. Res. A **890**, 119 (2018) DOI: 10.1016/j.nima.2018.01.010.

[52] J. Lai, "A direct study of 20Ne(a,p)23Na with the HELIcal Orbit Spectrometer (HELIOS)", PhD thesis (Louisiana State University at Baton Rouge, 2016), https://digitalcommons.lsu.edu/gradschool_dissertations/2625.

[53] https://epics-controls.org.

[54] L. R. Dalesio, A. J. Kozubal, and M. R. Kraimer, International conference on accelerator and large experimental physics control systems (1991), https://www.osti.gov/biblio/6110347.

[55] http://docs.nscl.msu.edu/daq/.

[56] R. Fox, R. Au, and A. V. Molen, IEEE Transactions on Nuclear Science **36**, 1562 (1989) DOI: 10.1109/23.41102.

[57] G. L. Engel et al., Nucl. Instrum. Methods Phys. Res. A **573**, 418 (2007) DOI: 10.1016/j.nima.2006.12.052.

[58] S. Ahn, "The study of nuclear structure of neutron-rich 81Ge and its contribution in the r-process via the neutron transfer reaction 80Ge(d,p)", PhD thesis (University of Tennessee, 2013), http://trace.tennessee.edu/utk_graddiss/2392.

[59] P. Malzacher, N. Iwasa, and H. Weick, https://web-docs.gsi.de/~weick/atima/.

[60] https://www.github.com/j-browne/raumlehre.

[61] J. Cameron et al., Nucl. Data Sheets **113**, 365 (2012) DOI: 10.1016/j.nds.2012.02.001.

[62] M. Wang et al., Chin. Phys. C **41**, 030003 (2017) DOI: 10.1088/1674-1137/41/3/030003.

[63] A. F. Scott et al., Nucl. Phys. A **552**, 363 (1993) DOI: 10.1016/0375-9474(93)90499-n.

[64] K. Schmidt, Private communication, 2017.

[65] A. Matic et al., Phys. Rev. C **84**, DOI: 10.1103/physrevc.84.025801 (2011) DOI: 10.1103/physrevc.84.025801.